POLITECNICO
MILANO 1863

**SCUOLA DI INGEGNERIA INDUSTRIALE
E DELL'INFORMAZIONE**

DESIGNING A TEST RIG FOR AN ELECTRICAL MULTI-PROPELLER SYSTEM

Tesi di Laurea Magistrale in
Aeronautical Engineering - Ingegneria Aeronautica

Author: **Gabriele Morelli**

Student ID: 945556
Advisor: Prof. Pierangelo Masarati
Co-advisors: Michele Zilletti
Academic Year: 2021-22

Abstract

The design of new multi-propeller eVTOL (Electric vertical take-off and landing) aircraft configurations for Advanced Air Mobility requires both new experimental and analytical tools and studies. This thesis presents a cost-effective design of a single Lift/Thrust Unit (LTU) test rig capable of measuring all the six components of its static and high-frequency dynamic loads and its relevant electrical parameters while simultaneously and effectively controlling its RPM (Revolutions per minute). A detailed technical analysis of the working mechanisms of the main components was first of all necessary (Chapter 1), and part of this analysis led to Appendix B, in which a method for the preliminary choice of the main components is presented. Then the Lift/Thrust Unit electrical drive system was designed by programming a microcontroller to control its RPM (Revolutions per minute) and by designing a custom Hall effect RPM sensor printed circuit board (Chapter 2). Several load cell-based measurement systems were designed and produced to measure both static and high-frequency dynamic loads (Chapter 3), and the static and dynamic loads data obtained with the different systems were then compared, both in hover and in forward flight (Chapter 4). It was found that with the proposed electrical drive system it is possible to drive the Lift/Thrust Unit at almost constant RPM even in an open-loop control mode, although the system is completely set up for closed-loop RPM control, should the latter turn out to be desirable in the future. As far as loads measurement systems are concerned, two out of the three proposed solutions turned out to be suitable for the measurement of high-frequency (within the 250 Hz interval) dynamic loads. The test rig presented in this thesis, which is part of an internship at Leonardo SpA Helicopter Division, can therefore be considered as the first-step towards the design of wind tunnel test rig of multiple Lift/Thrust Units in arbitrary relative position and tilt angle, which could be employed to provide the necessary experimental data, with an emphasis on loads data, to both assist and validate new multi-propeller eVTOL designs

Keywords: Advanced Air Mobility, test rig, eVTOL, Lift Thrust Unit, dynamic loads

Abstract in lingua italiana

Il progetto di nuove configurazioni di velivoli eVTOL (Electric vertical take-off and land-ing) multi-elica per l'Advanced Air Mobility richiede nuovi strumenti e studi sia speri-mentali che analitici. Questa tesi presenta un progetto economicamente conveniente di un banco di prova per una singola Lift/Thrust Unit (LTU) in grado di misurarne tutte e sei le componenti dei carichi statici e dinamici e i parametri elettrici rilevanti controllandone efficacemente gli RPM (Revolutions per minute). Prima di tutto, si è resa necessaria un'analisi tecnica dettagliata dei principi di funzionamento dei principali componenti (Capitolo 1), e parte di questa analisi ha portato all'Appendice B, in cui si presenta un metodo per la selezione preliminare dei componenti principali. Successivamente si è progettato il sistema di azionamento elettrico della Lift/Thrust Unit programmando un microcontrollore per controllarne gli RPM e progettando una PCB (Printed circuit board) per un sensore RPM ad effetto Hall personalizzato (Capitolo 2). Per misurare sia i carichi statici che quelli dinamici ad alta frequenza si sono progettati e realizzati diversi sistemi di misura basati su celle di carico (Capitolo 3), e si sono poi confrontati i dati relativi ai carichi statici che dinamici ottenuti con i vari sistemi, sia in hover che in volo avanzato (Capitolo 4). Si è rilevato che utilizzando il sistema di azionamento elettrico proposto, è possibile operare la Lift/Thrust Unit a RPM pressochè costanti già con una modalità di controllo in anello aperto, anche se il sistema è gia completamente predisposto per un controllo in anello chiuso degli RPM nel caso questo dovesse tornare utile in futuro. Per quanto riguarda i sistemi di misura dei carichi, due delle tre soluzioni proposte si sono rilevate adeguate per la misura di carichi dinamici ad alta frequenza (entro i 250 Hz). Il banco di prova presentato in questa tesi, che è parte di un tirocinio presso la divisione elicotteri di Leonardo SpA, può dunque essere considerato il primo passo verso il progetto di un banco di prova in galleria del vento per diverse Lift/Thrust Units in posizione rel-ativa e angolo di tilt arbitrari, che possa essere impiegato per fornire i dati sperimentali necessari, con un'enfasi sui dati relativi ai carichi, sia a supportare che a validare progetti di nuovi eVTOL multi elica.

Parole chiave: Advanced Air Mobility, banco di prova, eVTOL, Lift Thrust Unit, carichi dinamici

Contents

Contents

Acronyms

AAM Advanced Air Mobility.

AC Alternating current.

ADC Analog to Digital Converter.

BEMF Back electromotive force.

BLDC Brushless, direct current motor.

BPMS Brushless permanent magnet synchronous motor.

CG Center of gravity.

DAC Digital to Analog Converter.

DC Direct current.

DEP Distributed Electric Propulsion.

EN Enable.

ESC Electronic speed controller.

FEM Finite element method.

FFT Fast Fourier Transform.

FOC Field-oriented control.

FR Frequency response.

FRF Frequency response function.

GND Ground.

I2C Inter-Integrated Circuit communication protocol.

IC Integrated circuit.

INL Integral nonlinearity.

LCD Liquid Crystal Display.

LSB Least Significant Bit.

LTU Lift/Thrust Unit.

MCU Microcontroller unit.

MMF Magnetomotive force.

MOSFET Metal-oxide-semiconductor field-effect transistor.

PCB Printed circuit board.

PI Proportional Integral.

PID Proportional Integral Derivative.

PMSM Permanent magnet synchronous motor.

PS Power Source.

PWM Pulse-width modulation.

RC Radio Controlled.

RMS Root mean square.

RPM Revolutions per minute.

RS Register select.

RW Read/Write.

SPWM Sinusoidal pulse width modulation.

SV Space vector.

SVPWM Space vector pulse width modulation.

UAV Unmanned aerial vehicle.

VTOL Vertical Take-Off and Landing.

Introduction

The concept of "Advanced Air Mobility" (AAM) (see [11] and [6]) is gaining more and more attention from the aerospace industry, and its market is expected to grow significantly in the next 8 years (see [25]). AAM is an air transportation concept which consists of designing aircraft running on sustainable energy sources to improve the accessibility of rural and regional areas to every kind of people and cargo, and to improve their mobility in high-density urban centers ("Urban Air Mobility"). The adoption of conventional VTOL (Vertical Take-Off and Landing) aircraft to large-scale civil transportation is limited by several issues which, for helicopters, include a flight price which is out of reach for most people and a relatively high noise level, the latter limiting in the end the potential net travel time savings (see [26] and [17]). Therefore, the aerospace industry, in an attempt to meet the more stringent requirements and targets (see reference [6]) relating to large-scale civil transportation, has developed different kind of prototypes and technology demonstrators of electric multi-propeller VTOL aircraft over the last years. Multiple configurations have been considered, all of which typically feature "Distributed Electric Propulsion" (DEP) and "autonomous operations" technologies" [1] Typical configurations are the tilt-propeller, tilt-wing and multi-copter. An example for the first configuration is provided by the Joby S4 demonstrator shown in Figure 1. This DEP, four-seat, personal transportation aircraft has four tilting propellers mounted on its polyhedral [2] wing and two on its V-tail. The propellers provide vertical force in thrustborne flight [3], and are tilted by 90° to provide the propulsive force in wingborne flight. Two examples for the second configuration are the A^3/Airbus Vahana demonstrator and the NASA GL-10 UAV (Unmanned aerial vehicle), DEP flight demonstrator (both defunct) shown in Figures 2 and 3, respectively. The Vahana featured a forward and an aft wing on which four propellers are mounted for a total of eight, and the propulsive force for wingborne flight is provided by tilting by 90° both wings [4]. Similarly, the NASA GL-10 had a tilting wing and a horizontal stabilizer with, respectively, eight and two propellers. The eighteen propeller

---

[1] In fact, as discussed in [6], the use of DEP may have several benefits in terms of noise level and safety
[2] The inner part of the high wing has a dihedral shape, while its outer part is anhedral
[3] Control in thrustborne flight is achieved by differential thrust
[4] The tilt-wing configuration has the obvious advantage of a simpler actuation system since only two actuators are needed to rotate the wing instead one for each propeller

Figure 1: Joby Aviation S4 demonstrator (picture from [26])

eVolo Volocopter and the eHang octocopter provide instead examples of the multicopter configuration. Since multicopter aircraft do not make use of wings, they are expected to be slower, with shorter range, and less efficient.

Of course some obstacles have to be overcome before these aircraft can be put on the market. On the technological side, they include battery technology, vehicle efficiency, and vehicle performance and reliability (see reference [6]). On the engineering side, several critical aspects are connected to the design of these novel configurations and are therefore worth investigating. One of them is the aerodynamic interaction between propellers in side-by-side and tandem configurations [5] both in hover and in forward flight conditions, being the classical literature focused on rotors, characterized by articulated, high aspect ratio blades, in hover, instead of on propellers, characterized by rigidly mounted, relatively low aspect ratio blades, in both hover and forward flight. This aspect in thoroughly discussed in reference [33]. Another critical aspect is the generation of substantial dynamic, high-frequency structural loads which takes place during the conversion phase of tilt-propeller and tilt-wing configurations. This is due to the fact that, during conversion, the rigidly mounted blades of the propellers operate in the unusual conditions of edgewise flow instead of the usual conditions of axial flow which are attained, on the other hand, in thrustborne (hovering) and wingborne flight. These loads may cause several issues like

---

[5]Both of these configurations are indeed present at the same time in aircrafts like the Joby S4 (Figure 1) and the Vahana (Figure 2)

Figure 2: A^3/Airbus Vahana demonstrator (picture from [19])

Figure 3: NASA GL-10 (picture from [18])

a shortened life of the aircraft structure due to fatigue, and passengers discomfort due to excessive noise and vibrations. Therefore, the design of a test rig for the hover and wind tunnel testing of multiple "Lift/Thrust Units" (LTUs) [6] in arbitrary relative position and tilting angle is of interest both when developing new multi-propeller aircraft and when validating complete designs. A notable example of such a test rig is discussed in [21], and the same test rig was then employed for the studies presented in [20] and [22]. The concept is shown in Figure 4.
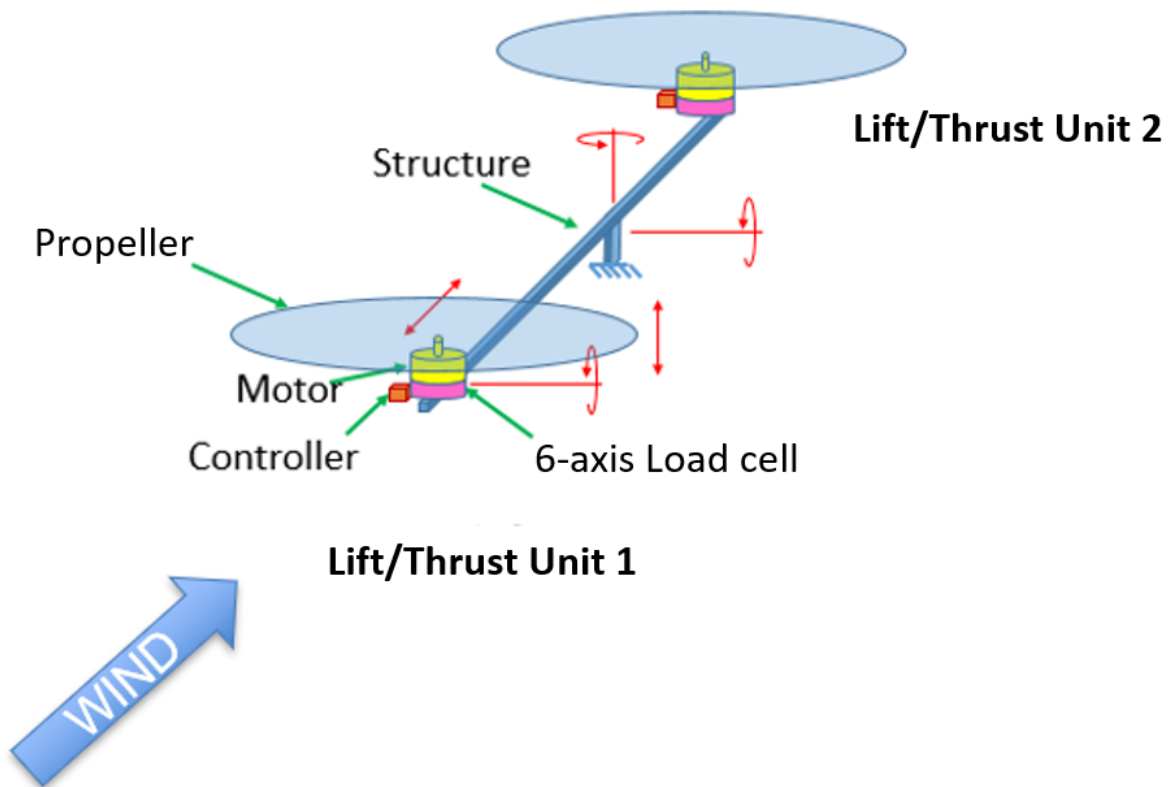

Figure 4: Wind tunnel test rig schematic diagram

In the context of this project, this thesis presents the design of a test rig (shown schematically in Figure 5) for a single LTU intended to be part of a multi-propeller aircraft. The functional block diagram of the rig is shown in Figure 5, while Figure 6 is a picture of the final version of the rig designed in this thesis work, and its main components are indicated in Figure 7. The propeller comprises 3 carbon fiber blades of length from root to tip

---

[6]The term "LTU" is used to denote the system comprising the propeller and the electrical motor by which it is driven, and, as an example, the LTU that was incorporated in the final version of the single LTU test rig (which was designed in this thesis work), is shown in Figure 8

equal to 276 mm, and it is driven by a trapezoidal BPMS (Brushless permanent magnet synchronous) motor, more commonly known as BLDC (Brushless direct current) motor [7], up to 5000 RPM (Revolutions per minute) continuously. The ESC (Electronic speed controller), powered from a DC (Direct current) Power Supply, drives the motor through "Sensorless six-step commutation" when detecting PWM (Pulse-width modulation) pulses from the MCU (Microcontroller Unit). The loop **could** [8] be closed by an Hall-based rotary magnetic RPM sensor : the MCU sets the value of the PWM duty cycle according to the RPM value measured by this RPM sensor. The static and dynamic loads are measured by a load cell, the channels of which are acquired by the Siemens SCADAS data acquisition system. To connect the load cell to the motor, various mechanical interfaces were designed and produced.
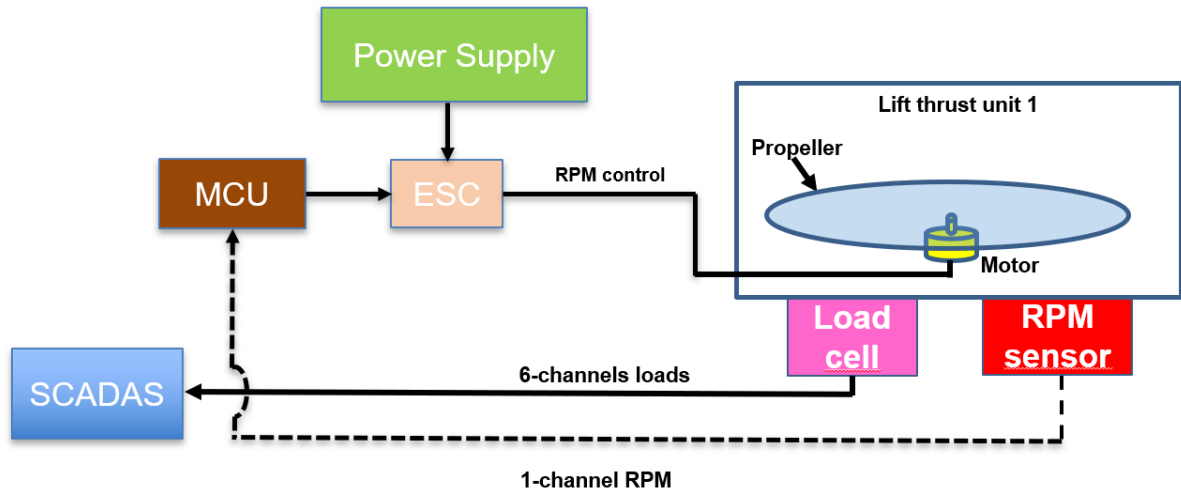

Figure 5: Functional block diagram of the single LTU test rig

---

[7]BPMS is a better name than BLDC for this kind of motor. See in this regard section 1.1.1

[8]The actual software implementation of e.g. a PI (Proportional integral) or a PID (Proportional integral derivative) RPM controller is not presented in this work
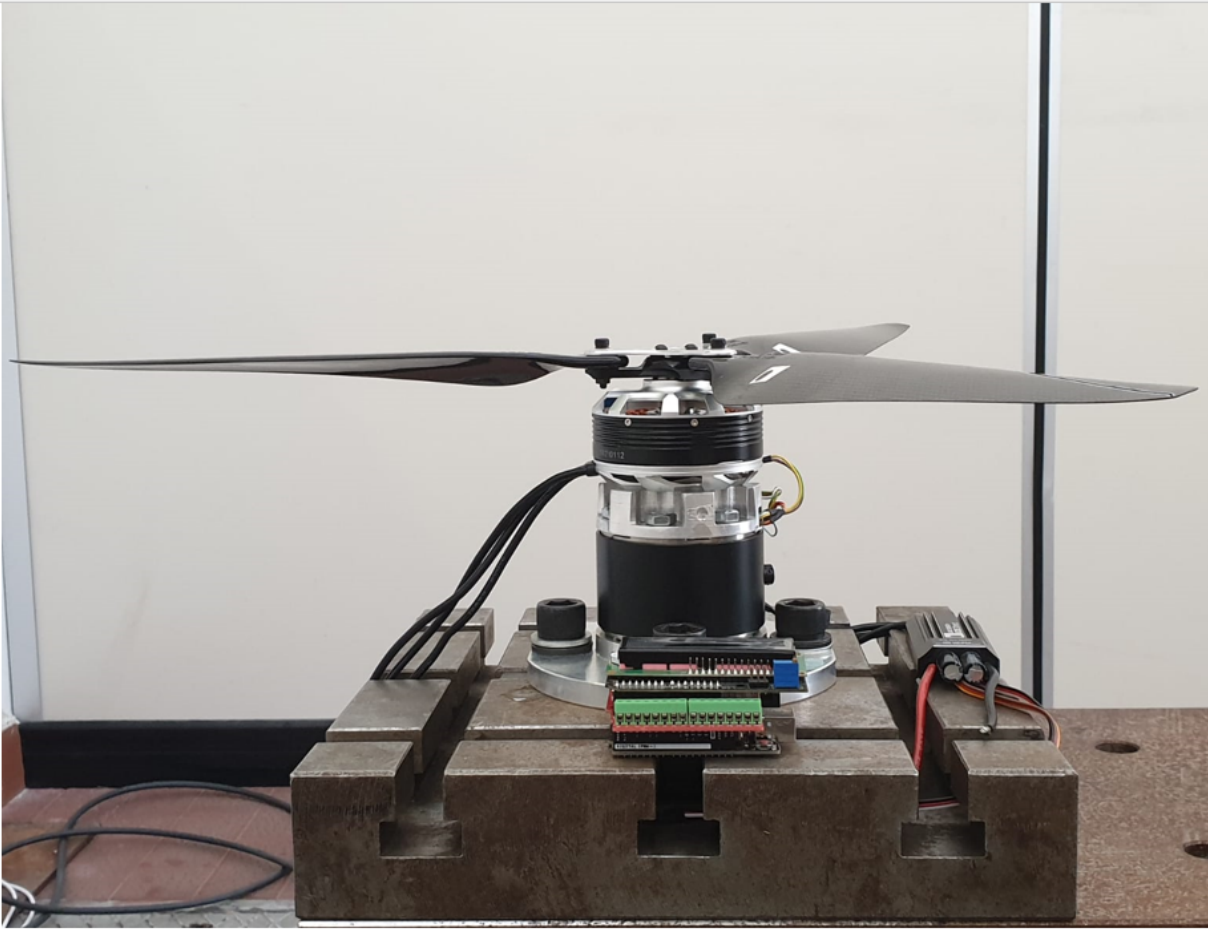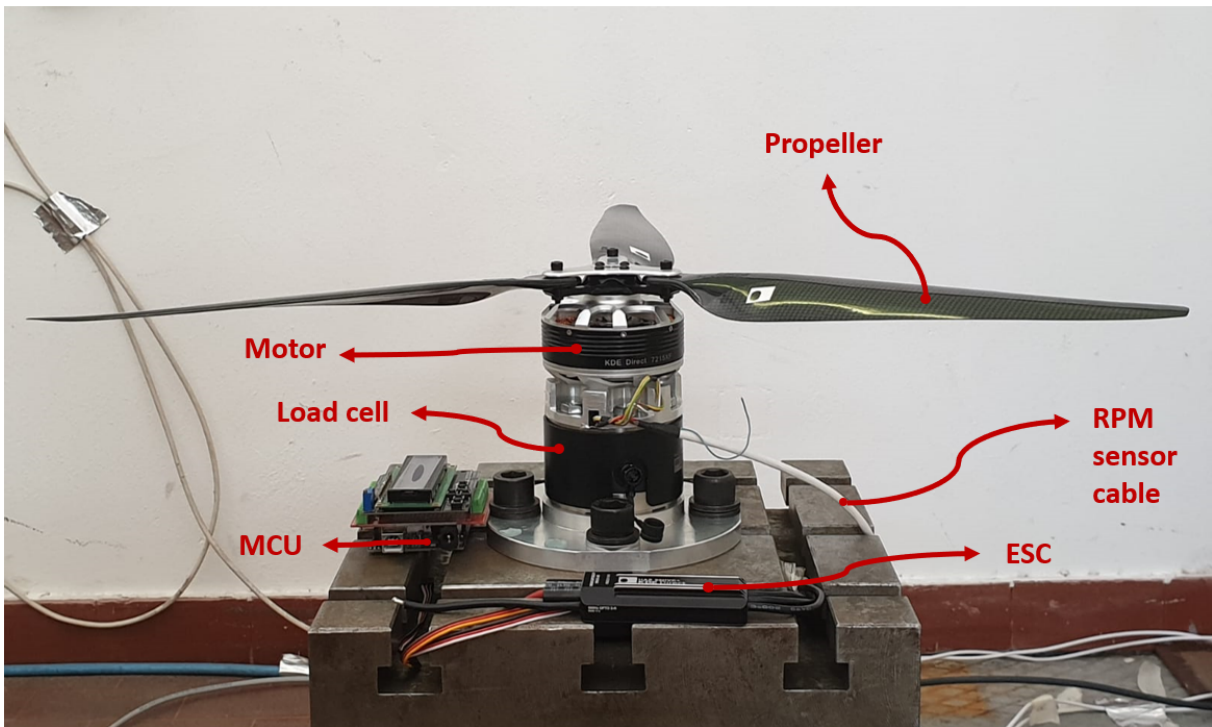
Figure 6: Single LTU test rig

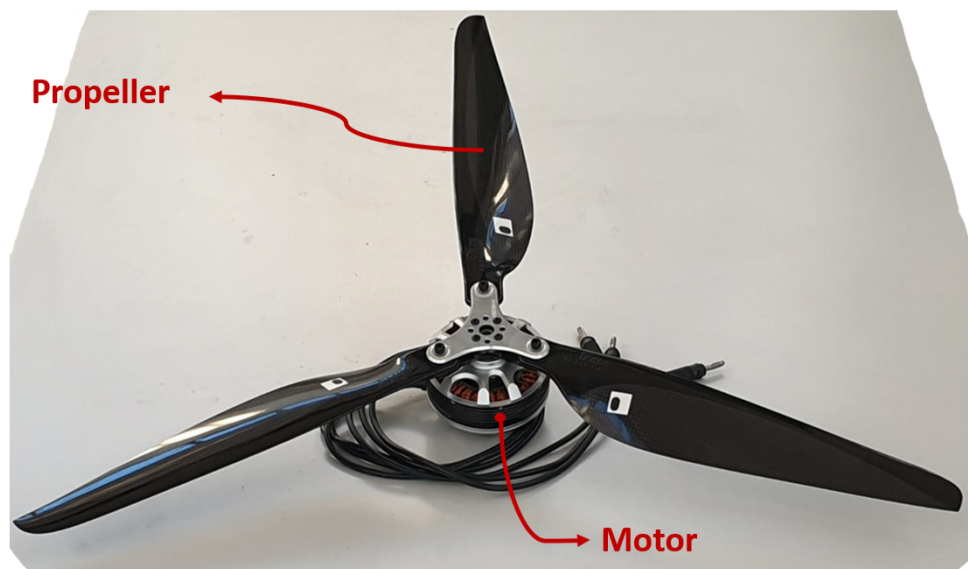Figure 7: Main components of the single LTU test rig

Figure 8: LTU

The design here presented provides a cost-effective solution to the following engineering problems :

- Designing a load cell based measurement system capable of measuring all the six components of LTU static and dynamic loads in the 250 Hz frequency range, the

upper limit being determined by the objective of measuring the amplitude of the 3/rev harmonic component at the maximum propeller RPM value of 5000. The 3/rev harmonic component is therefore at a frequency of 250 Hz. The significance of the 3/rev harmonic component lies in the fact that it is the lowest frequency load component transmitted to the rotor shaft. In fact, under the hypothesis of identical blades performing the same periodic motion, it could be proven (see section 18.3 of reference [14]) that only the static component and components which are integer multiplies of the number of blades, 3 in our case, are transmitted to the rotor shaft

- Mechanically interfacing the LTU with the load cell

- Designing a custom RPM sensor PCB (Printed circuit board)

- Interfacing a MCU with the motor ESC and with the custom designed RPM sensor PCB

- Driving the LTU at constant RPM

The experimental data pertaining to static and dynamic loads (see chapter 4) obtained with the test rig was used to develop a rigid blade, rigid support aerodynamic model of the propeller shown in Figure 1.22. Furthermore, Giovanni Chiarolla, a Master's degree student in Space Engineering and intern at Leonardo SpA Helicopter Division at the time of writing, joined the project by writing a master's thesis whose objective was to develop an analytical model of the electrical drive system (see chapter 2) of the single LTU test rig here presented and to validate it with experimental data. More in general, the test rig presented in this work can be considered as the first step towards the design of a wind tunnel test rig (see Figure 4) of multiple Lift/Thrust Units which could be employed to provide the necessary experimental data to :

- Understand the dynamics of an isolated propeller in edgewise flow in terms e.g. of aerodynamics, loads generation and dynamic response, and how it is impacted by blade flexibility

- Measure the static and dynamic loads generated by a propeller at different RPMs and at different air speeds (both in steady state and in transient conditions)

- Evaluate the effect the interaction between the propellers (in tandem or coaxial configuration) has on the dynamics of a single propeller

- Evaluate the effect of the interaction with the supporting structure (aeroelasticity)

- Evaluate single and multiple propeller acoustics

- Understand how the dynamics of an isolated propeller and the effect of the interaction between propellers scale with their size

1 | Detailed technical analysis of the initial components of the test rig

The design of the test rig started from some off-the-shelf components, but only some of them turned out to be suitable for the design purposes discussed in the introduction. Two triple blade propellers of different sizes were initially available, one having a diameter of 317.5 mm, and the other a diameter of 622.30 mm. These propellers were to be driven by a 48 mm and 80 mm diameter BPMS motor, respectively. An ESC which could drive both motors when powered by a laboratory DC power supply was also available, as well as an Arduino UNO R3 board to control the motor RPM. To measure the LTU loads, a 80 mm diameter, 6-axes strain gauge load cell was chosen. The following sections of this chapter discuss the main characteristics and working mechanisms, from both the mechanical and the electrical point of view, of the sole major components which were in the end integrated in the final design. This material is complementary to the one presented in Appendix B, in which methods for the selection of an appropriate LTU and the associated "Power Source" (PS) are presented.

1.1. Permanent magnet synchronous motor (PMSM) and Electronic speed controller

This section starts with the description of the general working mechanisms of a PMSM and of an ESC. Next, the discussion will focus on the particular PMSM and ESC which were in the end integrated in the final design.

1.1.1. Brushless permanent magnet synchronous motors and the need for an ESC

Any three-phase AC (Alternating current) motor, by which here is meant *any motor that will not turn continuously when connected to a battery* [1], requires a **motor controller**, represented in Figure 1.1, which synthetizes the three supply waveforms starting from the power supply waveform. The need for such a motor controller, which by the way is always electronic/electrical, can be justified for a generic **nonsalient**[2] brushless **permanent magnet synchronous** motor (a particular type of three-phase AC motor) as follows. The rotor magnets produce an airgap flux density (examples of which are shown in Figure 1.2) which is a function of the angle α around the rotor (θ_r is the rotor angular position) :
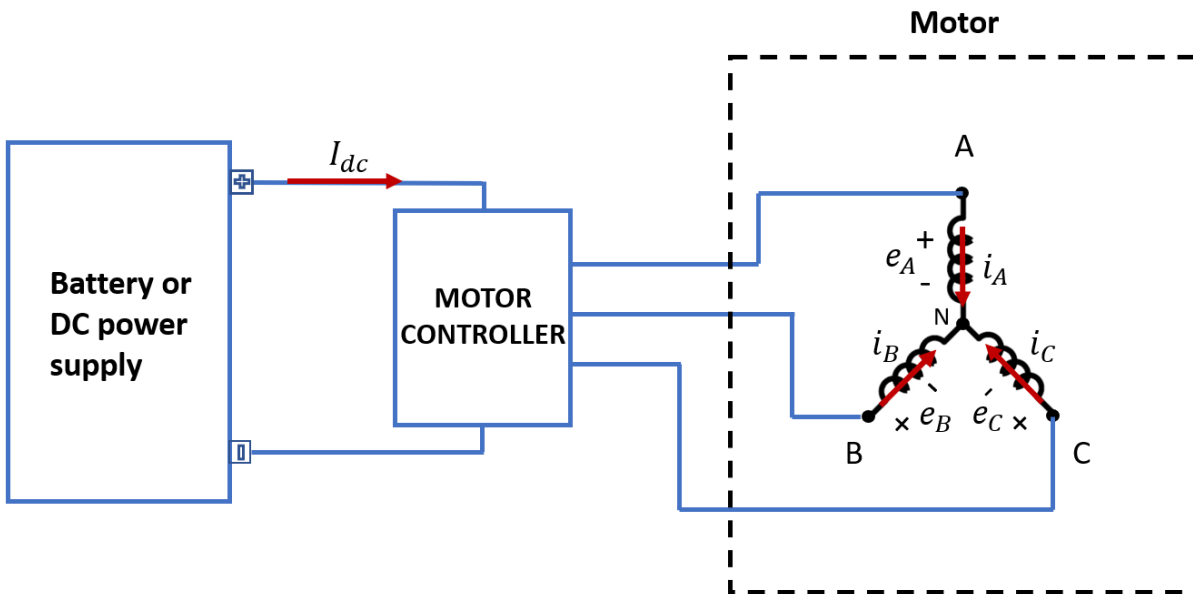

Figure 1.1: Functional block diagram of a wye-connected PMSM

---

[1]Definition taken from section "Taxonomy of Motors" on page 13 of reference [17]
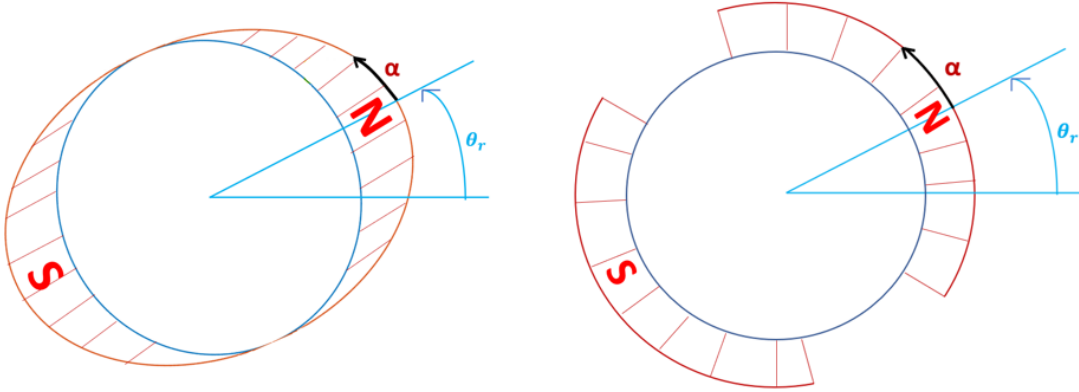[2]See section "Magnetic Saliency" on page 17 of reference [17]

Figure 1.2: Magnets airgap flux density distributions, sinusoidal (left), "trapezoidal" (right)

Since the three phases/windings are fixed in space, it is then possible to show [3] that the associated **rotor-stator flux linkages** Ψ_R are only periodic functions of the rotor angular position θ_r expressed in **electrical degrees** [4] (and are displaced from each other by 120°). Therefore, the torque produced by a single phase/winding is itself a function of θ_r, since :

$$T(t) = \frac{d}{d\theta_r}\Psi_R(\theta_r) \cdot i(t) \tag{1.1}$$

where $T(t)$ is the torque produced by that phase, Ψ_R the associated flux linkage, and $i(t)$ the current through it (the phase currents are shown in Figure 1.1 as i_A, i_B and i_C together with their positive direction). The function $\frac{d}{d\theta_r}\Psi_R(\theta_r)$ is equal to the **per-phase BEMF (Back electromotive force) function** $k_e(\theta_r)$, which can be proven to be equal to the **per-phase torque function** $k_t(\theta_r)$ [5]. It follows that $T(t)$ can be written also as [6] :

$$T(t) = k_t(\theta_r) \cdot i(t) \tag{1.2}$$

---

[3] See section "Rotor-Stator Flux Linkage" on page 292 of reference [17]

[4] The distinction between electrical and mechanical degrees and between electrical and mechanical angle is relevant for motors with more than two poles. The distinction is made clear in section "Electrical and Mechanical Measures" of chapter 3 of reference [17]

[5] See from page 38 to 42 of reference [17]

[6] Incidentally, equation 1.2 it is clear that if the motor only had one phase/winding, it would not be controllable to any arbitrary θ_r. In fact if the motor is at rest at a position θ_r for which k_t is equal to zero, no current can send through it which will move it out from this θ_r. This is the reason for using three phases, offset one another by 120°

The total produced torque τ can be derived from equation 1.3, which is the general energy balance for a three-phase motor :

$$\tau \cdot \omega = e_A i_A + e_B i_B + e_C i_C \tag{1.3}$$

where ω is the rotor angular speed, e is the back-EMF voltage, and the subscripts indicate the phase (see Figure 1.1, which also shows the sign convention for the back-EMF voltages). The function $k_e(\theta_r)$ is defined in terms of e as in equation 1.4 :

$$e := k_e(\theta_r)\omega \tag{1.4}$$

Therefore : [7]

$$\tau = k_{tA}(\theta_r)i_A + k_{tB}(\theta_r)i_B + k_{tC}(\theta_r)i_C = k_t(\theta_r)i_A + k_t(\theta_r - 120°)i_B + k_t(\theta_r + 120°)i_C$$

$$\tag{1.5}$$

Any existing nonsalient **permanent magnet** motors have a k_t function which (ideally) possesses quarter wave symmetry over the electrical period [8]. Therefore, from equation 1.5 we see that to obtain an always positive (or negative) total torque τ while taking full advantage of the negative (or positive) part of the functions $k_t(\theta_r)$, $k_t(\theta_r - 120°)$ and $k_t(\theta_r + 120°)$, each of the phase currents i_A, i_B, i_C has to maintain the same polarity as the corresponding k_t function (see Figure 1.3 for the particular case of a sinusoidal BPMS motor), and this implies both polarity reversal over the electrical period and **synchronization** with the rotor position θ_r, the latter meaning that the rotational frequency of the rotor has to be the same as the frequency of the phase currents, whence the adjective "Synchronous" in the acronym "BPMS" for these kind of motors.

---

[7]See section "Torque Production on page 51 of reference [17]
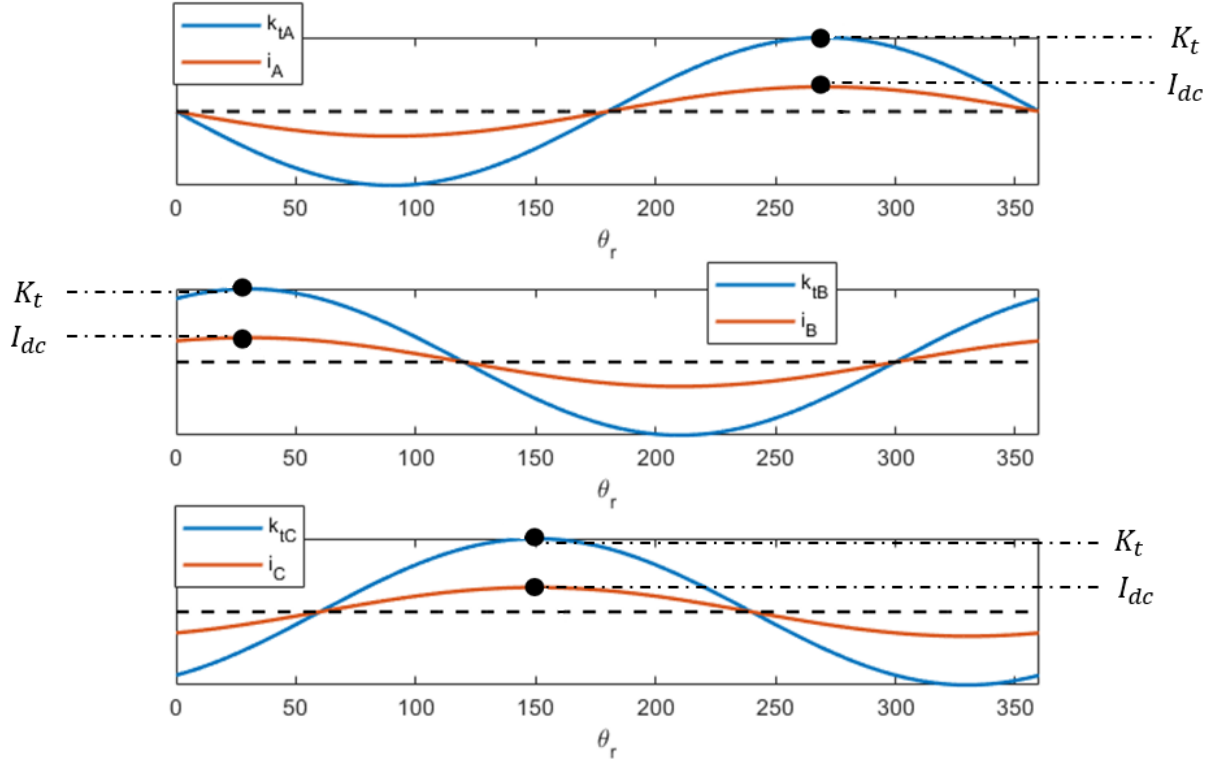[8]See Appendix "C" of reference [17]

Figure 1.3: Phase currents for a sinusoidal BPMS motor

No existing power supply can provide these current waveforms by itself, hence the need for an electronic/electrical motor controller. At this point it is relevant to understand which is the optimal shape of the three current waveforms, i.e. which shape gives a **constant torque τ of the greatest possible magnitude** for a given **peak of the three-phase currents I_{dc}** [9], or, equivalently, for a given **output current I_{dc}** (shown in Figure 1.1) from the power supply. **To this end, in all the following discussion the brushless permanent magnet motor will again be assumed to be nonsalient and also wye-connected, unless otherwise specified**. Two prototypical cases will be considered, that of a **sinusoidal and that of a trapezoidal motor**, meaning that they have sinusoidal and "trapezoidal" $\Psi_R(\theta_r)$, respectively, and consequently sinusoidal and trapezoidal $k_t(\theta_r)$ and $k_e(\theta_r)$, respectively : [10]

---

[9]Assume for the sake of simplicity that the three phase currents are "balanced", meaning that they have equal magnitude (amplitude in case of a sinusoidal waveform) and phase angles differing from each other by 120°

[10]A sinusoidal motor according to the given definition is not required to have "sinusoidal" windings. See appendix C, in particular section "Conclusions" on page 306 of reference [17] for detailed information
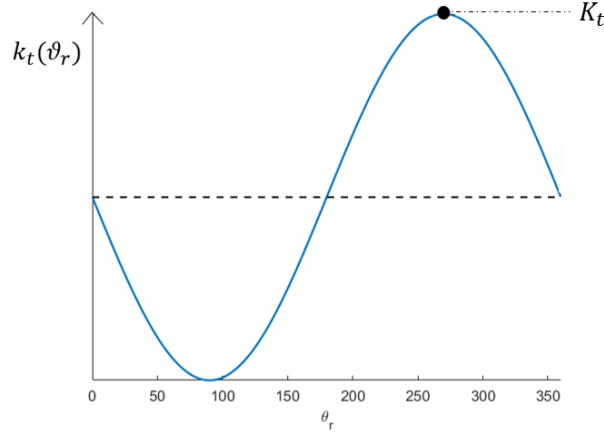
(a) Sinusoidal.
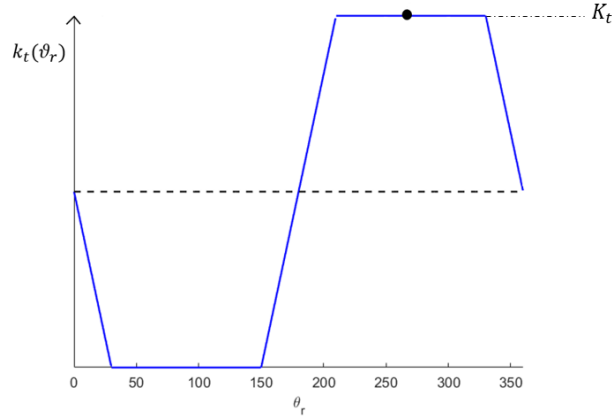
(b) Trapezoidal.

Figure 1.4: Torque functions for BPMS sinusoidal and trapezoidal motors

Starting with the sinusoidal motor, for which, as we have stated already in words, we have $k_{tA} = -K_t \sin \theta_r$, $k_{tB} = -K_t \sin (\theta_r - 120°)$ and $k_{tC} = -K_t \sin (\theta_r + 120°)$, where "$K_t$" is the so called **per-phase torque constant**, which represents the magnitude of the per-phase torque functions. It can be shown [11] that if :

$$i_A = -I_{dc} \sin \theta_r \tag{1.6}$$

$$i_B = -I_{dc} \sin (\theta_r - 120°) \tag{1.7}$$

$$i_C = -I_{dc} \sin (\theta_r + 120°) \tag{1.8}$$

that is, if sinusoidal phase currents of amplitude I_{dc} are injected into the windings and kept in phase with the corresponding torque function (see Figure 1.3), a **constant** torque

---

[11]See page 53 of reference [17]

of value.

$$\tau = \frac{3}{2}K_t I_{dc} \qquad (1.9)$$

is produced [12]. This motor control scheme, which is a **current control scheme**, is called **sine-wave drive** (or "sinusoidal commutation"). That fact that this is also the greatest possible magnitude of τ (for a sinusoidal motor) for a given I_{dc} will be discussed later on.

Moving on to the **trapezoidal motor**, the analytical expressions of the k_t functions could be given as piecewise functions. However, for our purposes, this is not necessary. In fact, assuming that the k_t functions are constant over at least a 120° interval [13], it is clear that **a constant τ (although maybe not of the greatest possible magnitude) can be achieved by injecting currents which are equal to I_{dc} and $-I_{dc}$ over the constant positive and negative portions,respectively, of the corresponding k_t function, and which are zero elsewhere** [14] :

---

[12]This is analogous to the cancellation of vibratory loads at frequencies which are not integer multiples of the number of blades which was mentioned in the introduction

[13]In the case of a delta-connected motor, a 60° flat top interval is required. See section 1.1.2 and, in particular, Figure 1.21

[14]If the k_t function of the real trapezoidal motor doesn't quite have this 120° constant interval, this will result in some torque ripple
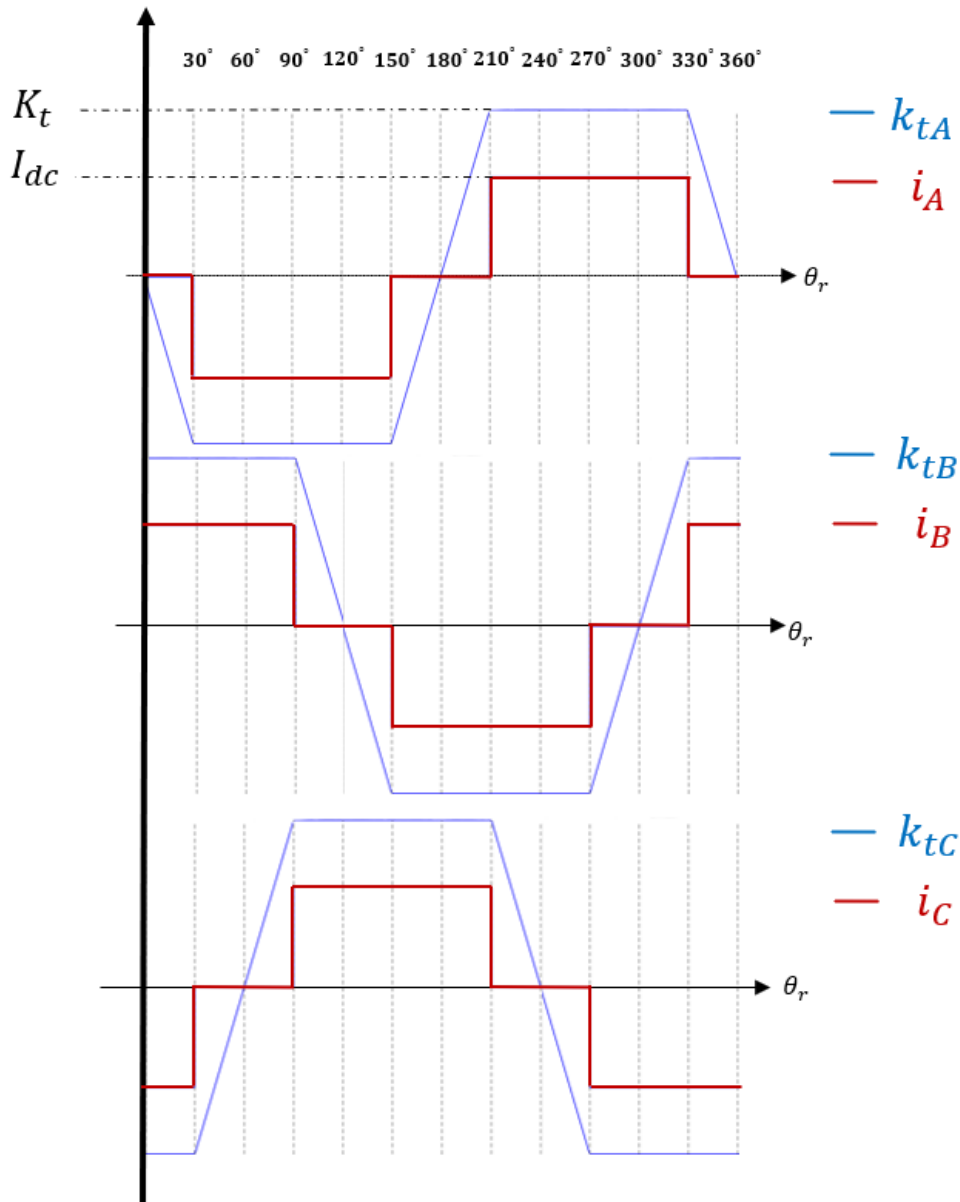
Figure 1.5: Phase currents for a trapezoidal BPMS motor

Since only two phases conduct at any given time (and at the constant portion of the corresponding k_t function), it follows from equation 1.5 that the constant torque is given by :

$$\tau = 2K_t I_{dc} \tag{1.10}$$

This current control scheme can be called **120° six-step commutation** (in literature it

is also called "trapezoidal drive", "six-step commutation", etc.) [15]. From Figure 1.5 we see that each phase current changes only six times in an electrical period, and that, as mentioned before, only two phases at a time are active with a given current polarity. This means that the full electrical period can be logically divided into six sectors corresponding to the pair of phases being active for a given rotor position θ_r. **In fact, a typical way to implement this scheme is to place three Hall effect sensors evenly around the stator**. The digital readings (1 means "high", which corresponds to the stator north pole being detected, 0 otherwise) of the sensors can be written as a three digit binary number (e.g. 100 means sensor "1" is high while the others are low). Only six combinations of the readings are possible, because binary numbers 000 and 111 are invalid [16], and to these combinations there correspond six equally spaced sectors around the stator. So, according to which of the six sectors the rotor is in, two phases are fed with currents of appropriate polarity, while the current flow in the third one is interrupted. **Another method to implement the six-step commutation scheme is to design a sensing circuit to detect the points at which the back-EMF voltage of one of the three phases becomes zero (these points are called "BEMF zero crossovers"). This method is called sensorless six-step commutation because it makes no use of Hall effect sensors. For the implementation details one can e.g. refer to [32]**. It should be mentioned that the six-step commutation current control scheme is a proper **electronic commutation** scheme since its only role is to reverse polarity and to interrupt the current flow, which is exactly the same role of the traditional commutator, while the magnitude of the current (and so the amount of torque) is controlled independently according to the required torque. On the other hand, the sine-wave drive scheme for a sinusoidal motor (which by the way is sometimes called PMSM (see page 58 of reference [17])) does not perform commutation in the traditional sense, since the instantaneous value of each phase current changes continuously.

It was mentioned that for a sinusoidal motor the sine-wave driver not only gives a constant τ, but a constant τ of the maximum possible magnitude. In fact, let's consider the following expression for the torque vector, valid for any nonsalient or singly-salient motor [17] :

$$\vec{\tau} = c\,\vec{\lambda} \times \vec{i} \tag{1.11}$$

---

[15] Apparently, the shape of the phase currents is the reason why a BPMS trapezoidal motor is sometimes called a BLDC. See page 57 of reference [17]

[16] In fact, numbers 000 and 111 imply that the north pole of the stator is facing in one case none and in the other all of the sensors (respectively) at once

[17] See page 12 of reference [30]

For the sake of simplicity, but without loss of generality, let's interpret equation 1.11 in the context of space vector (SV) theory, which, as presented from page 90 to page 151 of reference [17] is limited to motors having **sinusoidal windings** [18]. If so, $\overrightarrow{\lambda}$ can be taken as the total stator flux linkage SV, $\overrightarrow{i}$ as the current SV, while c is a positive constant. If the motor besides having sinusoidal windings also has a **wye connected stator with an isolated neutral**, the total flux $\overrightarrow{\lambda}$ can be expressed as [19] :

$$\overrightarrow{\lambda} = L_S \overrightarrow{i} + \overrightarrow{\psi}_R \tag{1.12}$$

in which L_S is called the *synchronous inductance* [20], and $\overrightarrow{\psi_R}$ rotor-stator flux linkage space vector. Substituting equation 1.12 for $\overrightarrow{\lambda}$ in equation 1.11, and using the properties of the cross product, one obtains :

$$\overrightarrow{\tau} = c \cdot \overrightarrow{\Psi}_R \times \overrightarrow{i} \tag{1.13}$$

From the definition of the cross product, it follows from equation 1.13 that the torque has magnitude given by :

$$\tau = c \mid \overrightarrow{\Psi}_R \mid\mid \overrightarrow{i} \mid \sin \delta \tag{1.14}$$

where δ is the counterclockwise angle measured from $\overrightarrow{\Psi}_R$ to $\overrightarrow{i}$. It is than clear the τ is maximum when $\delta = 90°$, that is when $\overrightarrow{i}$ is 90° in advance with respect to $\overrightarrow{\Psi}_R$. Since $\overrightarrow{i}$ is related to the stator MMF (Magnetomotive force) SV $\overrightarrow{f}$ via a scalar proportionality constant [21], **the physical interpretation of this fact is that τ is maximum when the stator MMF is 90° in advance with respect to the flux generated by the rotor (or, more precisely, the rotor-stator flux linkage)**. Now, as we have mentioned before, the per-phase Back-EMF function $k_e(\theta_r)$ is equal to the derivative with respect to θ_r of the per-phase rotor-stator flux linkage $\Psi_R(\theta_r)$, from which it follows that,

---

[18](see appendix "C" of reference [17]). An extension of the SV theory to non-sinusoidal motors, is described in chapter 2 of reference [30]. It is also interesting to note that if the motor has sinusoidal windings, the rotor-stator flux linkage $\Psi_R(\theta_r)$ is guaranteed to be sinusoidal even if the rotor is a "squarewave" rotor. See in this regard appendix "C" of reference [17]

[19]see appendix A and appendix B of reference [17]. It should also be mentioned that, in the context of the extended SV theory given in [30], both equation 1.12, and the consequent equation 1.13 are **guaranteed** to be valid also for non-sinusoidal windings, as long as the motor still has a wye connected stator with an isolated neutral

[20]L_S represents the "effective inductance" seen by each phase

[21]See section "Current Space Vector and its Interpretation" on page 111 of reference [17]

for a given $| \overrightarrow{i} |$ and $| \overrightarrow{\Psi}_R |$ [22], τ is maximum when $\overrightarrow{i}$ (or, equivalently, the stator MMF SV) is *parallel* to the Back-EMF space vector. This is indeed the relationship between $\overrightarrow{i}$ and the Back-EMF space vector in the sine-wave drive. Equation 1.14 can be expressed in a reference system rotating with the rotor, which is known as *dq reference frame* (see Figure 1.6), as follows :

$$\tau = \frac{3}{2}P \mid \overrightarrow{\Psi}_R \mid i_q \tag{1.15}$$

in which P is the number of *pole pairs* of the motor, and i_q the rotating q-axis component of the current SV $\overrightarrow{i}$ (see Figure 1.6). **From equation 1.15 one can deduce that only the q-axis component of current generates torque. This fact suggests a current control scheme in which the current SV $\overrightarrow{i}$ is adjusted to be completely aligned with the rotating "q" axis (or, equivalently, the d-axis component of the current SV is adjusted to be zero) so that the maximum torque per current is produced. This scheme is known as FOC, which stands for "field-oriented control".**
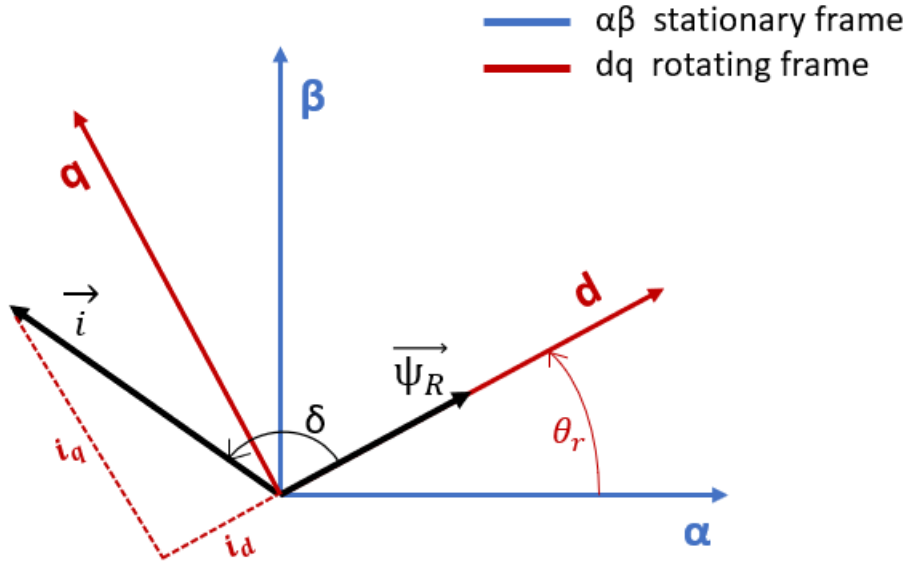

Figure 1.6: Reference frames and related components

As in the case of six-step commutation, also for the FOC scheme there exist both the sensored and sensorless implementations. In the implementation with sensors, the motor

---

[22]$| \overrightarrow{\Psi}_R |$ represents the peak value of the rotor-stator flux linkage $\Psi_R(\theta_r)$, and it *constant* for a given motor. For example, for a motor with sinusoidal windings and sinusoidal rotor flux it is given (reference [17]) by $\frac{\pi}{4}N \cdot d \cdot Y \cdot B_p$
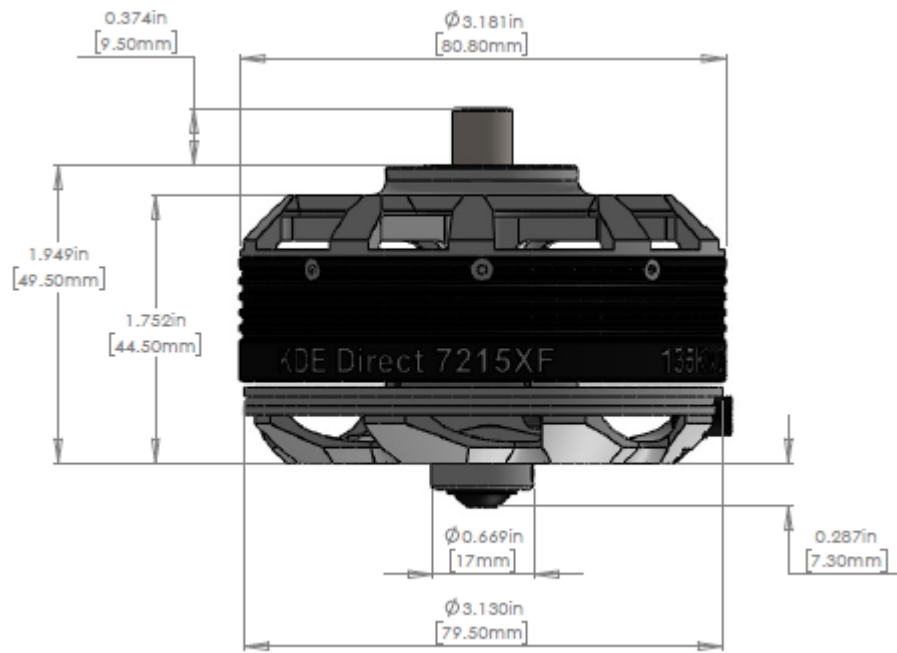
angular position and RPM are typically measured by an encoder or by Hall sensors, while in sensorless implementation the these two quantities are reconstructed/estimated based on the phase voltages and currents, and a "startup procedure" is required (see e.g. [16]). The two most commonly used modulation techniques in FOC are the "SVPWM" ("Space Vector PWM") and the "SPWM" ("Sine PWM"). SVPWM is described in references [24] and [13], while in reference [12] the two techniques are also briefly compared in terms of the maximum value achievable for the phase voltage. Concrete examples for both the sensored and sensorless implementations can be found e.g. in reference [29].

1.1.2. KDE7215XF-135 permanent magnet synchronous motor

KDE7215XF-135 motor is a **Trapezoidal Permanent Magnet Synchronous Motor**, a.k.a trapezoidal PMSM, meaning that it is a BPMS which develops a Back-EMF of trapezoidal shape (see section 1.1.1). In particular it is an outrunner PMSM, meaning that the rotor with its magnets encircles the stator, on which the stationary windings are placed. A description of its mechanical characteristics will now be given, followed by a description of its electrical characteristics.

1.1.2.1. KDE7215XF-135 mechanical characteristics

The overall features and dimensions of the motor are shown in Figure 1.7. The stator is shown in Figures 1.9 and 1.10. The two ball bearings in Figure 1.11a are press fitted one on top of another into the upper bearing retainer, visible in Figure 1.9, while the bigger bearing in Figure 1.11b is press fitted into the lower bearing retainer, visible in Figure 1.10. The dark grey annular parts visible in Figure 1.11 are the bearings shields. The rotor, together with its shaft and magnets, is shown Figure 1.12. The shaft, visible in Figure 1.13 is press fitted into the through hole on the top of the rotor body, until it attains a proper axial distance from it. Finally, the whole system is held together by the retaining collar shown in Figure 1.14. The collar is fixed relative to the shaft via its two set screws pressing against the two flat spots (upper end of shaft in Figure 1.13) of the shaft. Then, as shown in Figures 1.14 and 1.8, a button head cap is screwed into the shaft threaded hole, fixing the collar and inner ring of the lower bearing together.

(a)

Φ 10mm core shaft
9.5mm shaft extension

M4 x Φ 23mm, 90° pattern

M3 x Φ 25mm, 90° pattern

M3 x Φ 20mm, 90° pattern
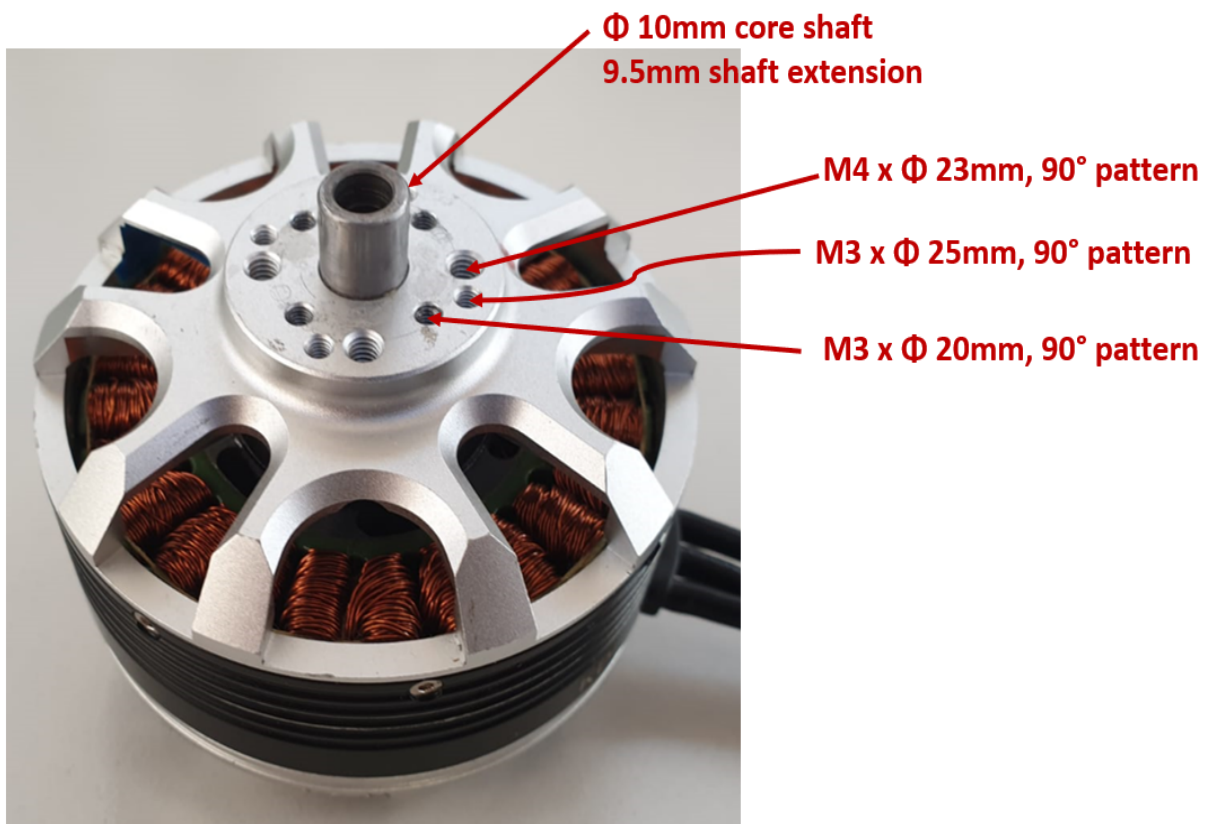
(b)

Figure 1.7: Overall dimensions, upper portion (Picture (a) from [3])

OVERSIZED 6000-2RS
RUBBER-SEALED
RADIAL BALL BEARING

SHAFT MACHINED
FLUSH TO COLLAR

FLANGED BUTTON HEAD
SOCKET HEAD CAP SCREW
RETAINER (M5 x 0.8 x 10MM)

TRIPLE 90° PATTERN THREADS
M5 x Ø 40MM
M4 x Ø 40MM
M4 x Ø 35MM
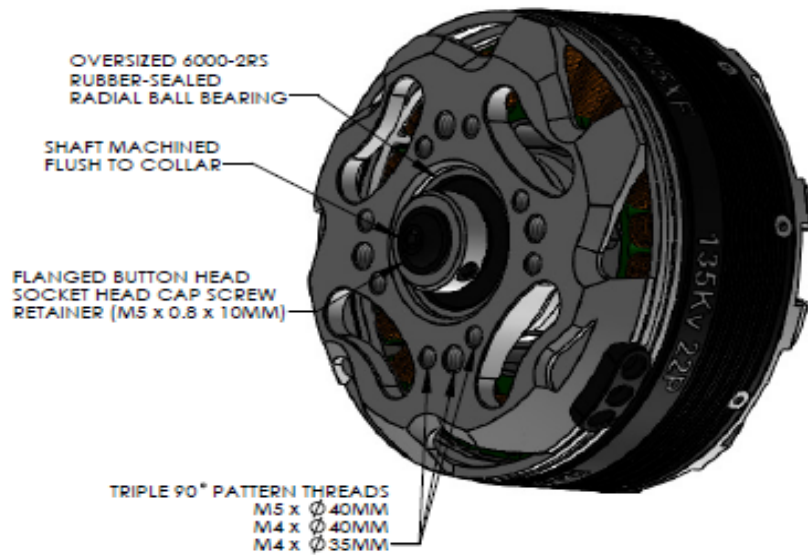
Figure 1.8: Overall dimensions, lower portion (Picture from [3])

Figure 1.9: Stator, front view (pictures from 1.9 to 1.14 are from KDE Direct)

Figure 1.10: Stator, back view

(a) Upper bearings.   (b) Lower bearing.

Figure 1.11: Bearings

Figure 1.12: Rotor, front view

Figure 1.13: Shaft
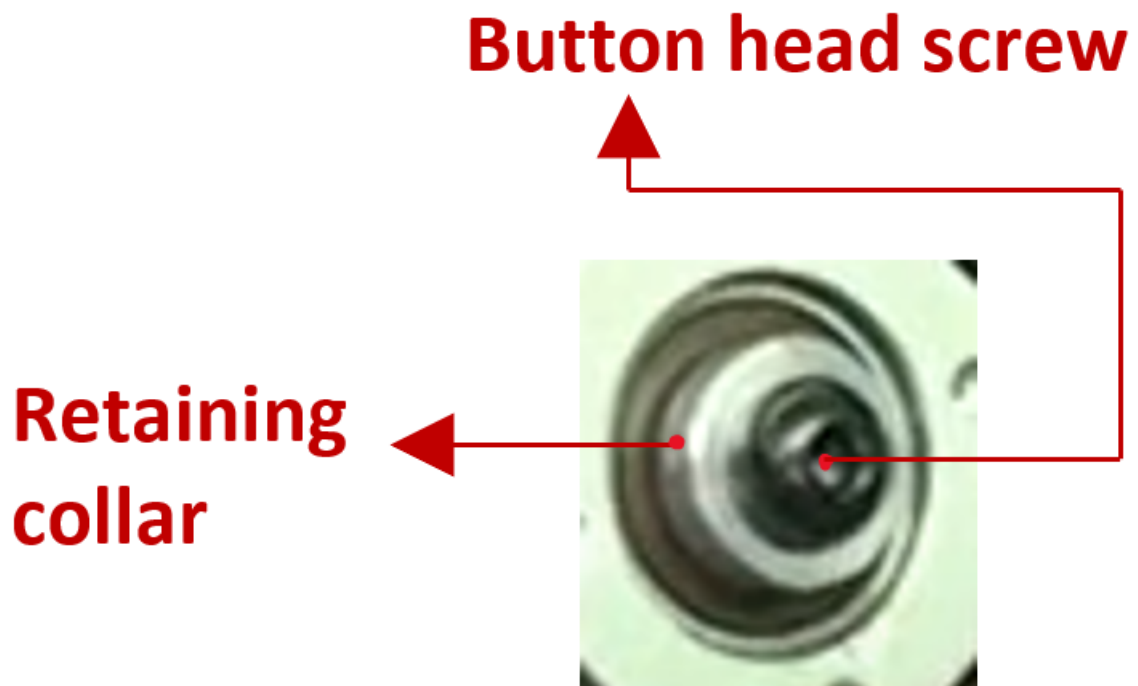
Figure 1.14: Button head screw and collar

1.1.2.2.   KDE7215XF-135 electrical characteristics

The motor maximum continuous current and maximum DC supply voltage are 45 A and 61 V, respectively. **Given these maximum ratings, it is capable of driving the propeller described in section 1.2 up to roughly 5000 RPM. The criteria for choosing a PMSM suitable for the given application are given in Appendix B. The motor is delta-connected and it is driven by sensorless six-step commutation control with synchronous rectification. This latter information was provided by the motor manufacturer (KDEDirect) itself, while in the remaining of this section and in section 1.1.3 the working mechanisms common to all such kind of systems are presented**.

Now an important equation, i.e. equation 1.24, will be derived. The derivation requires the material discussed in section 1.1.3, and therefore it should be read in parallel with it. So, referring to Figure 1.15, and taking phase a as an example[23],

---

[23]the equations for the other phases are obtained by cyclic permutation of the phase letters a, b and c

the general voltage equation for one of its phases reads :

$$V_A = R_s i_A + L_{AA}\frac{di_A}{dt} + L_{AB}\frac{di_B}{dt} + L_{AC}\frac{di_C}{dt} + e_A \tag{1.16}$$

where V_A is the phase voltage (sign convention shown in Figure 1.15), R_s is the phase resistance, L_{AA} is the self-inductance, L_{AB} and L_{AC} are the mutual-inductances, and e_A is the Back-EMF voltage of phase a. Assuming a symmetrical machine, the self inductance of each phase is equal and the mutual inductance between any two phases is equal :

$$L_{AA} = L_{BB} = L_{CC} = L \tag{1.17}$$

$$L_{AB} = L_{BA} = L_{AC} = L_{CA} = L_{BC} = L_{CB} = M \tag{1.18}$$

Moreover, for a delta-connected motor (as well as for a wye-connected with an isolated neutral) the following holds :

$$i_A + i_B + i_C = 0 \tag{1.19}$$

From equations 1.16, 1.17, 1.18, and 1.19, and expressing the self-inductance L as the sum of the magnetizing and the leakage inductance, i.e. $L = L_{mag} + L_l$, it follows (see appendix B of reference [17]) that the three **voltage equations** become uncoupled :

$$V_A = R_s i_A + ((L_{mag} + L_l) - M)\frac{di_A}{dt} + e_A \tag{1.20}$$

$$V_B = R_s i_B + ((L_{mag} + L_l) - M)\frac{di_B}{dt} + e_B \tag{1.21}$$

$$V_C = R_s i_C + ((L_{mag} + L_l) - M)\frac{di_C}{dt} + e_C \tag{1.22}$$

Further, the back-EMF voltage of a phase can be written as (taking phase A as an example) :

$$e_A = k_{eA}(\theta_r)\omega \tag{1.23}$$

where k_{eA} is the Back-EMF function of phase A, ω the rotor angular speed, and θ_r the rotor angular position in electrical degrees [24]. The maximum absolute value of functions k_{eA}, k_{eB} and k_{eC}, is called Back-EMF constant, and it will be denoted by K_e. K_e is the (absolute) value of the flat portions of the trapezoidal Back-EMF functions e_A, e_B and e_C

---

[24]See section 1.1.1 and pages 60 and 61 of reference [17])

showed in red in Figure 1.21. From all these considerations one can derive an important equation giving a global (i.e. without details of each phase) description of a delta-winded, trapezoidal PMSM driven with six-step commutation. In fact, for each of the six step (modes in Figure 1.21) one can sum the two voltage equations describing the phases which are in series in the given step, then subtract from the resulting equation the remaining voltage equation, and finally take the average of both sides of the resulting equation over one period of the PWM signal [25]. With the help of Figures 1.21 and 1.15, one can deduce that the resulting equation is the same for all six steps, and it reads [26] :

$$V_{avg}^m = \frac{2}{3}R_s I_{avg}^m + \frac{2}{3}((L_{mag} + L_l) - M)\frac{dI_{avg}^m}{dt} + K_e\omega \tag{1.24}$$

in which V_{avg}^m and I_{avg}^m are the average of motor voltage and current, respectively, over one PWM period . **Equation 1.24 is important and it will be used later on in its steady state form** $\left(\dfrac{dI_{avg}^m}{dt} = 0\right)$. **It can be shown that (see section 1.1.3) that** V_{avg}^m **is given by** :

$$V_{avg}^m = DV_{dc} \tag{1.25}$$

in which D **is the duty cycle** of the PWM signal applied to the MOSFETs (MOSFET stands for "Metal-oxide-semiconductor field-effect transistor") gates, and it is defined as $\frac{T_{on}}{T}$, namely as the ratio between PWM on time and the total PWM period.

1.1.3. KDE-UAS95HVC electronic speed controller

From the hardware point of view, the ESC (see Figure 7) is the physical object which implements the sensorless six-step commutation control scheme. Its maximum continuous current and DC supply voltage are 95 A and 52.2 V respectively (these two values are provided by the manufacturer (KDEDirect) itself), and are determined by the power dissipation limit of its MOSFETs (switches). Each one of the three motor phases is driven by a single pair or multiple pairs of high-side and low-side MOSFETs (multiple pairs if multiple MOSFETS are paralleled for each side). When the corresponding high-side MOSFET (MOSFETs if the MOSFETs are paralleled) is active the phase is connected to the supply voltage V_{dc} (see Figure 1.15),

---

[25]For example, in mode 1 one has to subtract 1.21 from the sum of equations 1.20 and 1.22

[26]Notice that since the frequency of the PWM signal is typically of the order of tens of kilohertz, the motor RPM, and so the back-EMF voltages can be considered as constant over a PWM period. In other words, the mechanical part of the system only sees a constant voltage equal to V_{avg}^m in equation 1.24

while it is connected to GND (ground) when the corresponding low-side MOSFET is instead active :
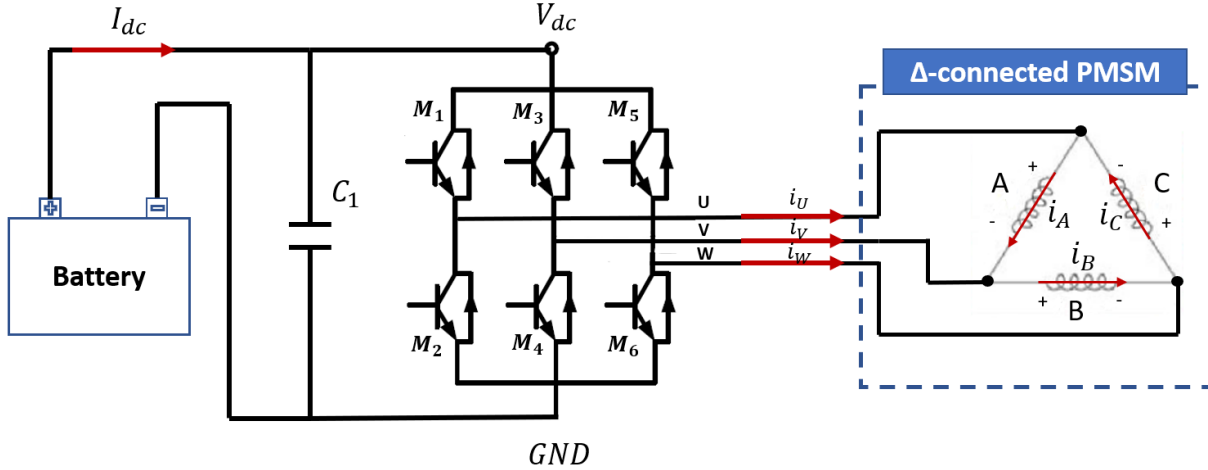

Figure 1.15: Delta winding connection, three phase excitation

KDE-UAS95HVC ESC implements **synchronous rectification**. In standard six-step commutation, during each one of the six states (see section 1.1.1), one MOSFET (or possibly all the ones which are in parallel with each other) is on, the other is modulated with a PWM signal generated from an internal MCU (or FPGA, etc.), and all the other MOSFETs are off. This is shown in Figure 1.16 in which H_U, H_V and H_W are the gate signals of the high-side MOSFETs of motor terminals U, V and W, respectively, while L_U, L_V and L_W are the ones of the low-side MOSFETs of motor terminals U,V, and W respectively. The gate signal waveforms for each one of the six phase sides are reported for each one of the six modes (states). Taking as an example mode 3, Figure 1.17 shows [27] how in the PWM off time the freewheeling current flows through the body diode D2 of MOSFET M_2, and this could lead to high power losses in the diode (see reference [28]), especially for high current applications like the ones considered in this work. Since typically MOSFETs used in these applications have very low R_{dson}[28], the power loss could substantially reduced by switching on MOSFET M_2 during the PWM off time, so that the freewheeling current flows through M_2 [29] instead of through its body diode. **This method is called synchronous rectification, and the corresponding gate signals and the current flow in mode 3 (as an example) are shown in Figures 1.18 and**

---

[27]It should be mentioned that the direction in which the "On Current" is drawn in this Figure assumes that the motor is not in a braking state and that the ripple-current is kept sufficiently small. See article [27], and in particular paragraphs "Braking" and "Input Capacitor". Although the discussion in this article strictly applies to the case of a DC motor, most of the concepts apply also to the case of a PMSM

[28]The equivalent resistance of the MOSFET when it is in the "on" state

[29]Current can flow in both direction through a MOSFET

1.19. Clearly, to prevent both MOSFETs M_1 and M_2 being on at the same time creating a short circuit (shoot-through in jargon), it is necessary to provide for sufficient time [30] (dead-time in jargon) to elapse between MOSFET M_1 being on and MOSFET M_2 being on.
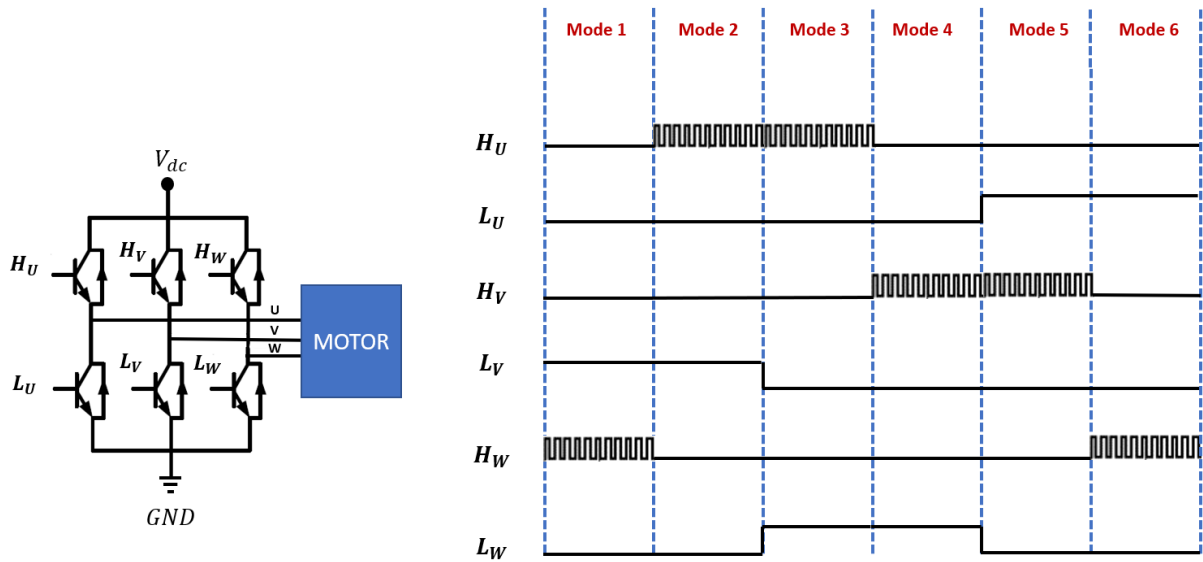

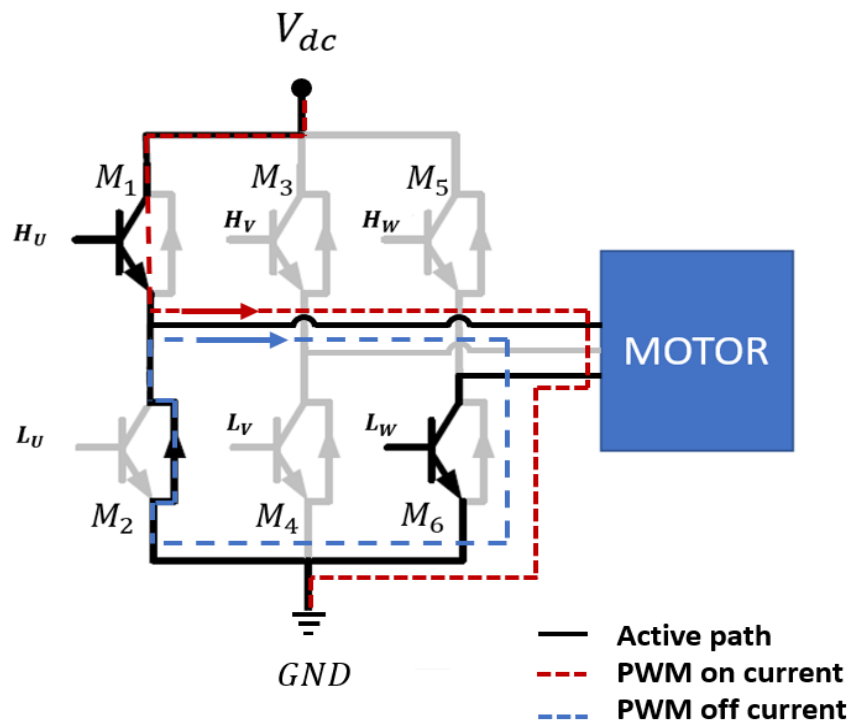
Figure 1.16: Gate signals in standard six-step commutation

Figure 1.17: Current flow in mode 3 during PWM on and of times
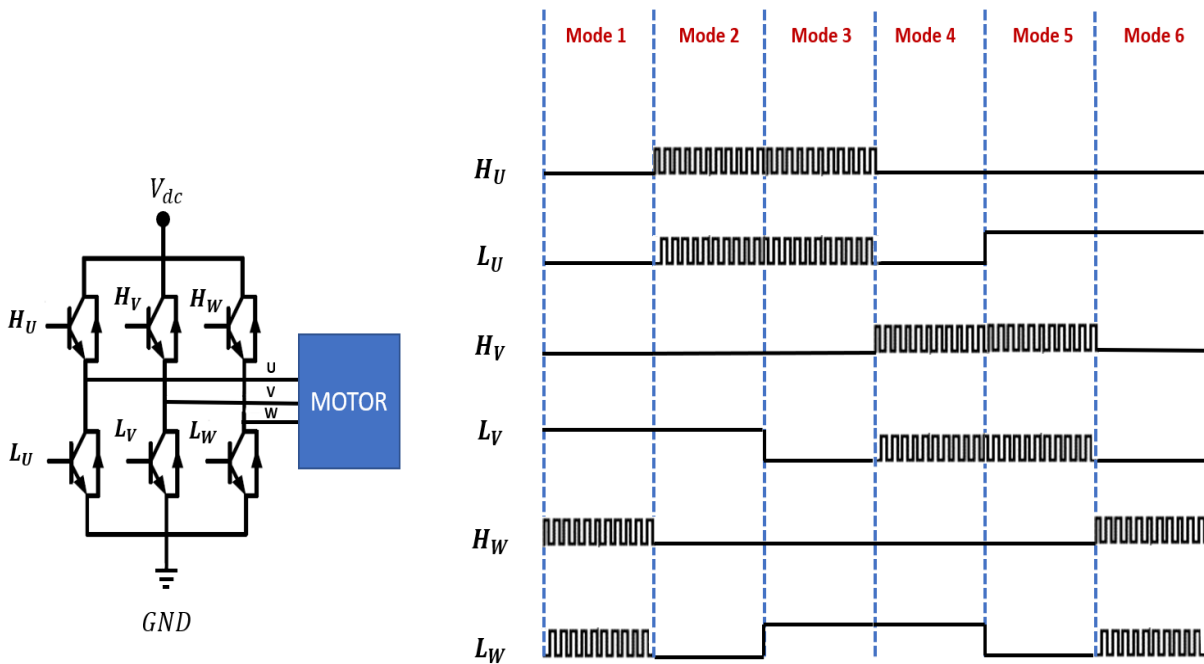
---

[30]In practice this time is very small

Figure 1.18: Gate signals in six-step commutation with synchronous rectification
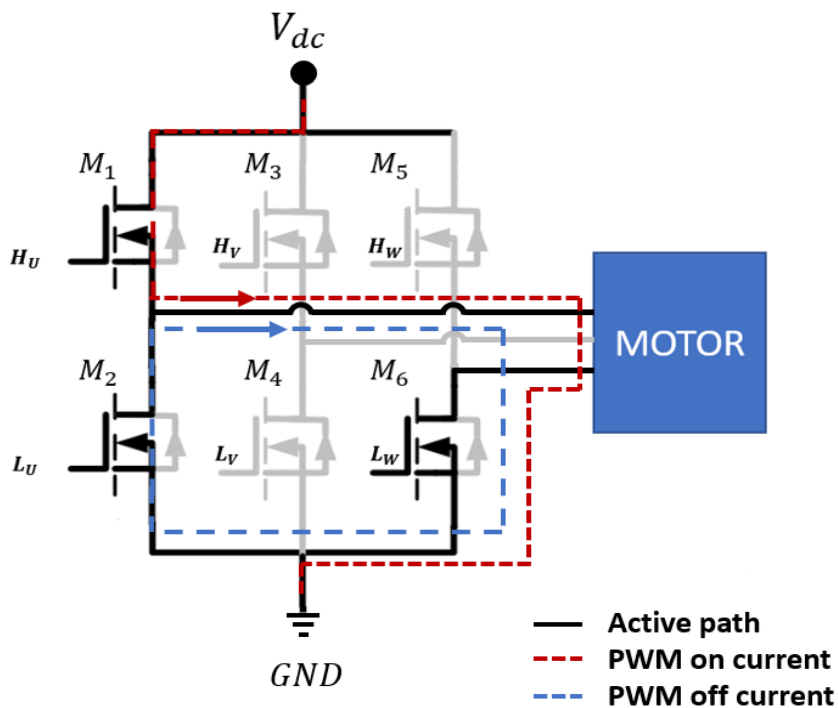
Figure 1.19: Current flow in mode 3 with synchronous rectification

During the PWM on time ("On current" condition in Figure 1.19) all of the three phases are excited, as it is clear from the waveforms of currents i_A, i_B, i_C in Figure 1.21 (see also

reference [15]). This is different from what happens in the six-step commutation scheme for the case of a wye-connected motor, for which only two phases are excited during the PWM on time [31].

However, the six-step commutation switching sequence is the same for both the delta and wye winding connection methods, from which it follows that the three "input line currents" i_U, i_V and i_W in Figure 1.15 have the same waveforms (see Figure 1.20) for both winding connection methods. **It should be mentioned that if the ripple-current is kept sufficiently small by putting properly chosen bulk capacitors on the ESC input terminals (see C_1 in Figure 1.15), the magnitude I_{dc} of these currents, which is nothing more than the DC power supply current, is,to a good approximation, equal to I_{avg}^m defined in equation 1.24. A good explanation of why this is the case can be found in article [27].** [32]

---

[31]This is the reason why the excitation system in Figure 1.15 is called "three phase excitation"

[32]Although the discussion in this article strictly applies to the case of a DC motor, most of the concepts apply also to the case of a trapezoidal PMSM controlled by six-step commutation
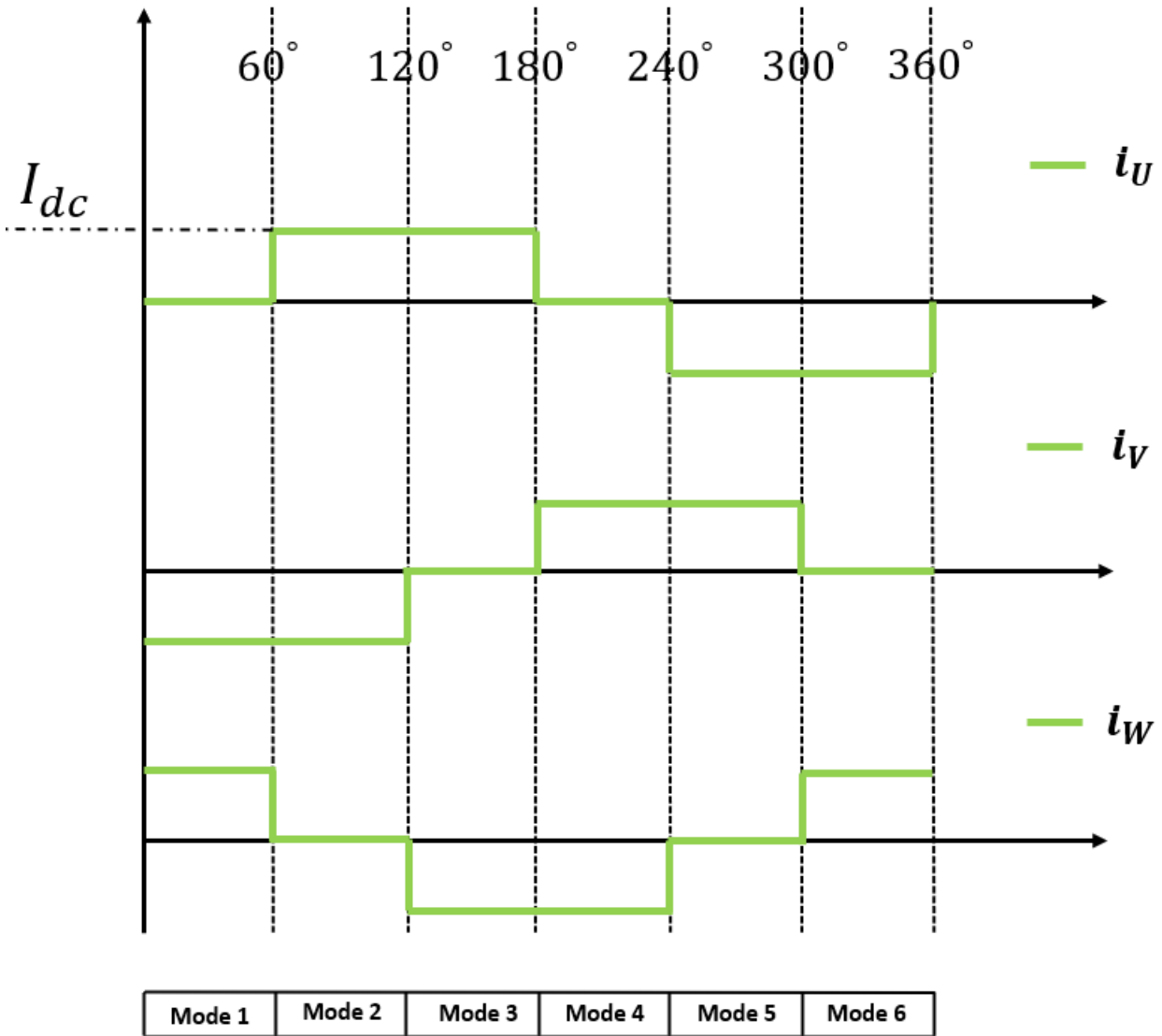
Figure 1.20: Input line currents waveforms of both winding connection methods

It follows that the Back EMF and phase currents for a delta-connected motor driven by six-step commutation are as shown in Figure 1.21 below. Phase currents i_A, i_B and i_C are positive if in the corresponding direction shown in Figure 1.15, and Table 1.1 shows the signs of the three phase currents in each one of the six modes. For each mode the signs associated to the two phases connected in series are highlighted in red. The current waveforms for the case of a wye-connected motor are instead given in Figure 1.5. For more details about six-step commutation see section 1.1.1 and reference [32]
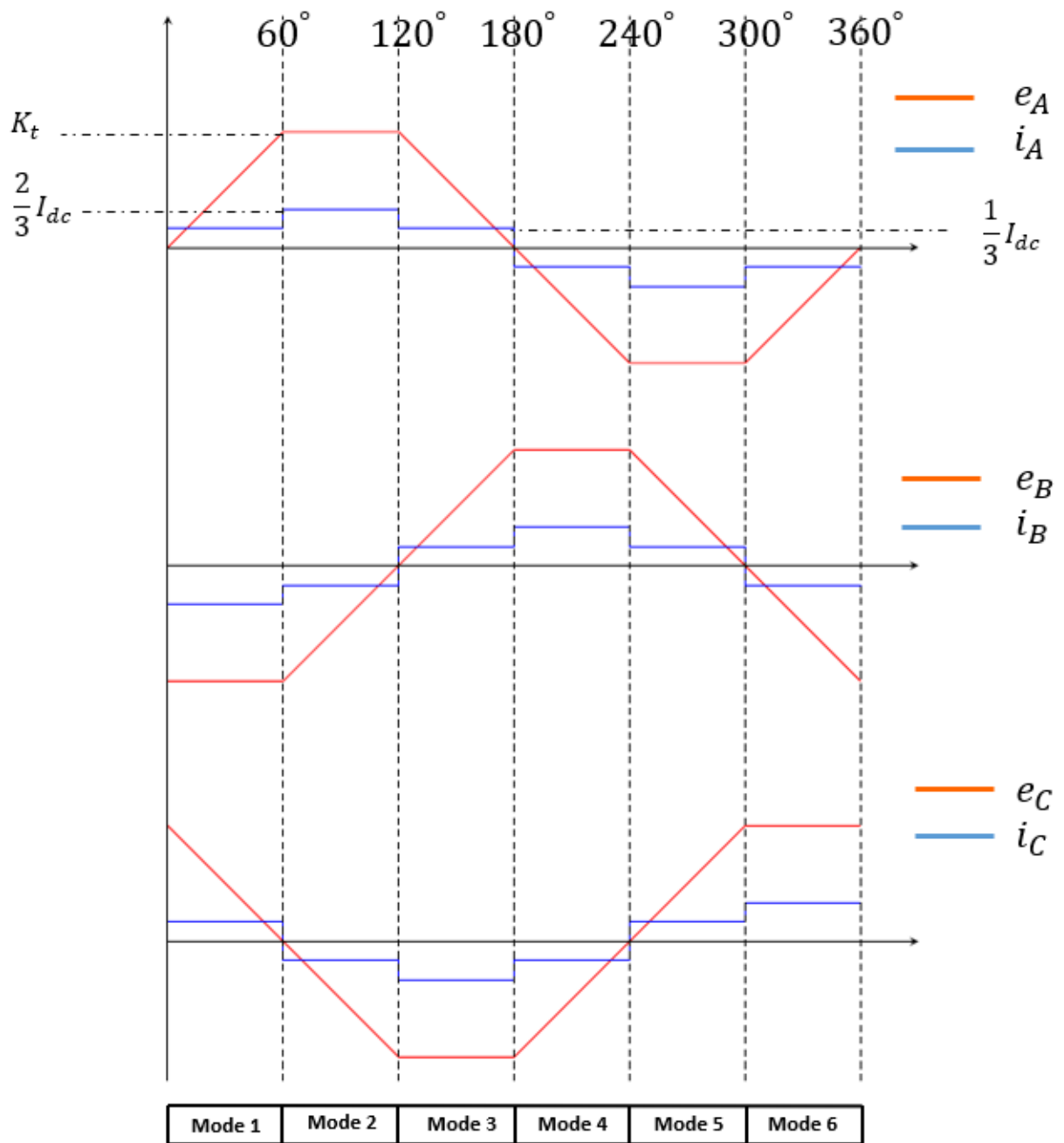
Figure 1.21: Six-step commutation waveforms for delta connection

Current	Mode 1	Mode 2	Mode 3	Mode 4	Mode 5	Mode 6
i_A	+	+	+	-	-	-
i_B	-	-	+	+	+	-
i_C	+	-	-	-	+	+

Table 1.1: Sign of phase currents in each mode

1.2.   The propeller

The propeller shown in Figure 1.22 is made of 3 carbon fiber blades, the overall dimensions and spanwise CG ("center of gravity") position x_{cg} of which are represented in Figure 1.23.

Figure 1.22: Propeller
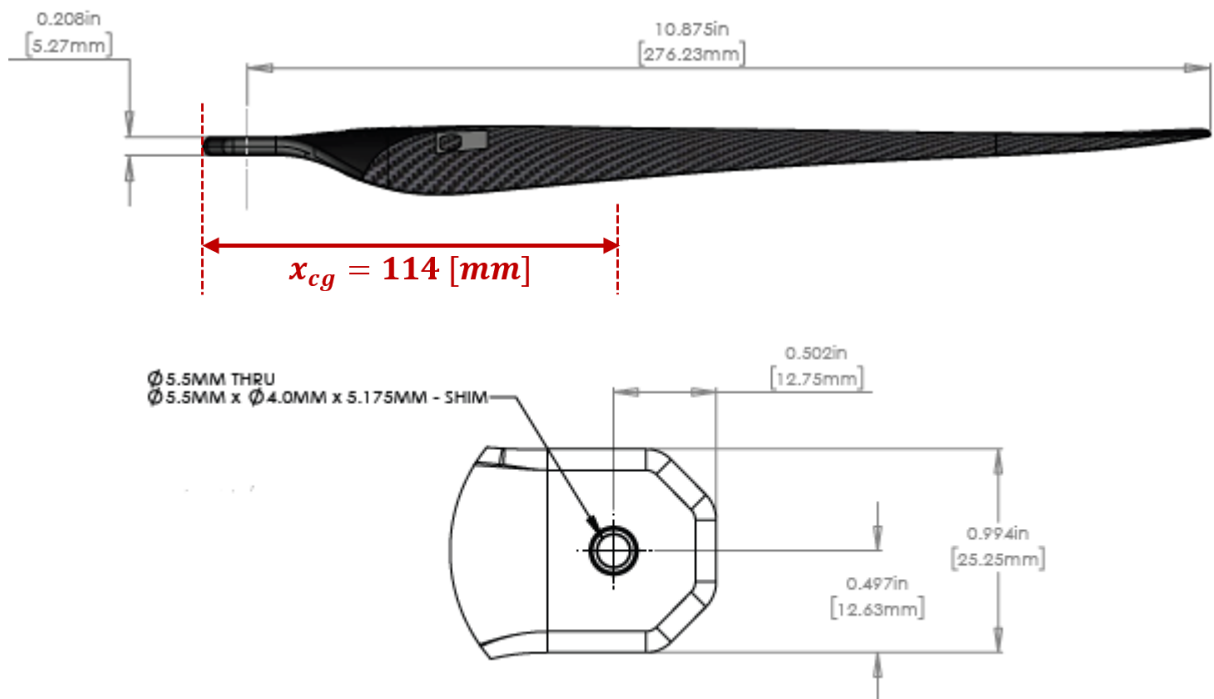
Figure 1.23: Propeller blade (Picture from [4])

The mass of each blade is 35 g, while the mass of the entire propeller as it is shown in Figure 1.22 is 155 g.

The interface between blades and motor consists of a **blade adapter**, which is made of two parts, the first being the **upper plate** indicated by number 5 in Figure 1.24, and a **lower base**, indicated by number 9 in the same Figure. The 3 blades are sandwiched between the **upper plate** and the lower base via the three screws indicated by 1. The tightening torque of these screws should not be so high as to completely prevent the lead-lag motion of the blades. The motor transmits the motion to the blades via the **lower base**, which is attached to it as shown in Figure 1.25 via the four screws indicated by 7. Finally, the four screws indicated by number 3 in Figure 1.24 are for secure retention of the **upper plate**, and should not be overtightened because of the risk of bending the **upper plate**.
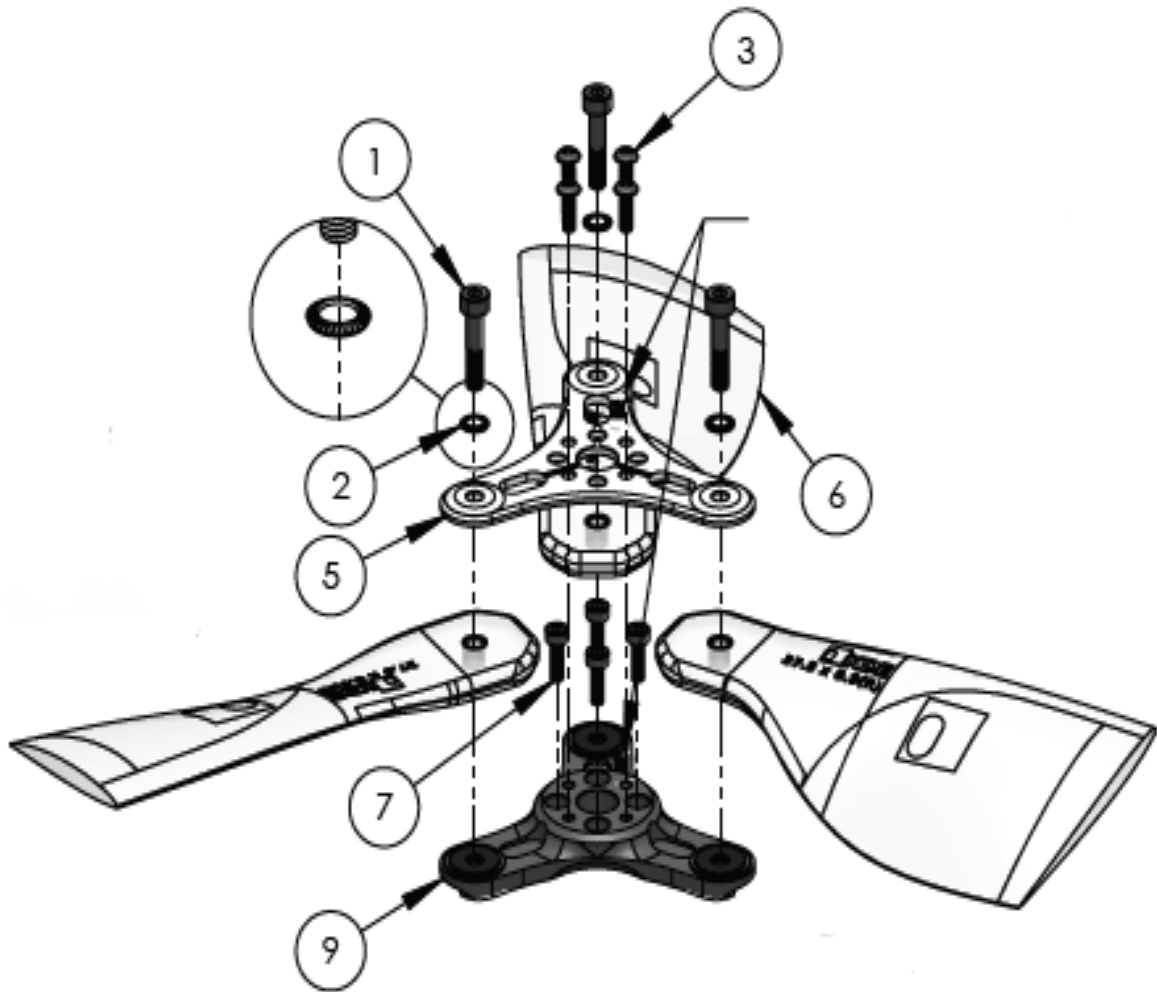
Figure 1.24: Blade to motor interface (Picture from [4])

Figure 1.25: Mounting the adapter on motor (Picture from [4])

2 | Design of the LTU electrical drive system

The test rig has to implement some kind of RPM control, which, in its simplest form, consists in driving a single LTU at reasonably constant RPM. **Specifically the RPM behaviour is considered acceptable if their steady-state oscillations are within 5% of the mean value**. To this end, the circuit, the schematic diagram of which is shown in Figure 2.2 for reference, was designed. The ESC is powered by the DC Power Supply from its positive and negative terminals, and it has two groups of three wires. The orange-red-brown group is for customization, via connection to a computer, of the parameters related to the ESC control algorithms, and it was not used in this work. The other group, the +5V (red), GND (black) and PWM signal (white) group, which is meant to be connected to an RC (Radio Controlled) flight controller, was connected to an Arduino UNO R3 board. An LCD (Liquid Crystal Display), shown in Figure 2.4, and also connected to the Arduino board as shown in the schematic, is used to set the value of the PWM signal duty cycle, and so the RPM value, by means of the UP and DOWN Push Buttons. As it will be explained in section 2.1, using only these three pieces of hardware, i.e. the ESC, the Arduino board (MCU), and the LCD display, an open-loop RPM control was achieved. In fact it is important to mention that our ESC (1.1.3) does not feature any internal speed or torque controller [1].

To measure the LTU RPMs, a custom Hall effect sensor PCB, whose schematic diagram is shown in Figure 2.3, was designed and produced. The sensor can easily communicate with a Microcontroller (e.g. the ATmega328p on the Arduino board), which could then be programmed to achieve a closed-loop RPM control (see Figure 5). The RPM sensor was successfully integrated in the final version of the test rig (the Microcontroller is able read the LTU RPM value from the sensor), but, since the RPMs were satisfactorily constant (see section 2.3) already with an open-loop control, it was not deemed necessary for the sake of this work to program the Microcontroller also for a closed-loop control. **The details of the working mechanisms of the electrical drive system will be**

---

[1]This fact was verified by testing

given in the following sections.

2.1.   Open-loop voltage control scheme

The open-loop voltage control scheme is shown in Figure 2.1. From equation 1.24 in steady state $\left(\dfrac{dI^m_{avg}}{dt} = 0\right)$ one can see that [2] ω, i.e. the LTU RPM, is proportional to V^m_{avg}, i.e. to the average motor voltage, which in turn, from equation 1.25, is proportional to the duty cycle D (for a given supply voltage V_{dc}) of the PWM modulating signals shown in Figure 1.18, which are generated by an **internal** MCU (or FPGA, etc.) and then level shifted and fed to the MOSFETs gates by MOSFET gate drivers. **So, if it is possible to adjust the value of this duty cycle, an open-loop control of the LTU RPMs is achieved. The question now becomes how to adjust the value of the gates duty cycle.** This is done by sending to the ESC a throttle signal, V_{thr} in Figure 2.1 (PWM white cable in the schematic 2.2), which is itself a PWM signal, but it has a much lower frequency [3] than the gates PWM frequency [4], which is typically of the order of tens of kilohertz [5]. **The duty cycle of V_{thr} can be easily generated and adjusted by the user (see section 2.1.1), and it is internally put in a linear relationship with the one of the gates PWM by the ESC**. By default our ESC is expecting a PWM throttle signal of a standard RC radio system, with on time period T_{on}, called **"pulse"** in jargon, between 1100 μs, corresponding to 0% throttle [6], and 1940 μs, corresponding to "full (100%) throttle" [7].

In the default throttle calibration mode [8], the 0% pulse, T_{arm} ("arming pulse"), can be redefined to some value in the range [800 1250] μs, but the pulse range is kept equal by the ESC to the standard one, T_{std}, of 840 μs (1940-1100). Therefore, the 100% pulse, T_{full}, is then internally and automatically set to be :

$$T_{full} = T_{arm} + T_{std} \tag{2.1}$$

However it turns out that when the throttle range is redefined while using an Arduino

---

[2]For the sake of this discussion, the term $\frac{2}{3}R_s I^m_{avg}$ can be neglected being R_s typically of the order of 0.1Ω

[3]The maximum frequency tolerated by the ESC described in section 1.1.3 is 600 Hz)

[4]The gates PWM signals have also a greater amplitude, typically greater than +10 V for MOSFETS

[5]For example, for our ESC, the gates PWM frequency is adjusted dynamically between 16 to 18 Khz in "Dynamic mode"

[6]i.e. to a gates PWM with $D = 0$

[7]i.e. $D = 1$ and the full supply voltage V_{dc} is applied to the motor

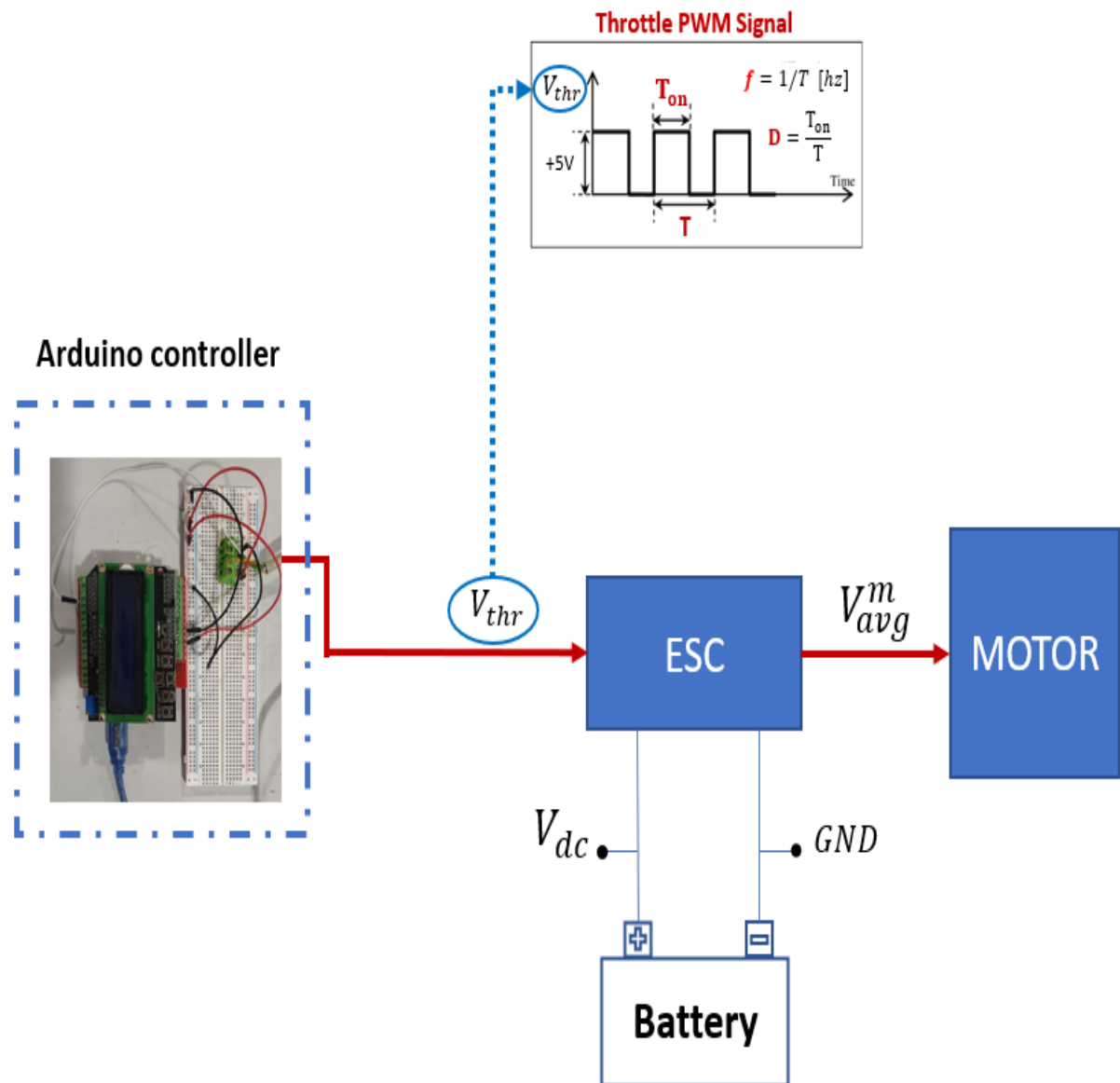[8]The default throttle calibration mode is called "dynamic" by the ESC supplier
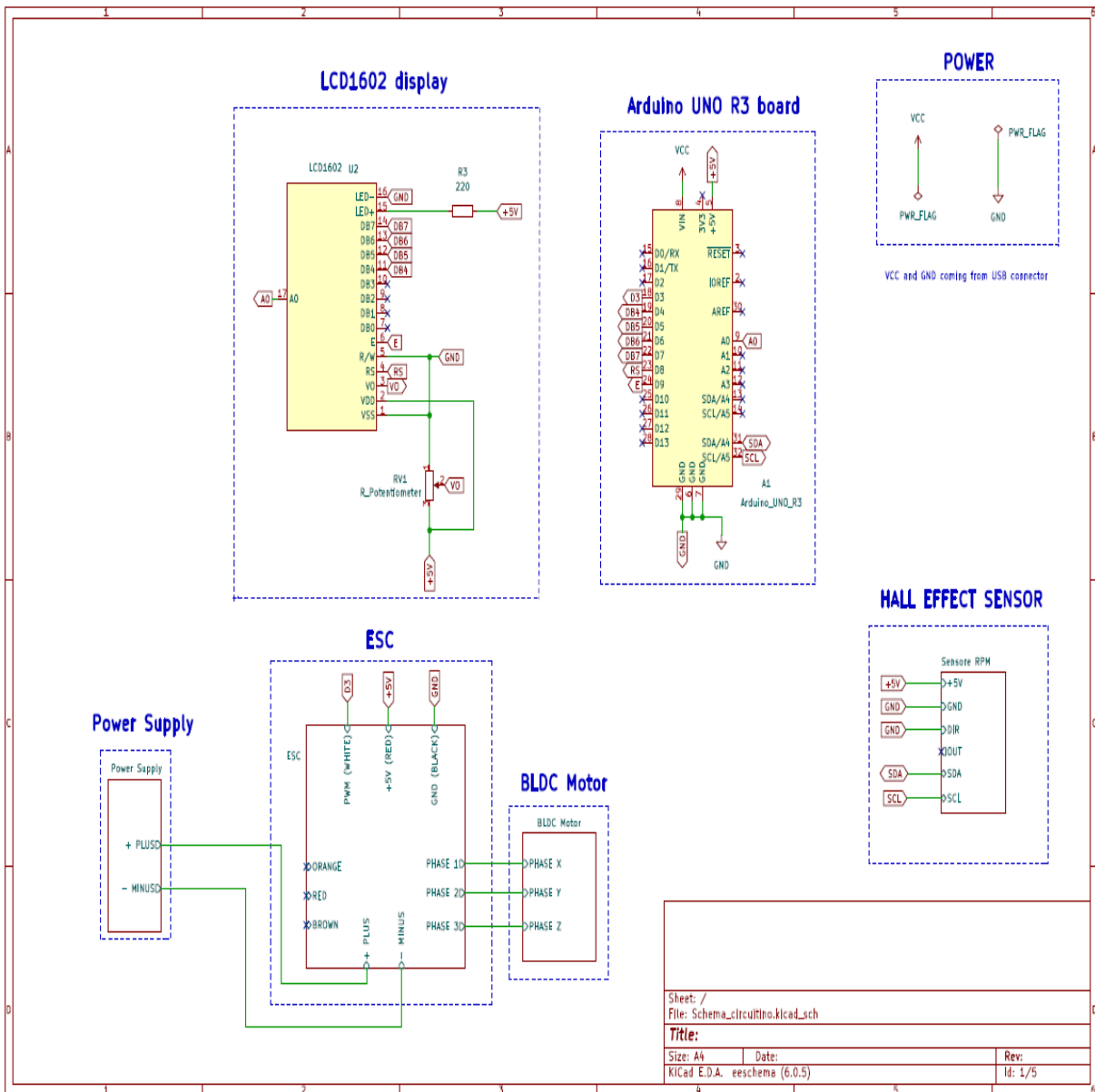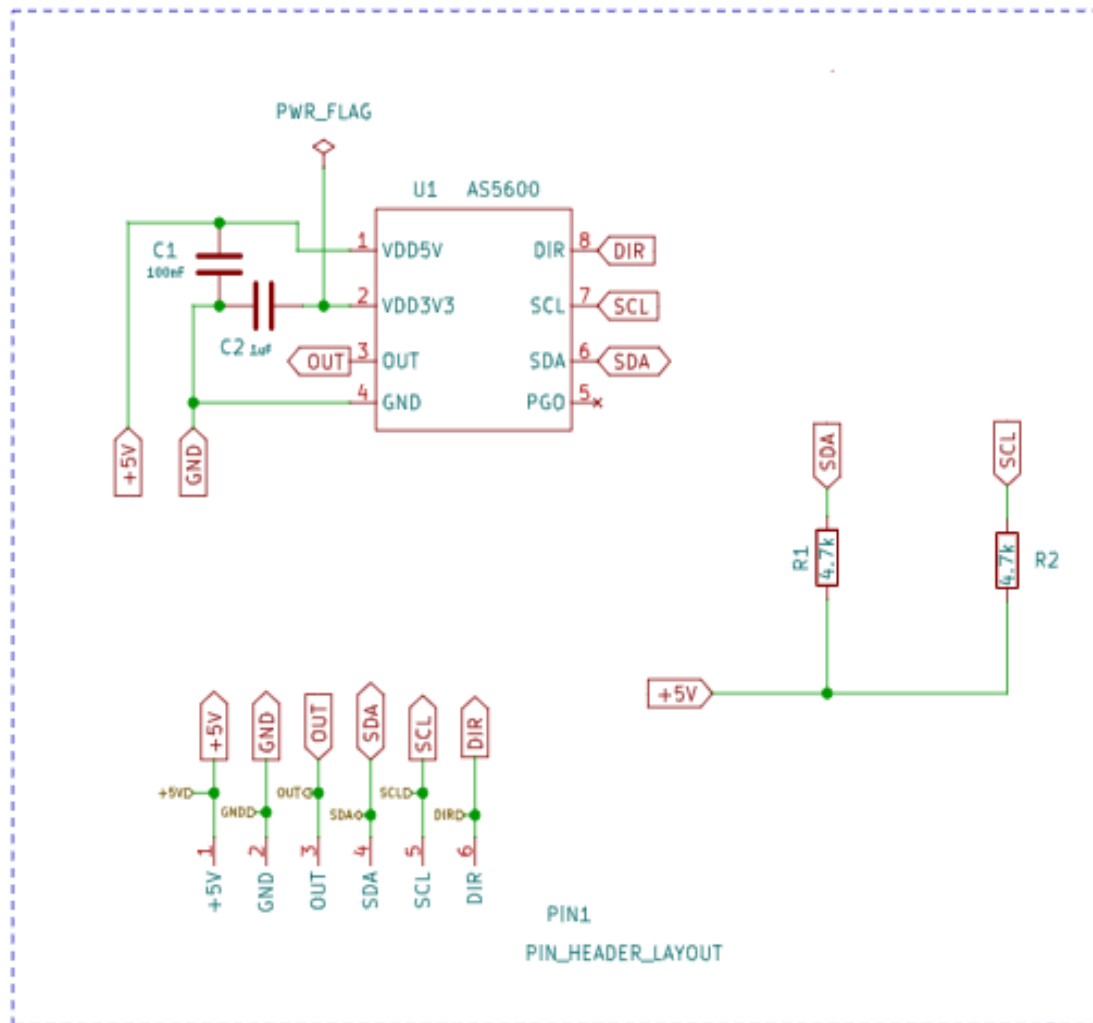
Figure 2.1: Open-loop voltage control scheme

Figure 2.2: Overall drive system schematic

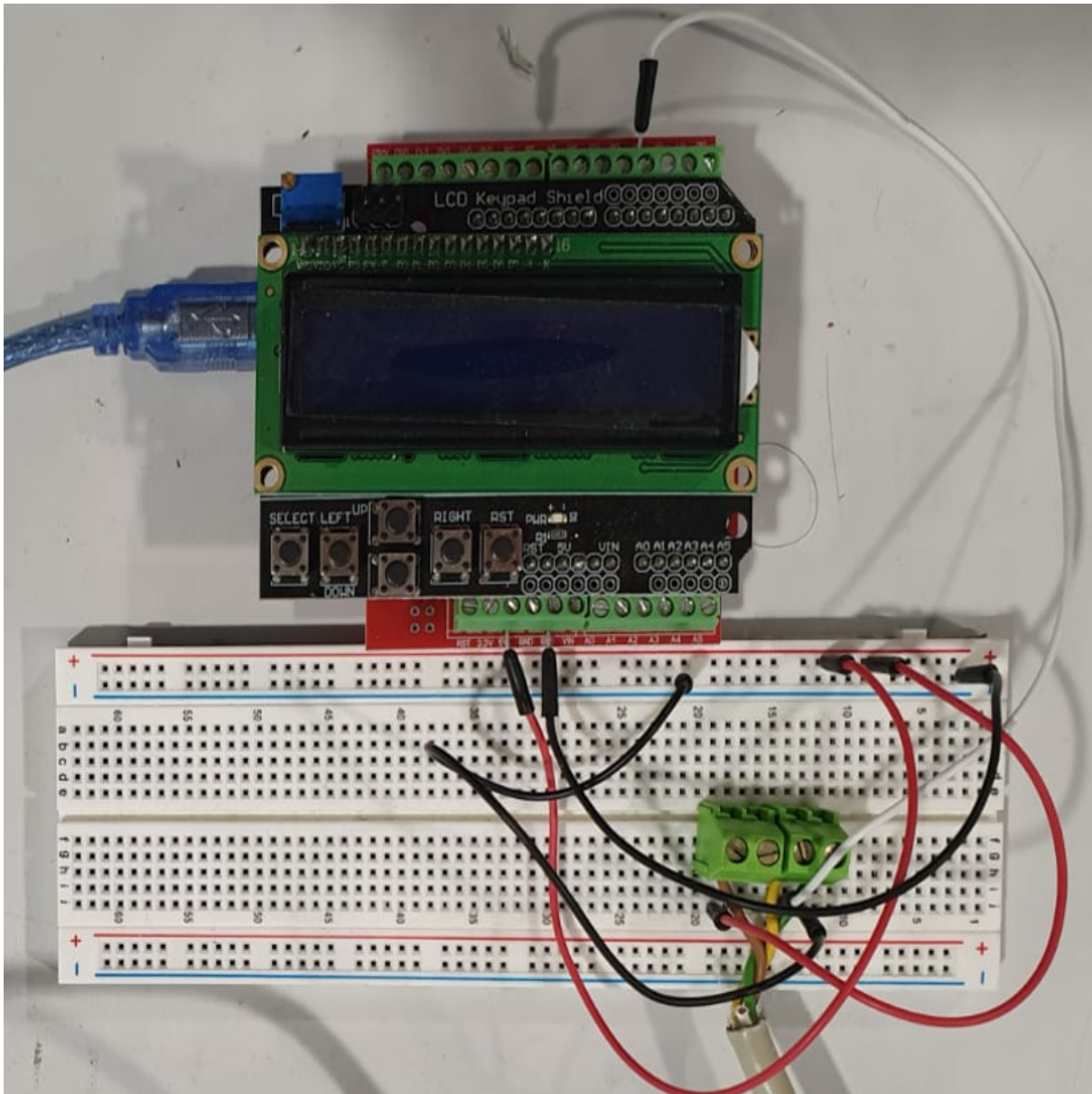Figure 2.3: Hall effect sensor PCB schematic

Figure 2.4: LCD Keypad Shield

board (as shown in section 2.1.1), the motor spinning pulse, T_{sp}, i.e. the pulse at which the motor actually starts spinning at the minimum possible RPMs (minimum possible applied voltage), is internally set to be :

$$T_{sp} = T_{arm} + 160 \tag{2.2}$$

i.e., 160 μs are added to T_{sp}. The consequence of this is that at T_{full} one is not applying the full supply voltage V_{dc} even though according to the ESC we are at 100% throttle. Therefore, once, by increasing the duty cycle with the LCD UP button (see section 2.1.1), the pulse of V_{thr} reaches the value of T_{full}, the LTU RPM value does not increase anymore, even if it should. To solve this issue, it is sufficient for example to change the ESC throttle calibration mode to "range" (via the ESC "Device manager adapter") and insert manually the values of T_{sp} ("MIN" value) and T_{full} ("MAX" value) [9].

To generate and adjust the throttle signal V_{thr} it was decided to use an Arduino Uno R3 board, which was programmed as discussed in section 2.1.1

2.1.1. Arduino sketch for open-loop motor control

Referring to the code listed below, the "LyquidCrystal" library is first of all included to communicate more easily with the LCD display. In line 9 the variable "val" is initialized to store the value of the voltage output A_0 (see schematic) from the LCD. Then, in line 13, a variable of type "LyquidCrystal" is created on pins 8, 9, 4, 5, 6, and 7. The first number defines the number of the Arduino pin to which the RS ("Register Select") pin [10] (see schematic 2.2) of the LCD is connected. The second number defines the number of the Arduino pin to which the EN ("Enable") pin of the LCD is connected, and its function is described in reference [5]. The last four pin numbers define the data pins for receiving and sending the data [11]. Then, in line 17 the on time of V_{thr} is set equal to 102, which means a duty cycle D of :

---

[9]The values inserted have to be both within ranges specified by the manufacturer

[10]When this pin is set (by the LiquidCrystal display library) "high" the "Data register" is selected, while when it is "low" the "Command Register" is instead selected. The function of these two registers is described in reference [5]

[11]The LCD may also communicate with the MCU by means of eight data lines instead of four. But typically, as it was done in this work, the 4-bit mode is used, and in this mode the remaining four data lines are left unconnected as shown in the schematic 2.2. It should also be mentioned that the RW (Read/Write) pin was connected to GND (see 2.2). This pin must be set "low" or "high" depending on whether one has to write or read from either the "Command" or "Data" register. Since the LiquidCrystal display library, when configured by six parameters, doesn't require reading from the registers (see reference [10]), the RW can indeed be connected to GND

$$D = \frac{102}{255} = 0.4 \tag{2.3}$$

Since the default frequency of the PWM signal generated on the chosen pin "3" is 490 Hz [12], this means that T_{arm} (see section 2.1) is set equal to roughly 816 μs.

Then, in the **"void setup"** the LCD is initialized as a 2x16 (rows by columns) matrix of characters and it is cleared. In line 27 pin 3 is configured as an output pin because it is the pin on which the PWM signal V_{thr} will come out from.

In the **"void loop"** the variable "val" is first of all updated with the current analog value (from 0 to 1023) of A_0. From this value, it is possible to understand which one of the five Push buttons (UP, DOWN, LEFT, RIGHT, and SELECT. See 2.4) connected to the A_0 voltage pin was pressed [13]. For example, if $50 \leq$ val ≤ 150, than the UP button was pressed. **Then, depending on whether the "UP" or "DOWN" button has been pressed, the variable is increased or decreased by 1**, and this is followed by a delay of 200 milliseconds to "slow down" the switch (lines 42 and 48). Moreover, the display is cleared. In lines from 51 to 55 the program makes sure that the duty cycle does not go outside the interval $102 \leq$ val ≤ 255. In line 58 a PWM signal (V_{thr}) of on time corresponding to "pwm_value" is outputted to Arduino pin 3, and finally, in lines from 61 to 63, "pwm_value" is printed on the LCD .

```
1
2 // Include libraries for LCD Display
3 #include <LiquidCrystal.h>
4
5
6 // PWM output pin
7 #define pwm      3
8
9 int val = 0;
10
11
12 // Define LCD display connections
13 LiquidCrystal lcd(8, 9, 4, 5, 6, 7);
14
15
```

---

[12] As specified in the Arduino Uno datasheet

[13] This is because the A_0 pin of the LCD is the output of a five stage voltage divider, as shown in the schematic in reference [9]

```
16  // Variable to represent PWM value
17  int pwm_value = 102; //102
18
19
20  void setup(){
21
22    // Setup LCD
23    lcd.begin(16, 2);
24    lcd.clear();
25
26    // Define Pins
27    pinMode(pwm,OUTPUT);
28
29  }
30
31  void loop()
32  {
33    {
34
35      // Memorizza in val il valore presente su A0
36      val = analogRead(A0);
37
38
39      // Increase motor speed if UP button pressed
40       if (val >= 50 && val <= 150){
41        pwm_value=pwm_value+1;
42        delay(200);
43        lcd.clear();}
44
45      // Decrease motor speed if DOWN button pressed
46      else if (val >= 150 && val <= 300){
47        pwm_value=pwm_value-1;;
48        delay(200);
49        lcd.clear();}
50
51      // Ensure PWM value ranges from 0 to 255
52      if(pwm_value>255)
```

```
53        pwm_value= 255;
54     else if(pwm_value<102)
55        pwm_value= 102;
56
57     // Send PWM to output pin
58     analogWrite(pwm,pwm_value);
59
60     // Display results on LCD
61     lcd.setCursor(0,0);
62     lcd.print("PWM:");
63     lcd.print(pwm_value);
64   }
65 }
```

2.2.   Design of the RPM sensor

The general idea is shown in Figure 2.5. As it should be clear from the description given in section 1.1.2.1, the black button head screw (also shown in Figure 1.14) rotates together with the rotor and is magnetic. So, one can attach to it [14] a small discoidal magnet (indicated with "M" in the Figure) whose angular position is detected by an Hall effect sensor placed underneath it.

---

[14]at its center with some glue
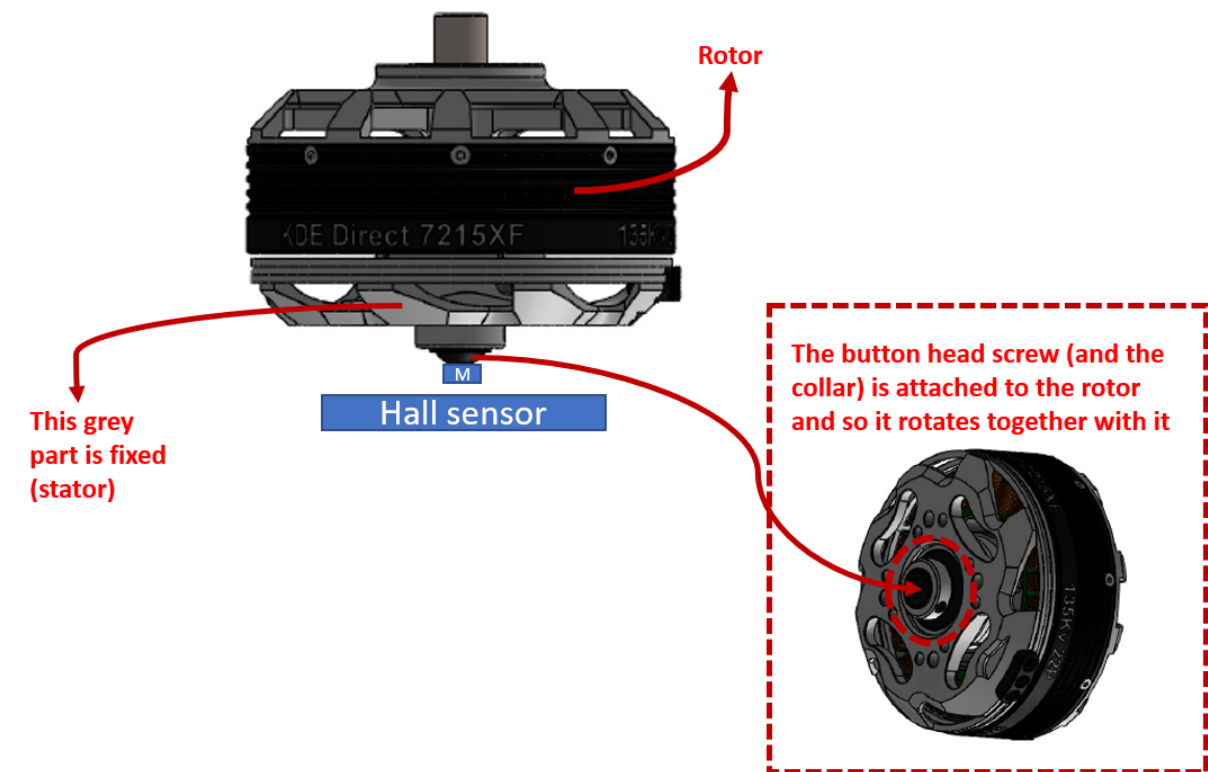
Figure 2.5: RPM sensor concept

Now, keeping in mind that the Hall sensor has to fit inside a tiny space in a mechanical interface (see for example the "6A80_C interface" in Figure 3.26) between the load cell and the LTU, it is essential for it to be as small as possible [15]. A possible (cost-effective) solution was found in the AS5600 IC (Integrated circuit), which is a 12-bit contactless **potentiometer** (angular position sensor). This tiny IC, shown in Figure 2.6, (6 x 4.9 mm in plane dimensions and maximum thickness of 1.75 mm), measures the **absolute angle** of a **diametrically** [16] magnetized magnet.

---

[15]Besides of course having the desired resolution, accuracy and sampling rate

[16]A "standard" axially magnetized magnet would not work
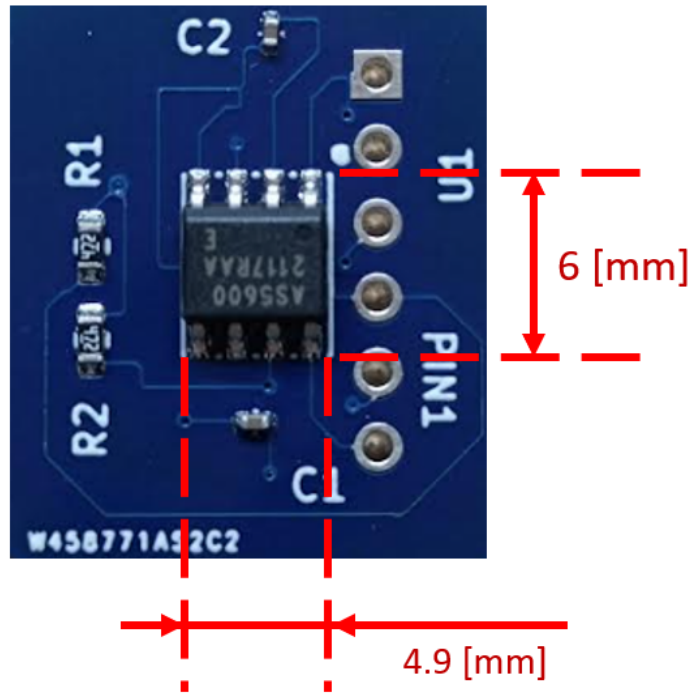
Figure 2.6: AS5600 IC package dimensions

Its functional block diagram is described in some detail on page 9 of its datasheet [1]. The important points for our applications are instead the following :

- It has a 12-bit resolution[17], an ADC (Analog to Digital Converter) Integral Non-Linearity (INL) of ∓ 1 degree [18], and a sampling rate which is not greater than 150 μs (sampling frequency which is not less than roughly 6600 Hz)

- There are three ways to communicate with the sensor. One can choose between the analog output and a digital PWM output, or alternatively, it can read the angle via I2C (Inter-Integrated Circuit communication protocol)

- The chip can be powered either from a 5.0 V or a 3.3 V supply, and it is programmed via I2C.

- The chip can be programmed for different angular ranges, but the default one of [0 360°] is perfectly good for our application

- The vertical distance between the surface of the chip and the magnet is typically between 0.5 and 3 mm and an optimal value can be found by communicating with

---

[17]Which, in terms of degrees, is a resolution of 0.087890625°

[18]If communication with the sensor is by means of its analog output, one has also to take into account both the integral and the differential non linearity of the "Digital to Analog Converter", a.k.a DAC (which are $\mp 5LSB$ ("Least Significant Bit") and $\mp 1LSB$ respectively)

the chip (via the I2C protocol). The displacement of the rotational axis of the magnet from the center of the chip must not exceed 0.25 mm

- Of course the chip has to be mounted on (custom) PCB and it requires external capacitors and resistors

The specified resolution, accuracy, and sampling frequency were deemed appropriate for the application and the mounting requirements not too stringent. Therefore, a custom PCB, shown in Figures 2.7 and 2.8 was designed and produced :
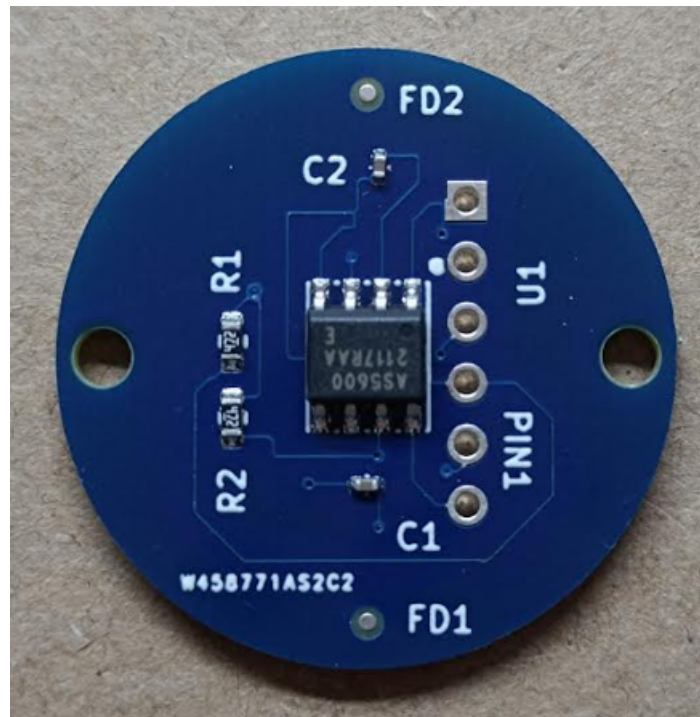
Figure 2.7: Hall sensor custom PCB
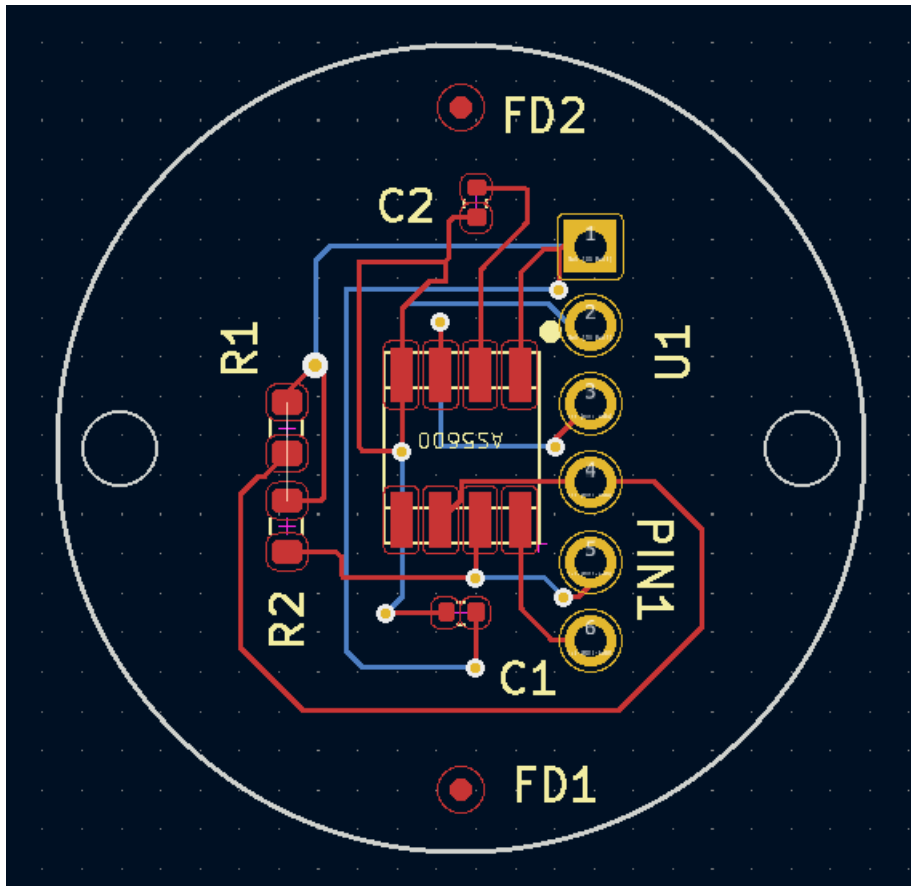
Figure 2.8: PCB routing

2.2.1. PCB schematic and code

The PCB was designed with the main objective of keeping it as compact as possible. To get the angular position, one can easily and directly use the analog output (which the default output mode) as explained in the datasheet. However, it is possible to get the angular position by reading/writing to the appropriate chip registers via I2C. Reading/writing to the registers is also necessary to find the optimal vertical distance from magnet to chip, as well as to change the output mode from analog to PWM. **To read/write to the registers via I2C a firmware was written in the form of an Arduino sketch. The code is not reported here, but the conceptual steps are the following :**

- **Check that the vertical distance between the magnet and the chip is optimal, or at least acceptable**

- **Read the raw angle from the registers and convert it to an angle in degree**

- **Calculate the LTU RPMs by taking the difference between the current and the previous angle reading and dividing it by the time interval be-**

tween the two [19]

2.2.2. Testing the Hall sensor PCB

To test the designed PCB, a series of tests on the motor alone (without the mounted propeller) was performed in which the average of its RPM readings was compared to the RPM reading obtained with a microphone (see Figure 2.9). The duty cycle of the throttle signal V_{th} was varied (see section 2.1), and so the motor RPM value was varied, between each test from the lowest to the highest range. The microphone was placed in such a way to detect the acoustic pressure pulses associated with the 10 motor groves indicated on the Figure. The average motor RPM according to the microphone can then calculated as follows :

$$\Omega = 60 \left(\frac{f_{pk}}{10} \right) \tag{2.4}$$

in which f_{pk} is the frequency in [hz] of the peak of the magnitude spectrum of the microphone output signal.

---

[19]The time interval between two consecutive angular readings is computed by using an internal AT-mega328p (which is the Arduino MCU) timer
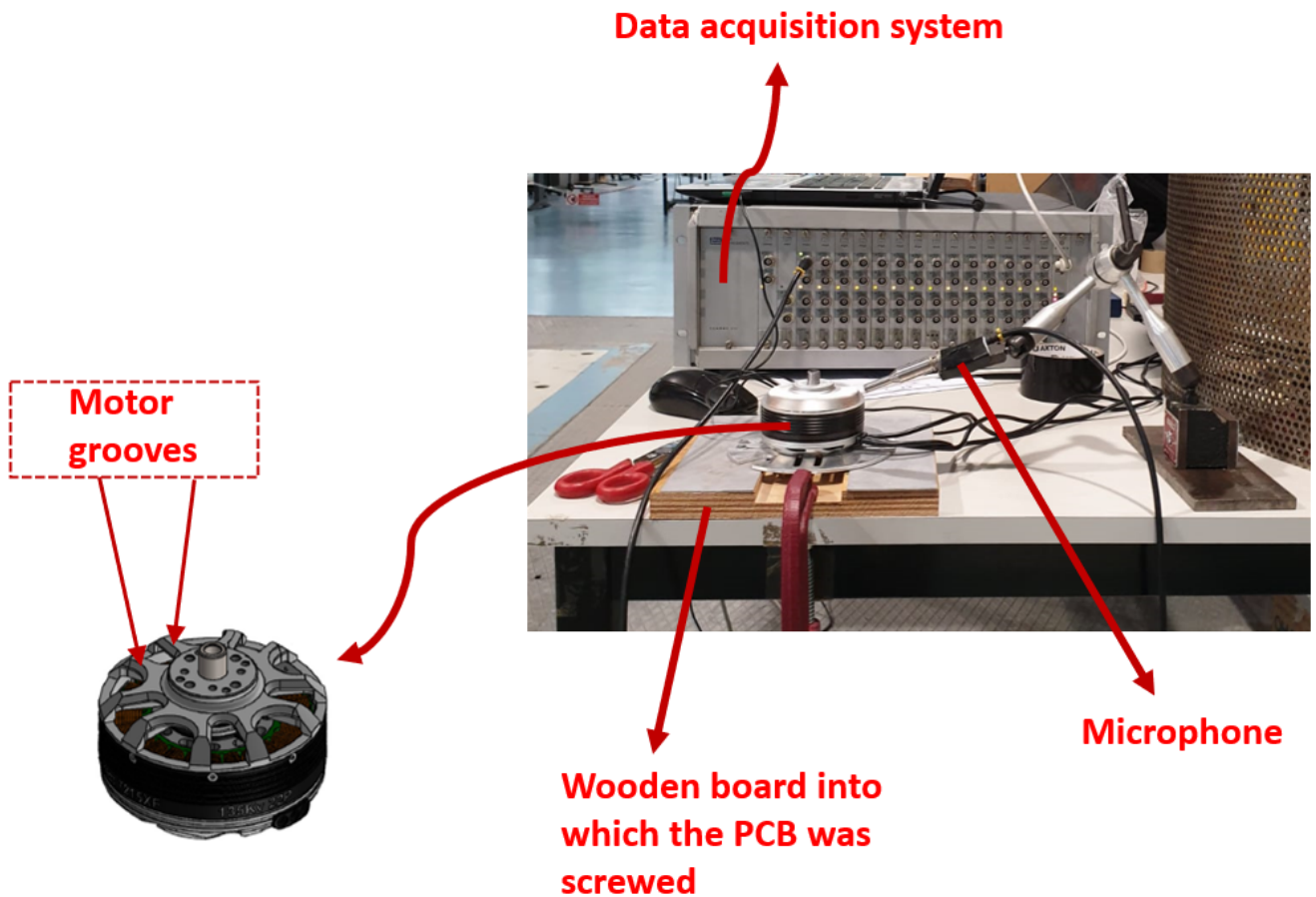
Figure 2.9: PCB microphone test

These tests showed a good agreement between the two average RPM values, with a discrepancy of less than 5% over the entire RPM/duty cycle range. Moreover, the Hall sensor readings showed only a small ripple in the motor RPM signal (see section 2.3), even without adopting "heavy" filtering techniques on the RPM signal. This fact was later also verified with totally analogous tests on the complete LTU (motor with propeller mounted). These results are the reason why it was not deemed necessary for the purpose of this work to program the MCU also for a closed-loop RPM control.

2.2.3. PCB mounting on the 6A80_C interface

The "6A80_C" interface [20] (see section 3.4) was designed to accommodate the custom PCB. 2.10 shows the mounting concept, while in Appendix A one can find the detailed mechanical drawing of the interface.

---

[20]It is the mechanical interface (between load cell and LTU) which was designed for the last load cell-based measurement system
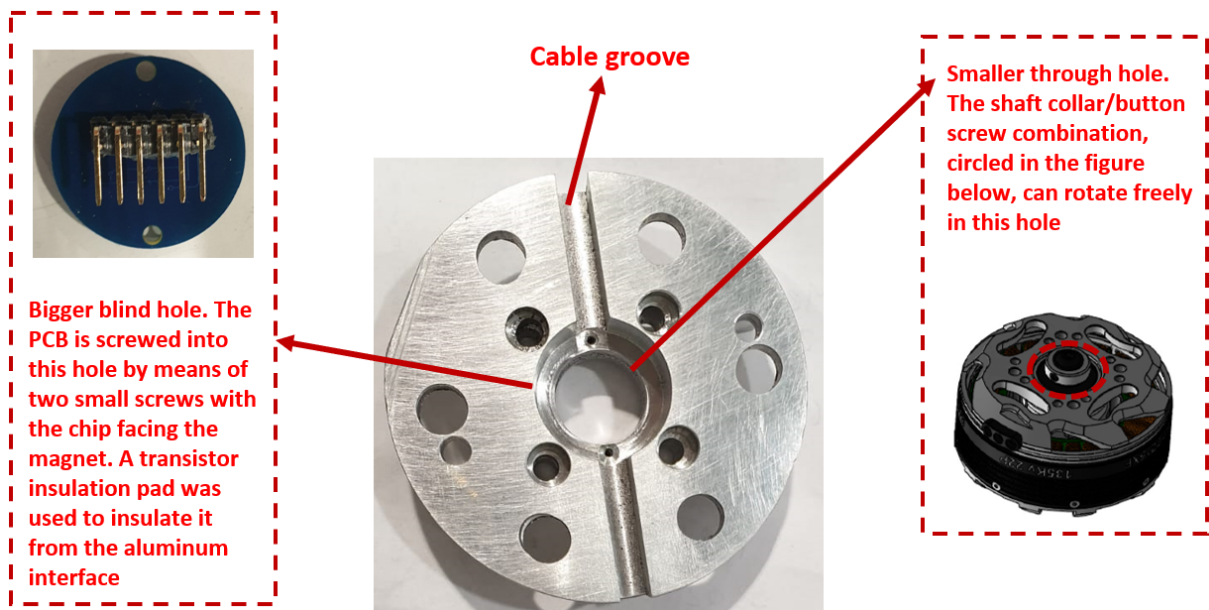
Figure 2.10: PCB mounting concept

2.3. RPM measurement

Several tests were performed to measure the motor RPM at different values of the duty cycle D. The RPM value was calculated on a time interval of 0.2 seconds reading the motor angular position via I2C. As an example, Tables 2.1, 2.2 and 2.3, which are relative to different and increasing values of D, are reported below to show both the RPM data and the results in terms of mean and variance.

Time [s]	RPM
0.0	2116.37
0.2	2109.22
0.4	2089.71
0.6	2080.59
0.8	2089.91
1.0	2100.12
1.2	2121.61
1.4	2089.86
1.6	2085.25
1.8	2104.92
2.0	2090.95
2.2	2106.65
2.4	2135.83
2.6	2089.91
2.8	2084.89
3.0	2130.80
3.2	2090.23
3.4	2081.16
3.6	2089.14
3.8	2110.90
4.0	2090.43
4.2	2101.99
4.4	2104.01
4.6	2121.06
4.8	2090.07
5.0	2085.41
5.2	2104.48
5.4	2119.66
5.6	2072.45
5.8	2112.20
6.0	2191.21
6.2	2118.21
μ	**2103.41 RPM**
σ	**22.4213 RPM**

Table 2.1: RPM data at low duty cycle

Time [s]	RPM
0.0	2980.62
0.2	3017.21
0.4	3009.08
0.6	3011.55
0.8	3047.06
1.0	2997.93
1.2	3002.49
1.4	3027.36
1.6	3006.84
1.8	3003.42
2.0	3004.15
2.2	3036.48
2.4	2991.50
2.6	3009.33
2.8	3022.49
3.0	3045.81
3.2	3006.01
3.4	2989.12
3.6	3029.44
3.8	3021.35
4.0	3016.07
4.2	3007.46
4.4	3048.09
4.6	3007.98
4.8	3004.04
5.0	2999.07
5.2	3027.54
5.4	3014.20
5.6	3005.39
5.8	3019.17
6.0	3004.35
6.2	3008.71
μ	**3013.16 RPM**
σ	**16.1848 RPM**

Table 2.2: RPM data at intermediate duty cycle

Time [s]	RPM
0.0	3587.89
0.2	3552.24
0.4	3592.87
0.6	3543.95
0.8	3590.76
1.0	3577.11
1.2	3560.53
1.4	3583.75
1.6	3577.94
1.8	3563.02
2.0	3581.26
2.2	3563.53
2.4	3598.67
2.6	3565.51
2.8	3581.26
3.0	3582.92
3.2	3579.60
3.4	3565.51
3.6	3584.16
3.8	3582.92
4.0	3582.92
4.2	3564.68
4.4	3602.82
4.6	3583.75
4.8	3580.43
5.0	3566.83
5.2	3601.99
5.4	3563.02
5.6	3582.09
5.8	3582.09
6.0	3581.26
6.2	3562.19
μ	**3577.17 RPM**
σ	**13.8894 RPM**

Table 2.3: RPM data at high duty cycle

3 | Design of the load cell-based measurement system

3.1. Objective and initial load cell selection

In order to **measure all the six dynamic components of LTU force and moment**, it was first of all necessary to design a load cell-based measurement system having a good dynamic behaviour over the entire frequency range of interest. **This range was established by the objective to be able to accurately measure at least the 3/rev harmonic component of each of the six signals. Since the maximum angular speed achievable by the bigger LTU is 5000 RPM (see section 1.1.2.2), the maximum frequency of its 3/rev harmonic component is 250 Hz. For this reason, the frequency range [0, 250] Hz was established as the one of interest.** The dynamic behaviour of such a measurement system is defined [1] by six "Frequency response functions" between the six applied, reference force/moment components and those measured by the load cell. Ideally, each of these FRFs ("Frequency response functions") should be of unit magnitude and zero phase over the entire frequency range of interest. The FRFs are not only the result of the mechanical characteristics of the load cell alone, but of those of the entire system, i.e. load cell (cells) plus the necessary mechanical interface between the motor and the load cell (cells).

From the point of view of the frequency response, the best commercially available option to measure the six components of dynamic loads is a **6-axis piezoelectric load cell** (see Figure 3.1a) consisting of very rigid, large-area quartz disks, but due to the design objective of keeping the overall design cost low (see introduction), the **six-axis strain gauge load cell** shown in Figure 3.1b was tentatively chosen. The coordinate axes and origin are shown in Figure 3.2. The X-axis is determined by the right hand-rule, while the coordinate origin is at the center of the contact plane. The main characteristics of the 6ADF80 are :

---

[1] When it can be considered linear

- Overall diameter 80 mm and height 40mm

- Mass 320 g

- Static measurement range 100 N for the F_X and F_Y force components, 200 N for the F_Z component and 10 Nm for all the three moment components

The risk associated with the choice of this load cell was that only its static characteristics in the form of a static calibration matrix were provided by the manufacturer. In fact, no experimental data was available to prove the suitability of its frequency response in the frequency range of interest.
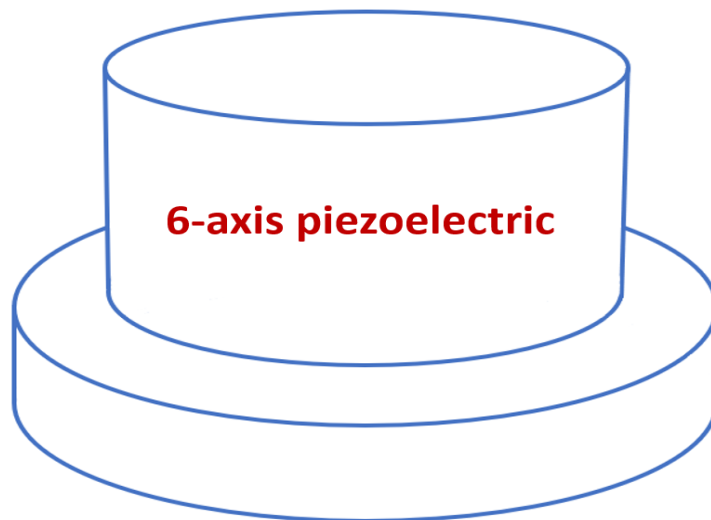
(a) 6-axis piezoelectric cell. Very good FR (Frequency response) but expensive

(b) 6-axis strain gauge cell. It was tested for frequency response

Figure 3.1: Initial load cell options
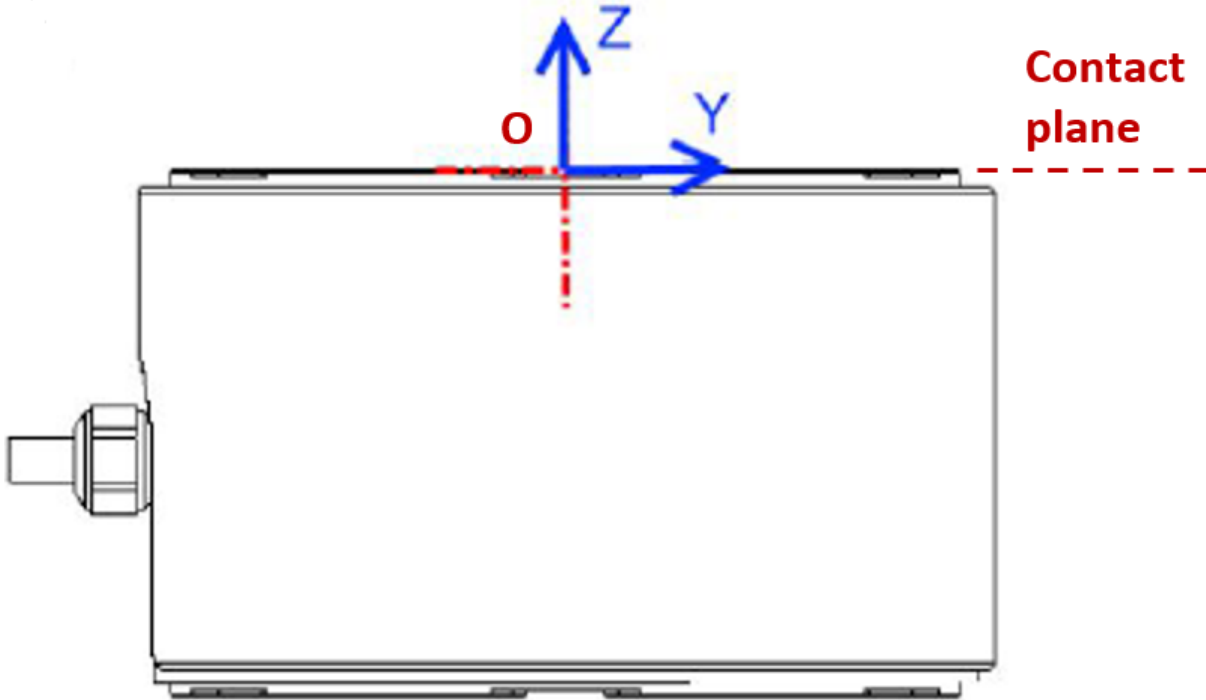
Figure 3.2: 6ADF80 coordinate axes and origin

Therefore, a measurement system based on the strain gauge load cell was designed and then tested for its frequency response. The next section illustrates the engineering journey involved.

3.2. Testing the dynamic characteristics of a 6ADF80 load cell-based system

To test for the measurement system frequency response, **the system is forced in multiple directions with an electrodynamic shaker (more details on this later). The idea is shown in Figure 3.3**. The shaker force F_{ref} [2] is decomposed at the stinger attachment point "A" along three mutually orthogonal axes, let's call them "shaker axes" (in red), parallel to the load cell axes (green). The components so obtained are denoted by F'_x, F'_y and F'_z. The reference force and moment components in load cell axes are denoted with $F^c_x, F^c_y, F^c_z, M^c_x, M^c_y$ and M^c_z, and are obtained by resolving F'_x, F'_y and F'_z at the load

---

[2]Notice that in Figure 3.3 F_{ref} is positive if compressive, i.e. if the piezoeletric load cell attached to the shaker stinger (see section 3.2.2) is compressed. This is also the convention for the measurement signal of all the uniaxial piezoeletric load cells used in this thesis work
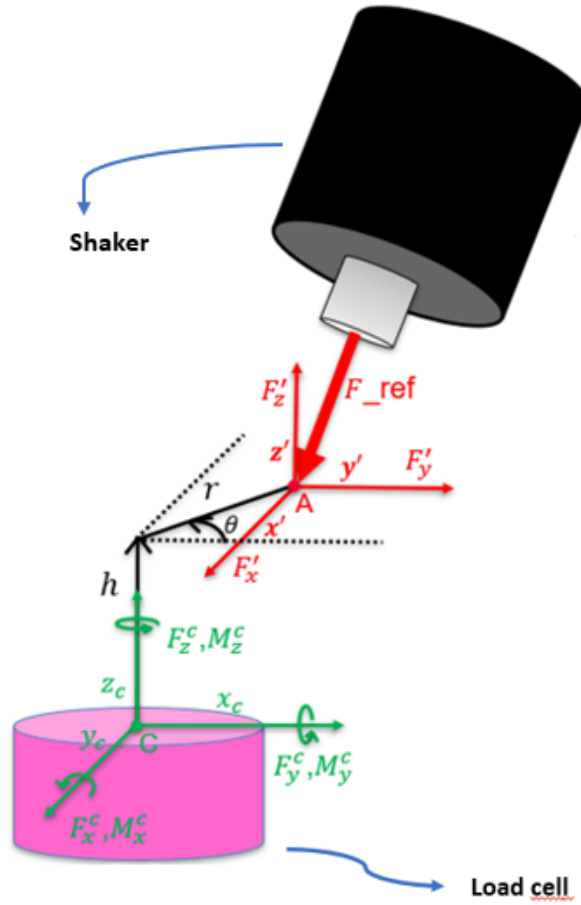
Figure 3.3: Measurement system test setup

cell coordinate origin "C" along its three mutually orthogonal axes. **From geometry the following relationships can be derived** :

$$
\begin{aligned}
M_x^c &= F_z' r \cos\theta - F_y' h \\
M_y^c &= F_x' h + F_z' r \sin\theta \\
M_z^c &= -F_x' r \cos\theta - F_y' r \sin\theta \\
F_x^c &= F_x' \\
F_y^c &= F_y' \\
F_z^c &= F_z'
\end{aligned}
\tag{3.1}
$$

Let $\mathbf{FM_c} := [F_x^c, F_y^c, F_y^c, M_x^c, M_y^c, M_z^c]^T$ and $\mathbf{FM_{sh}} := [F_x', F_y', F_y']^T$ be the column vectors of reference forces/moments in the load cell and shaker axes, respectively.

3.2.1.   First challenge, interfacing 6ADF80 load cell to both LTUs

The first challenge was to design a **mechanical interface** between the load cell and the LTUs **under the following design constraints** :

- **The interface's first mode frequency must be sufficiently higher than that of the load cell**

- **It has to be as lightweight as possible**

- **It has to be as compact as possible**

- **Multiple attachment points for the shaker stinger must be present**

The second design objective is driven principally by the fact that by increasing the interface mass (while keeping its geometry fixed) one lowers the whole measurement system's first mode frequency. The third objective is driven both by the same consideration as the second one and by an aerodynamic consideration. In fact, a large interface is likely to substantially disturb the LTU flow field.

The best trade-off between performance and simplicity of production was found in the solution shown in pictures 3.4 and 4.1. The LTU is connected to the the **"LTU plate"** by means of four socket head cap screws. The load cell on the other hand is first connected to the **"Load cell base plate"** (which in turn is attached to the very rigid support shown in Figure 3.5a) by means of four screws and one dowell pin, and then to the **"Load cell upper plate"** by means of four screws residing in counterbored holes and one dowel pin. The two subsystem so obtained are finally connected together by means of eight bolts passing through slots on the "LTU plate" and holes on the "Load cell upper plate". The detailed mechanical drawings of "LTU plate", "Load cell upper plate" and "Load cell base plate" are reported in appendix A. The attachment to the shaker stinger is by means of simple rectangular shaped parts, an example of which is shown in Figure 3.5a
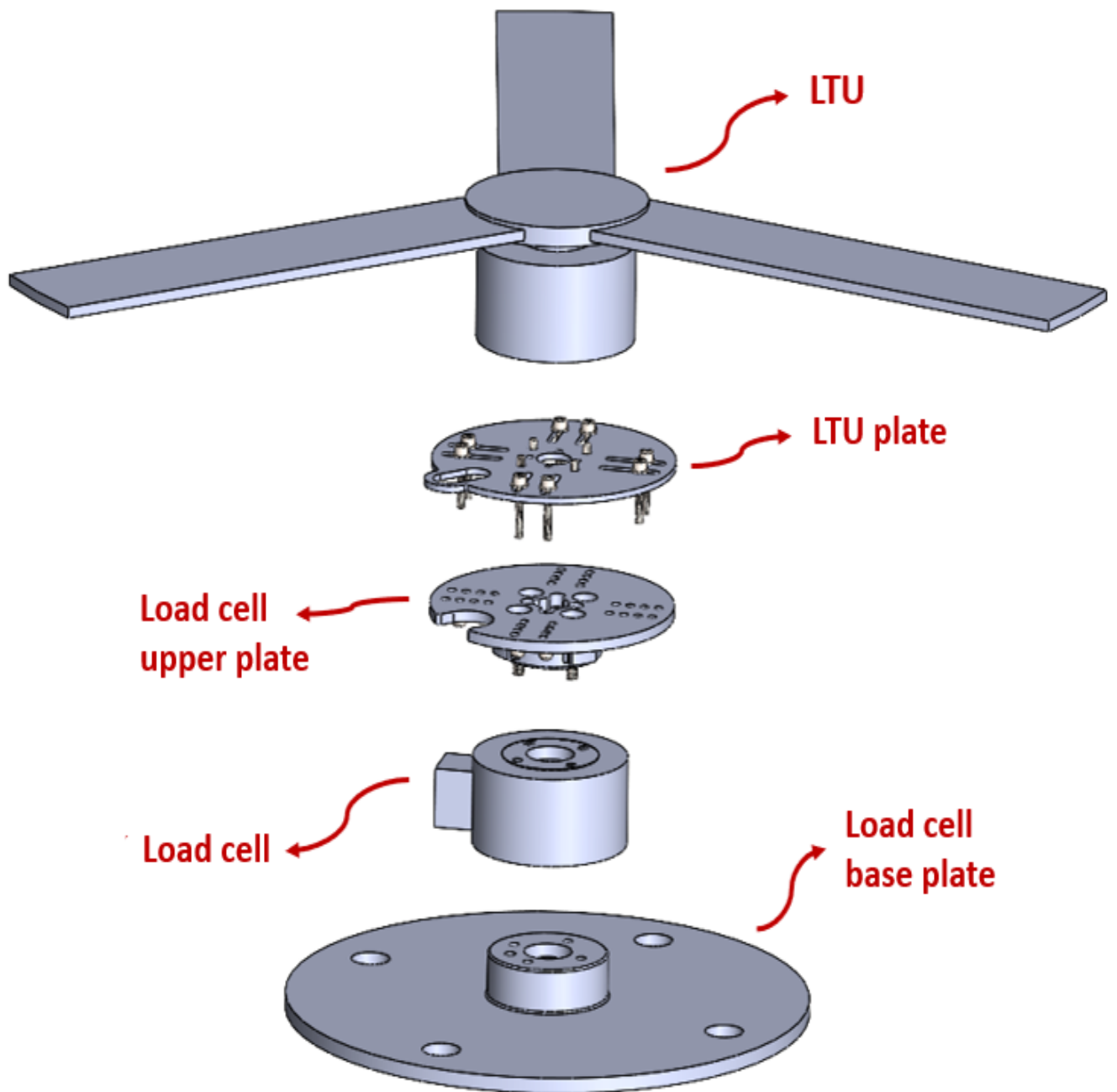
Figure 3.4: LTU to 6ADF80 Load cell mechanical interface

3.2.2.   Second challenge, devising a shaker test setup

As a first test it was decided to excite the system comprising the load cell and the "load cell upper plate" (see previous section) in the vertical direction and with an eccentricity with respect to the load cell coordinate origin (see Figures 3.5a and 3.2). So, particularizing equation 3.1 to the case of Figures 3.5a and 3.5b, yields :

$$
\begin{aligned}
M_x^c &= 0 \\
M_y^c &= r F_{ref} \\
M_z^c &= 0 \\
F_x^c &= 0 \\
F_y^c &= 0 \\
F_z^c &= -F_{ref}
\end{aligned}
\tag{3.2}
$$

since :

$$r = 0.012 \ m \tag{3.3}$$

$$h = 0 \ m \tag{3.4}$$

$$\theta = 270° \tag{3.5}$$

$$F_x' = 0 \tag{3.6}$$

$$F_y' = 0 \tag{3.7}$$

$$F_z' = -F_{ref} \tag{3.8}$$
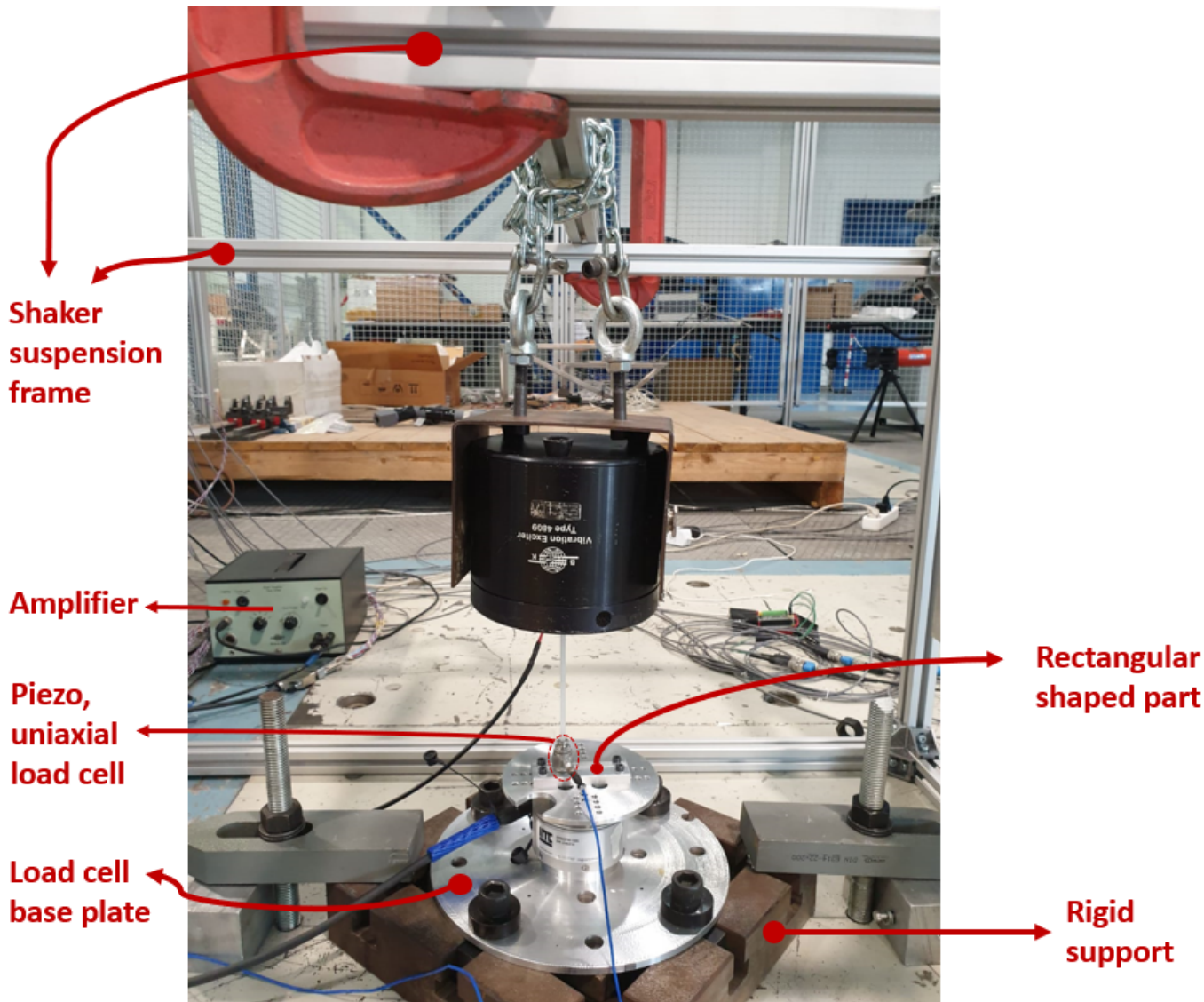
(a) Shaker test setup
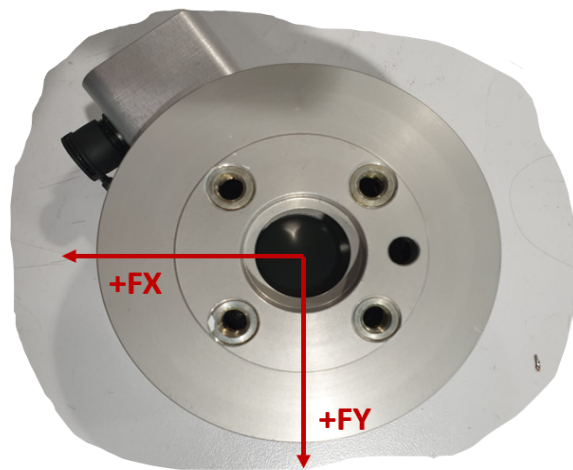
(b) Load cell top view in test setup

Figure 3.5: Shaker test in vertical direction

Due to the difficulty of connecting for this test the LTU and its LTU plate to the rest of the subsystem shown in Figure 3.5a, and considering the bigger LTU, their effect on the system frequency response was taken into account by attaching a mass (not shown in Figure 3.5a) of 1121.25 g [3] and of the same height as that of the subsystem LTU + LTU plate to the center of the top surface of the "load cell upper plate".

Referring again to Figure 3.5a, the system was excited by an **electrodynamic shaker** which was suspended to a frame. To measure the force applied by the shaker during the test, an **uniaxial piezoelectric load cell was placed in series with the shaker stinger**, and the whole system stinger+load cell threaded into the forcing point on the the rectangular shaped part. The shaker input **open-loop control signal** was generated by the **SCADAS data acquisition system** (see Figure 3.6) and then fed to an **amplifier** connected in series and before the shaker. Referring to Figure 3.6, the six channels of the load cell were connected to six of the eight channels of the VB8III-RT acquisition card by means of a cable with SUBHD 44 female to six 7-pin LEMO male connectors, while the piezoelectric load cell was connected to the V24-II card by means of a coaxial cable with 10-32 to BNC male connector.

---

[3]The mass of the bigger LTU is 755 g, being 555 g the mass of the bigger motor, and 155 g that of the bigger propeller (see 1). The masses of "LTU plate" and "Load cell upper plate" are given in Appendix A, and are 90 g and 250 g, respectively. So, taking into account also the total mass of screws, nuts and bolts, which is 50 g, we get a total mass of 1100 g, which is indeed roughly equal to the equivalent mass.
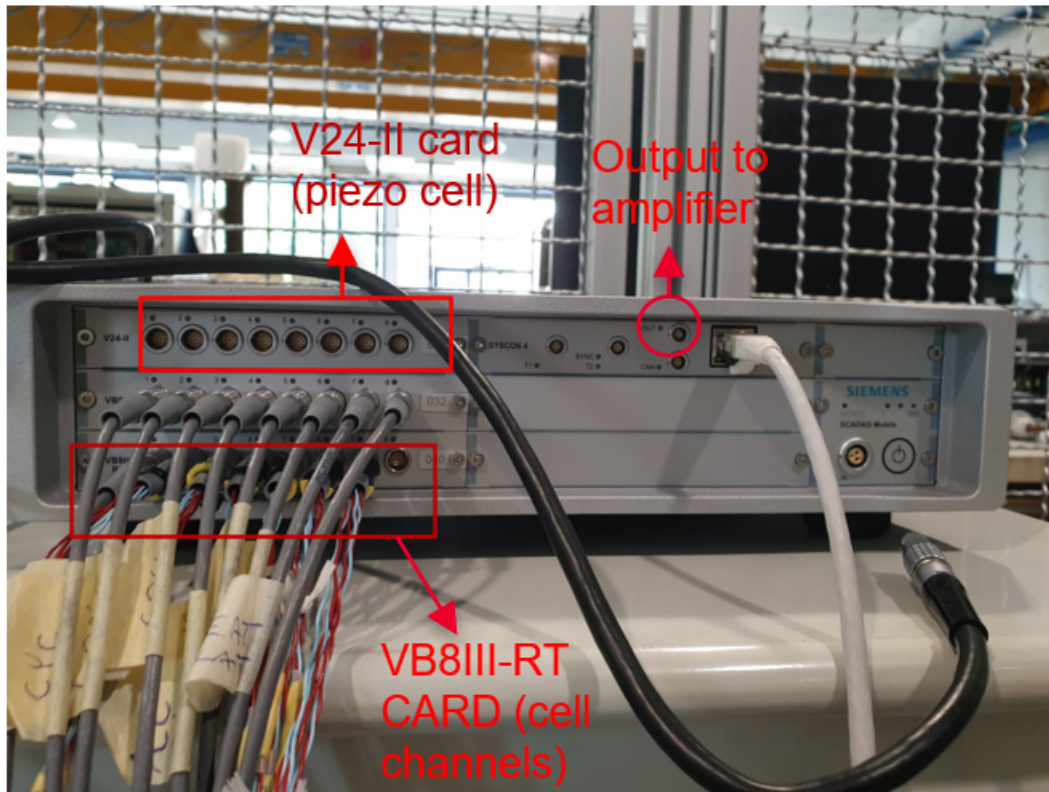
Figure 3.6: SCADAS data acquisition system

3.2.3.   Stepped sine test and post-processing

To derive the FRFs between the reference and the measured force/moment components, a **"Stepped Sine Test"** was performed. In this test, the frequency of the shaker excitation force is increased (up cycle test) or decreased (down cycle test) at a **given frequency step** (see reference [23]). The SCADAS generates a sinusoidal waveform at a given frequency, and after a certain **settling time** is elapsed, it then calculates the FRF between the shaker **reference force** F_{ref} (see Figure 3.3) and each channel **non-dimensional voltage signal**, which is the channel output voltage divided by the excitation voltage of the load cell bridge circuits [4]. Let's denote by $\mathbf{FRF_{CH}}$ and $\mathbf{MC}$ the column vector of the channels FRFs and the 6x6 load cell static calibration matrix, respectively. Then, if each component of vector $\mathbf{FM_c}$ is different from zero, it is useful to define the following diagonal matrix, constructed from the reciprocals of the components of vector $\mathbf{FM_c}$ multiplied by F_{ref} :

---

[4]The six channels signals are acquired in parallel with the reference force F_{ref} signal

$$\mathbf{D} := F_{ref} \begin{bmatrix} \frac{1}{F'_x} & 0 & 0 & 0 & 0 & 0 \\ 0 & \frac{1}{F'_y} & 0 & 0 & 0 & 0 \\ 0 & 0 & \frac{1}{F'_z} & 0 & 0 & 0 \\ 0 & 0 & 0 & \frac{1}{F'_z r \cos\theta - F'_y h} & 0 & 0 \\ 0 & 0 & 0 & 0 & \frac{1}{F'_x h + F'_z r \sin\theta} & 0 \\ 0 & 0 & 0 & 0 & 0 & \frac{1}{-F'_x r \cos\theta - F'_y r \sin\theta} \end{bmatrix} \tag{3.9}$$

In fact, the column vector of the force/moment components FRFs, $\mathbf{FM_{frf}}$, can be computed as follows :

$$\mathbf{FM_{frf}} = \mathbf{D} \cdot \mathbf{MC} \cdot \mathbf{FRF_{CH}} \tag{3.10}$$

If, on the other hand, one or more components of vector $\mathbf{FM_c}$ are equal to zero, then only the subset of equations 3.10 corresponding to the non-zero components of vector $\mathbf{FM_c}$ will be useful. In the case of a zero force component, the FRF between F_{ref} and itself is instead useful, while in the case of non zero moment component, it is useful to compute the FRF between $b \cdot F_{ref}$, where b is an appropriate reference distance [5], and itself. In fact, in both cases the FRF magnitude should be approximately zero. The FRFs between the force/moment components were obtained in post-processing, as just described, from the channels FRFs computed by the SCADAS.

The relevant test parameters are the sampling frequency FS, the starting excitation frequency f_{in}, the highest excitation frequency f_{fin} and the excitation frequency step Δf. For this test their values are :

- $FS = 1600$ Hz

- $f_{in} = 2$ Hz

- $f_{fin} = 500$ Hz

- $\Delta f = 0.5$ Hz

---

[5]It could be e.g. the distance of the point of application of F_{ref} from the load cell coordinate origin

To assess the FRF data computed by the SCADAS, the FRFs of the channels were also computed in Matlab starting from the time histories of F_{ref} and those of the six channels non-dimensional voltages (raw data) as follows :

- The time histories of the six channels non-dimensional voltages and that of F_{ref} are divided into N_{tb} equal time blocks of data (typically from 25 to 30)

- An FFT (Fast Fourier Transform) is performed for each time block separately [6]. Let's denote with $G_R^{jn}(\omega)$ and $G_I^{jn}(\omega)$ the FFT real and imaginary part, respectively, of the nth block of channel j, and with $G_R^{rn}(\omega)$ and $G_I^{rn}(\omega)$ the FFT real and imaginary part of the nth block of F_{ref}

- From the channels FFTs, the corresponding autopower spectrum is computed for each channel and for each time block. The autopower spectrum of the nth block of channel j is given by :

$$S_{jj}^n(\omega) := (G_R^{jn}(\omega) + iG_I^{jn}(\omega))(G_R^{jn}(\omega) - iG_I^{jn}(\omega)) \tag{3.11}$$

- From the channels and F_{ref} FFTs, the cross power spectrum is computed between F_{ref} and each channel, for each time block. The cross power spectrum of the nth block of channel j and the nth block of F_{ref} is given by :

$$S_{jr}^n(\omega) := (G_R^{jn}(\omega) + iG_I^{jn}(\omega))(G_R^{rn}(\omega) - iG_I^{rn}(\omega)) \tag{3.12}$$

- The average of all N_{tb} autopower spectra is computed for each channel j. Denoting this average with $\overline{S_{jj}}(\omega)$ (notice the overline), one has :

$$\overline{S_{jj}}(\omega) = \frac{\sum_{n=1}^{N_{tb}} S_{jj}^n(\omega)}{N_{tb}} \tag{3.13}$$

- The average of all N_{tb} cross power spectra between channel j and F_{ref} is computed for each channel j. Denoting this average with $\overline{S_{jr}}(\omega)$, one has :

$$\overline{S_{jr}}(\omega) = \frac{\sum_{n=1}^{N_{tb}} S_{jr}^n(\omega)}{N_{tb}} \tag{3.14}$$

---

[6]A window function can be applied (in this particular case, a Hamming window was used) to each time block
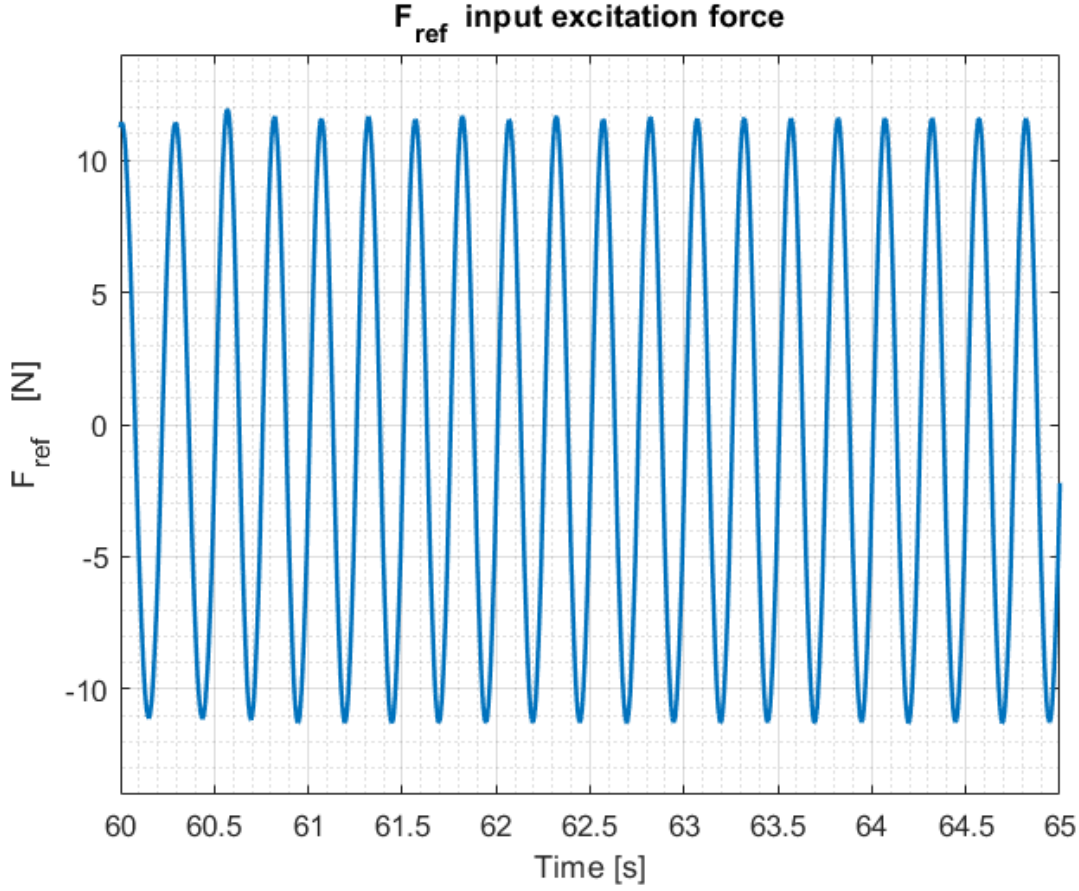
Figure 3.7: Excitation force time history

- The FRF between channel j and F_{ref} is computed as (see section 3.5 of reference [2]) :

$$FRF_j = \frac{\overline{S_{jr}}(\omega)}{S_{jj}(\omega)} \tag{3.15}$$

  FRF_j are the components of vector $\mathbf{FRF_{CH}}$ in equation 3.10

- Vector $\mathbf{FM_{frf}}$ is computed by using equation 3.10

3.2.4.   Shaker test results

First of all to assess the quality and the magnitude of the excitation force from the shaker, i.e. F_{ref}, a representative portion of its time history is reported in Figure 3.7 :

The FRFs between F_{ref} and the six channels non-dimensional voltages are reported in Figure 3.8, in which the FRFs computed by the SCADAS are compared to those obtained by the method described in section 3.2.3
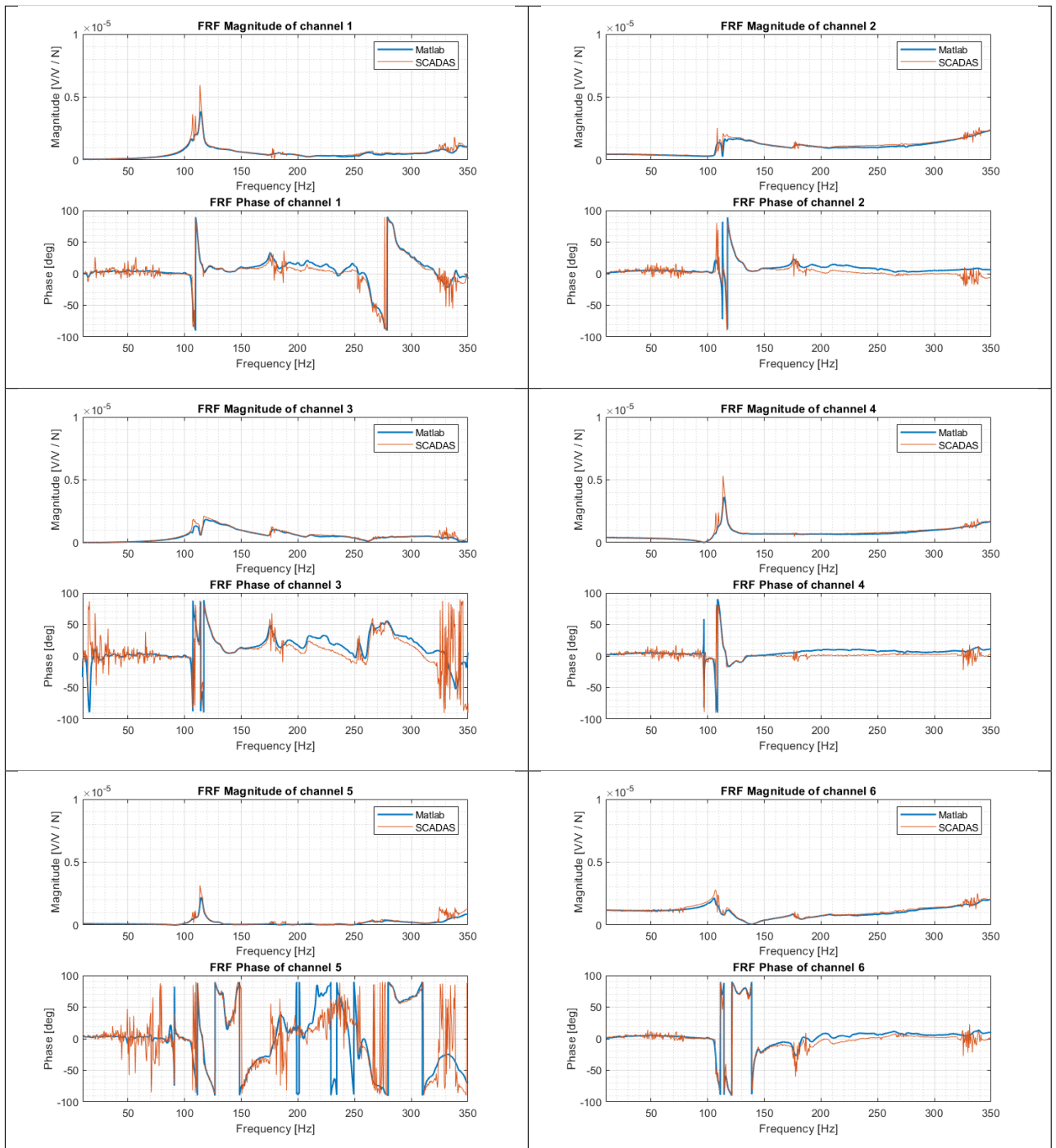
Figure 3.8: FRFs of the channels
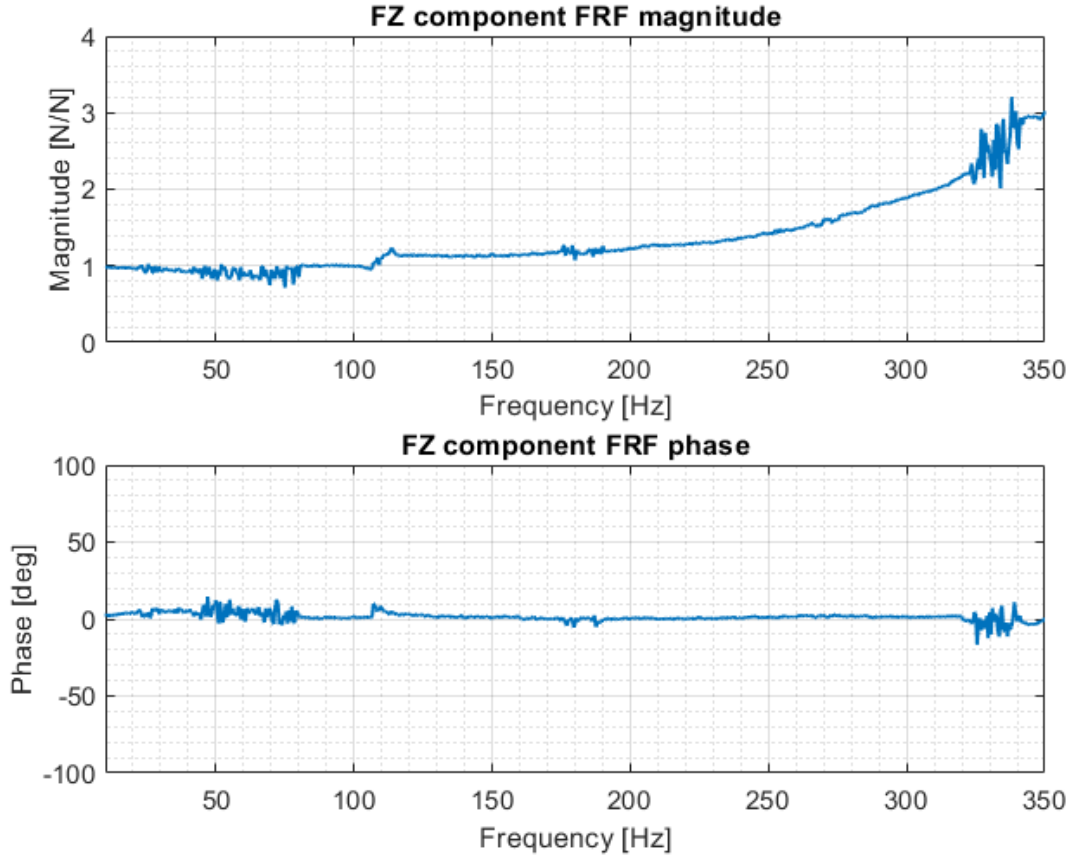
Figure 3.9: FRF of F_Z force component

Then, the FRFs of F_Z and M_Y, which are the only non-zero reference force/moment components, are reported in Figures 3.9 and 3.10, respectively. Finally the FRF between F_{ref} and M_Z [7], which is a zero reference moment component, is reported in Figure 3.11 as an example to show that its equivalent arm is indeed negligible.

3.2.5. Analysis of results and conclusion

From the FRFs of the channel, it is clear that the measurement system has a structural resonance at around 110 Hz. Although this resonance does not clearly manifests itself in the FRF of F_Z (Figure 3.9), it is clearly visible in the FRF of M_Y (Figure 3.10). Because of the frequency separation between the structural modes of the mechanical interface and those of the load cell [8], it can be concluded that the 110 Hz peak is due to the load cell first

---

[7]Not to be confused with the FRF between its reference and its measured value
[8]A resonance attributable to the "Load cell base plate" was found at a higher frequency of roughly 350 Hz)
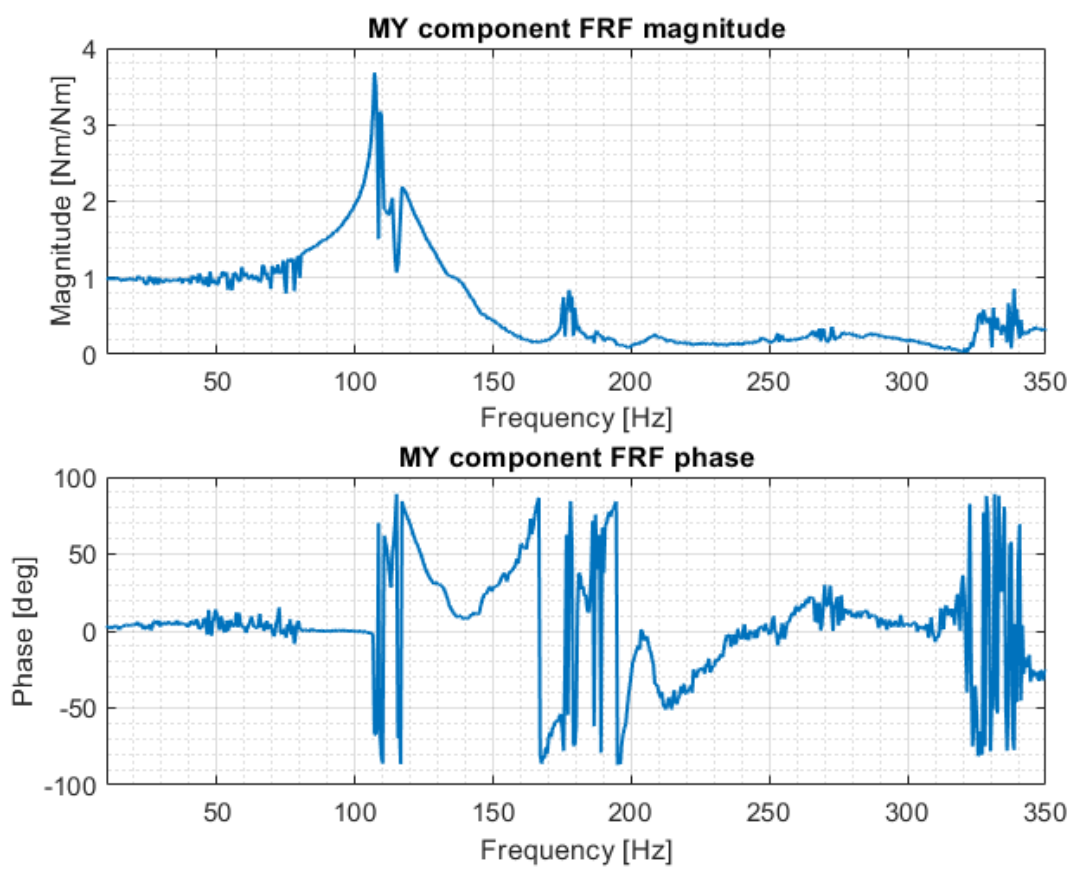
Figure 3.10: FRF of M_Y moment component
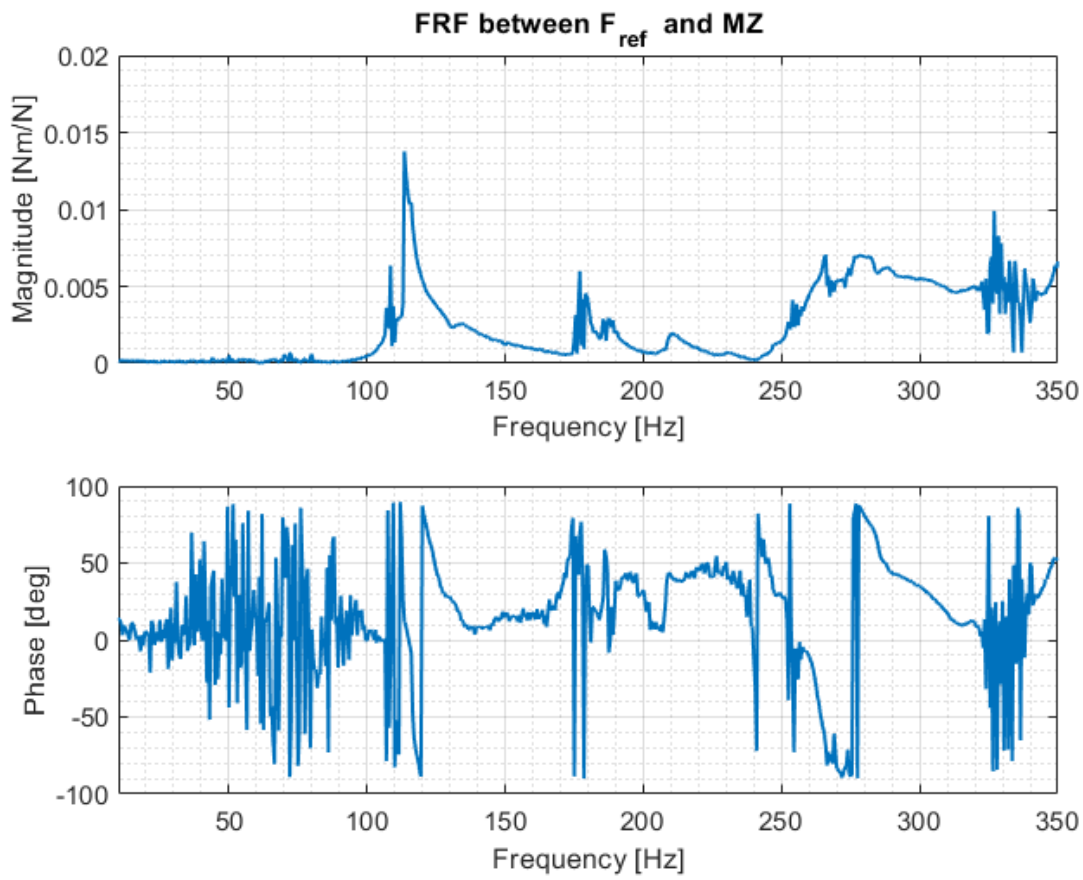
Figure 3.11: FRF between F_{ref} and M_Z moment component

structural mode, which means that **the load cell frequency response is not suitable for the application, for which a bandwidth of at least 250 Hz is required, as stated above**.

3.3. Designing and testing a piezoelectric system

In view of the results of the tests on the 6ADF80-based measurement system, **in all the subsequent work only the bigger LTU was considered. In fact a measurement system capable of measuring the 3/rev dynamic loads of the smaller LTU, comprising the smaller BPMS motor and the smaller propeller (see 1), would require a bandwidth of 500 Hz (the smaller LTU has a maximum angular speed of 10000 RPM). Such requirement was deemed to be too demanding for a low cost design** [9]. **So, a new measurement system was designed based on three PCB208C03 uniaxial piezoelectric load cells, which were already available without purchase**. Clearly the rationale for the choice of these sensors is their comparatively high frequency limit, which is of the order of the tens of a KHz. A mechanical interface consisting of two parts called **"Piezo upper plate" and "Piezo lower plate"**, and shown in Figure 3.12 (the relative mechanical drawings are in Appendix A), was devised and produced :

The measurement system axes and origin are defined in Figure 3.13. The measurement range of a single uniaxial load cell is 2.224 kN, which means that the measurement range for the F_Z force component is $3 * 2.224 = 6.672$ kN for the whole measurement system.

---

[9]Even if the smaller LTU has a mass which is roughly one third of that of the bigger one and a height which is roughly 30% less
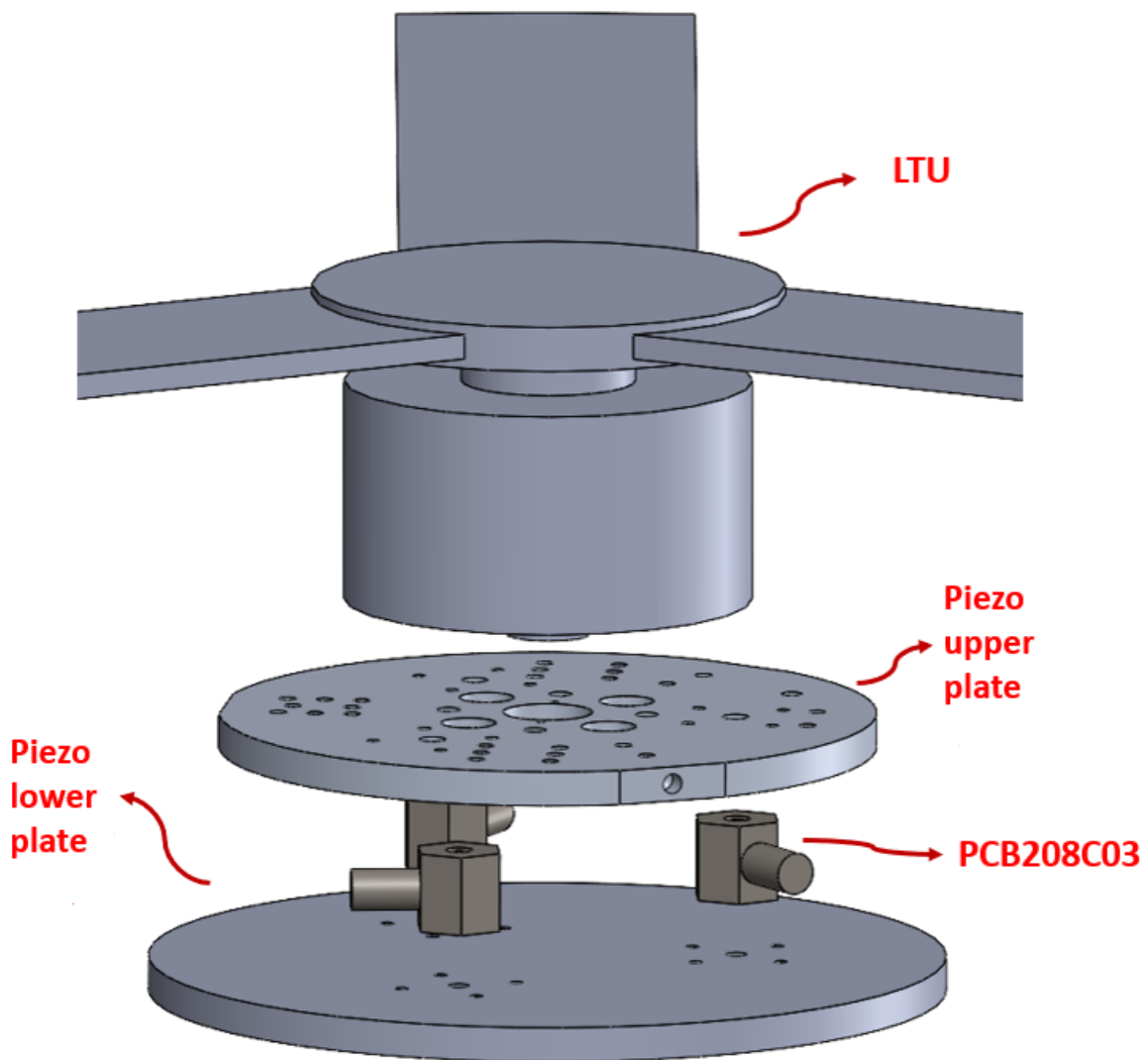
Figure 3.12: Piezoelectric measurement setup
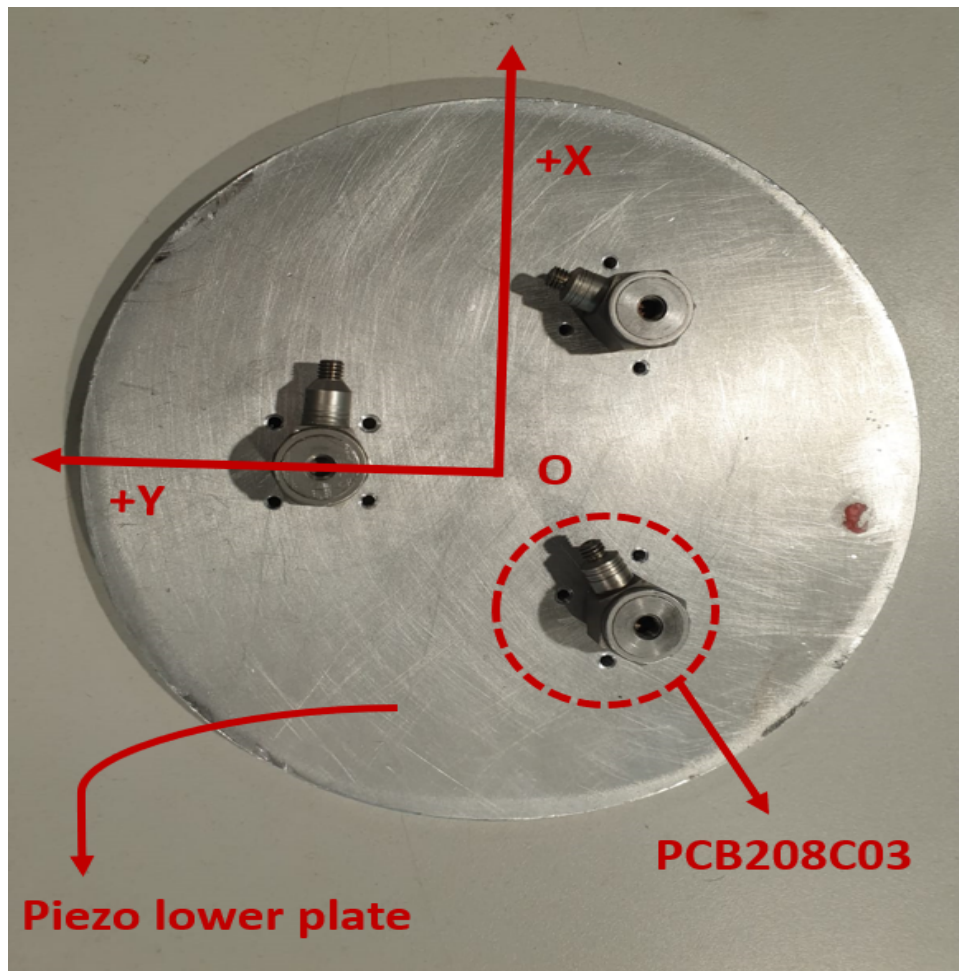
(a)
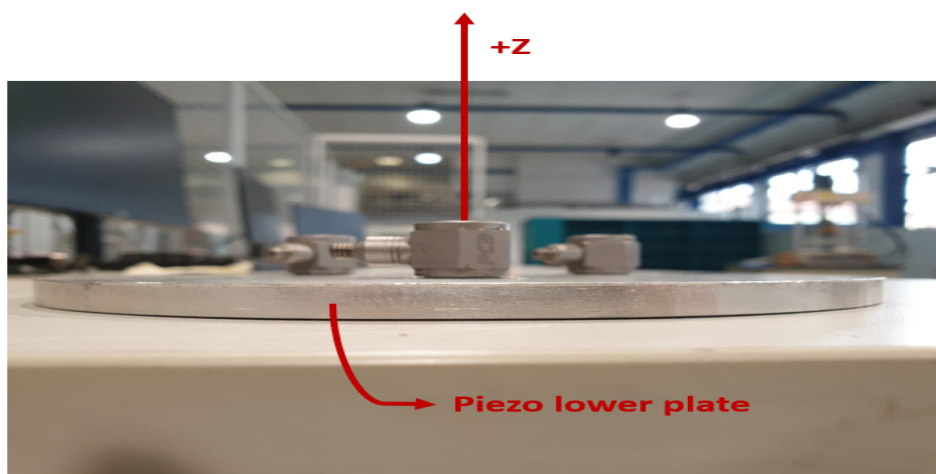
(b)

Figure 3.13: Piezoelectric measurement system, axes definition

The intrinsic limitation of this setup is that it is only capable to measure one force component, namely F_Z and two moment components, namely M_X and M_Y. Some concepts to overcome this limitation will be presented in section 3.3.4. But first of all the test to prove the suitability of the frequency response of the system will be presented.

3.3.1.   Shaker test

A shaker test was performed in the vertical direction and with an eccentricity of $d_1 = 49.57$ mm along the system X-axis (see Figures 3.14 and 3.15). The shaker test setup was totally analogous to the one described in section 3.2.2, with the exception that the actual motor was mounted [10] instead of an equivalent mass (see Figure 3.15 [11]). In Figure 3.14, the bigger and smaller circles define the area occupied by the motor and the piezoelectric cell measuring F_{ref}, respectively, while F_1, F_2 and F_3 are the three vertical reaction forces of the three uniaxial load cells, which are taken as positive if in the upward direction (load cell in compression). By adopting this convention, F_1, F_2 and F_3 are exactly the forces measured by the corresponding load cells.

Particularizing equation 3.1 to the case of Figures 3.14 and 3.15, yields :

$$
\begin{aligned}
M_x^c &= 0 \\
M_y^c &= r F_{ref} \\
M_z^c &= 0 \\
F_x^c &= 0 \\
F_y^c &= 0 \\
F_z^c &= -F_{ref}
\end{aligned}
\tag{3.16}
$$

since :

---

[10] The test was performed with the motor blocked and without propeller

[11] Although the propeller is shown in this Figure, the test was actually performed without the mounted propeller
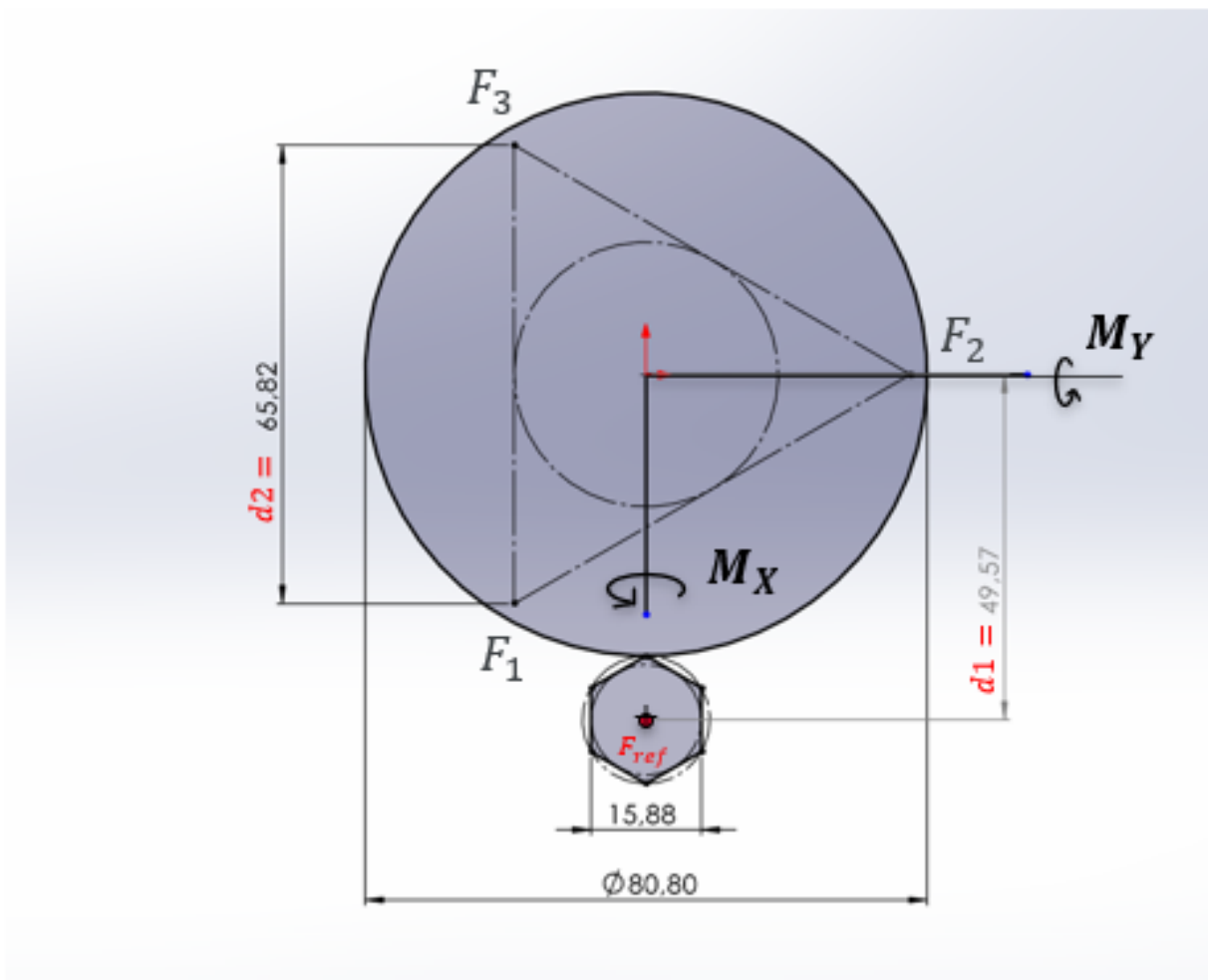
Figure 3.14: Shaker test geometry
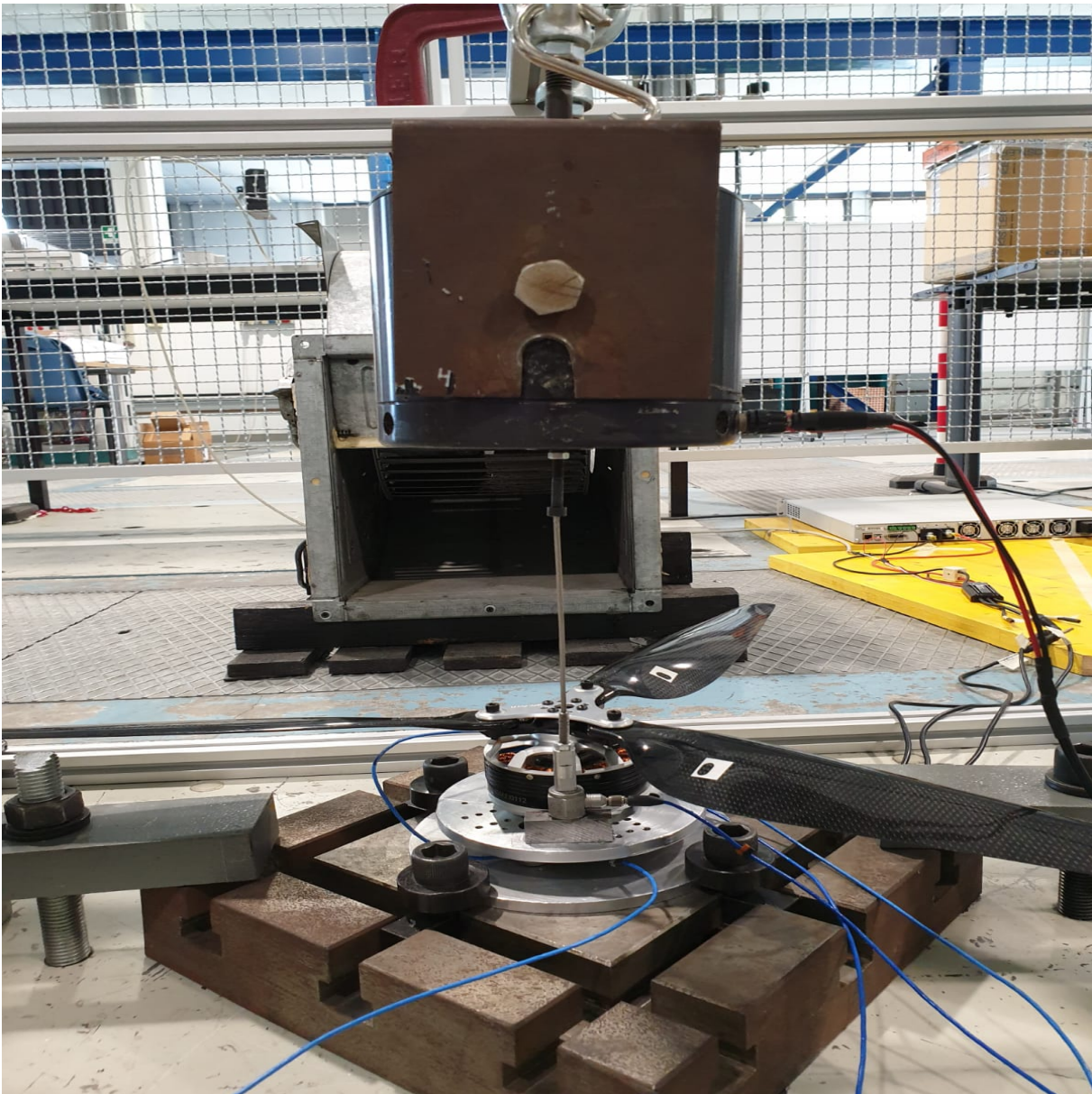
Figure 3.15: Shaker test setup

$$r = 0.04957 \ m \tag{3.17}$$
$$h = 0 \ m \tag{3.18}$$
$$\theta = 270° \tag{3.19}$$
$$F'_x = 0 \tag{3.20}$$
$$F'_y = 0 \tag{3.21}$$
$$F'_z = -F_{ref} \tag{3.22}$$

Further, referring to Figure 3.14, one obtains the following equilibrium equations :

$$
\begin{aligned}
M_X &= d_2 \frac{(2F_2 - F_1 - F_3)}{2\sqrt{3}} = 0 \\
M_Y &= d_1 F_{ref} + d_2 \frac{(F_3 - F_1)}{2} = 0 \\
F_Z &= F_1 + F_2 + F_2 - F_{ref} = 0
\end{aligned}
\tag{3.23}
$$

from which the theoretical values of the ratios $\frac{F_1}{F_{ref}}, \frac{F_2}{F_{ref}}$ and $\frac{F_3}{F_{ref}}$ can be obtained as :

$$
\begin{aligned}
\frac{F_1}{F_{ref}} &= \frac{3d_1 + d_2}{3d_2} = 1.08645 \\
\frac{F_2}{F_{ref}} &= \frac{1}{3} \\
\frac{F_3}{F_{ref}} &= \frac{d_2 - 3d_1}{3d_2} = -0.41978
\end{aligned}
\tag{3.24}
$$

The values of the relevant parameters were :

- $FS = 3200$ Hz

- $f_{in} = 2$ Hz

- $f_{fin} = 1000$ Hz

- $\Delta f = 0.5$ Hz
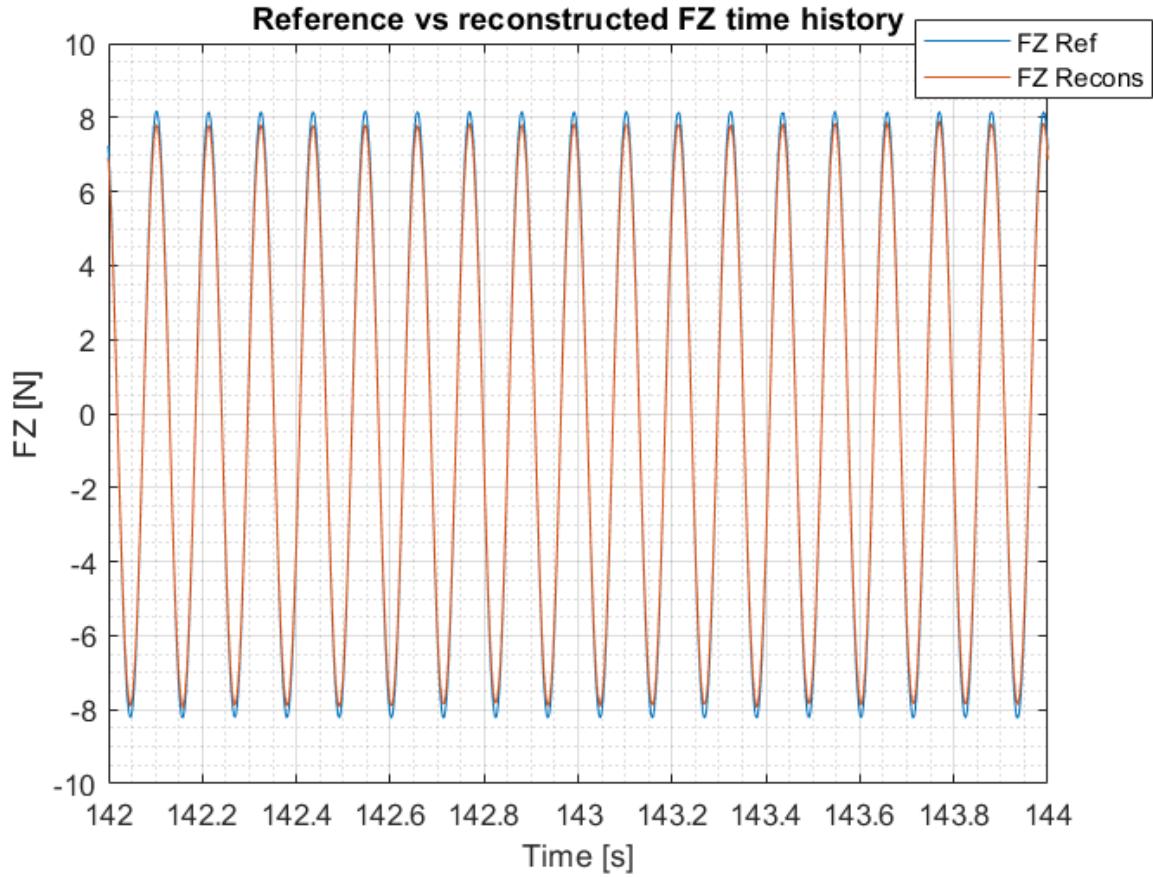
Figure 3.16: Excitation vs reconstructed F_Z

3.3.2. Shaker test results

First of all, to assess the quality and the magnitude of the excitation force from the shaker, a representative time portion of the reference value of F_Z, i.e. F_z^c in equation 3.16, is reported in Figure 3.16. The reconstructed F_Z, given by $-(F_1 + F_2 + F_3)$ is also reported in the same Figure for comparison. The FRFs between F_1, F_2 and F_3 and their corresponding reference values computed from equation 3.24 is reported in Figure 3.17. It can be noticed that the magnitude of channels 1 and 2 FRFs is pretty far from the ideal value of 1. This fact will be further discussed later. Finally the FRFs of F_Z and M_Y are reported in Figures 3.18 and 3.19, respectively, while it was checked that the FRF between F_{ref} and the M_X moment component was negligible.
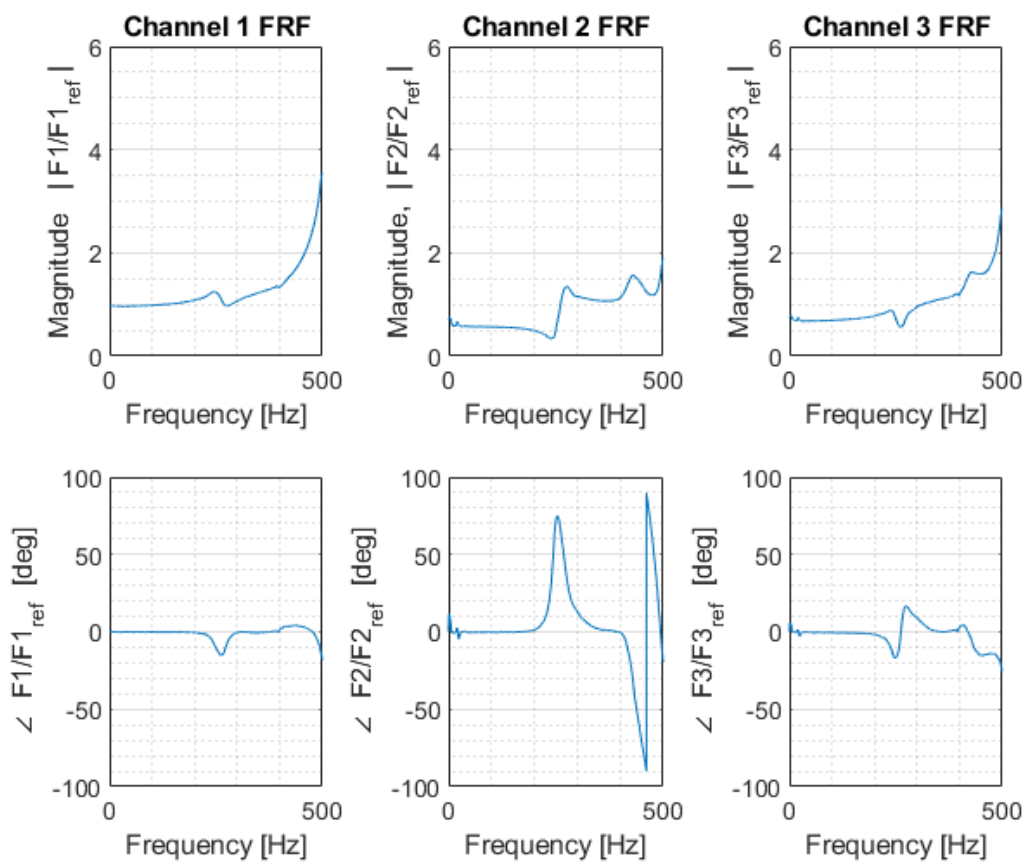
Figure 3.17: FRFs of the channels
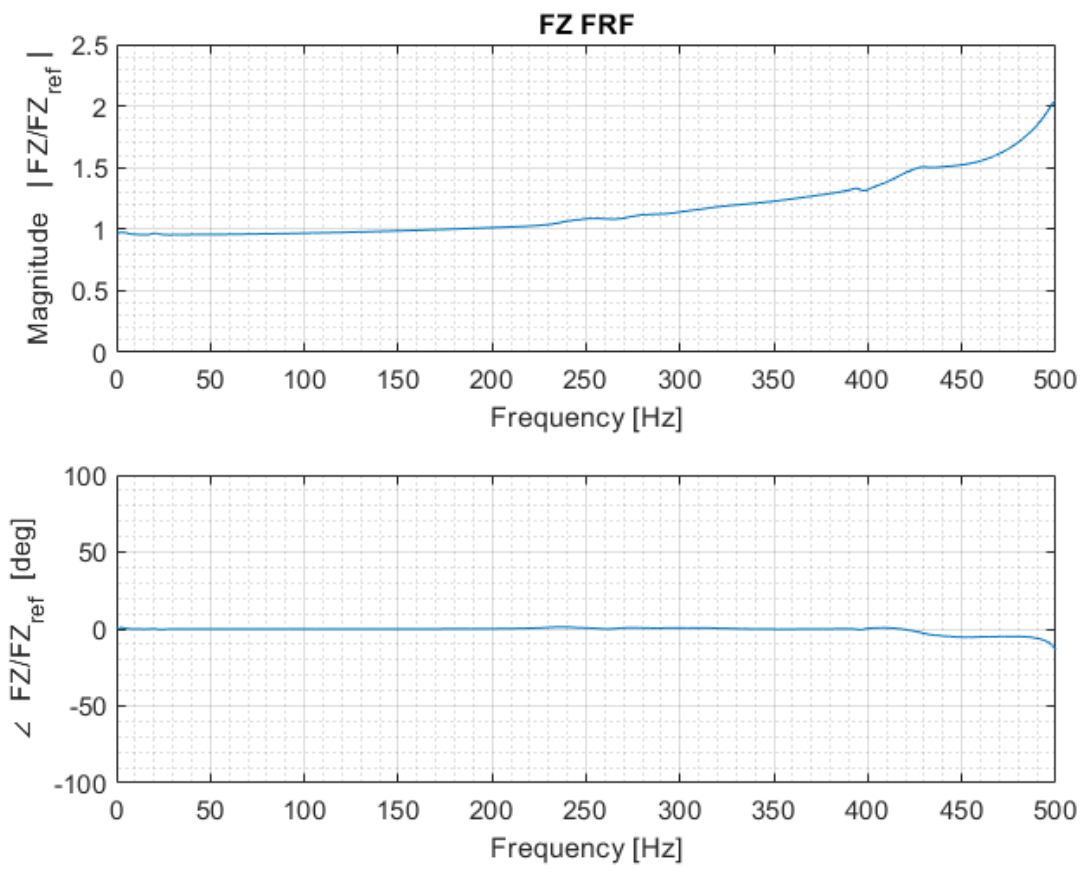
Figure 3.18: FRF of F_Z
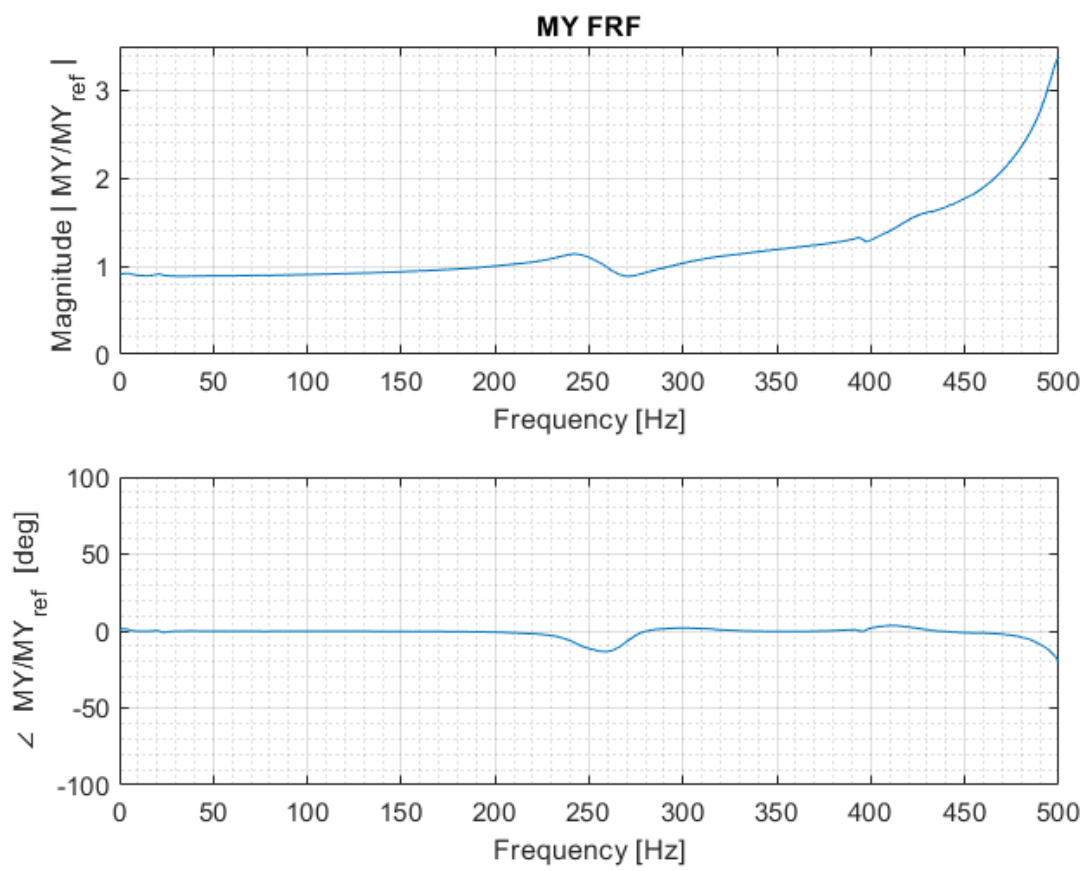
Figure 3.19: FRF of M_Y

3.3.3.   Analysis of shaker test results

Figure 3.17 shows that the magnitude of channels 1 and 2 FRFs is pretty far from the ideal value of 1, even at low frequencies (quasi-static range). This means that M_X and M_Y cannot be reconstructed solely from F_1, F_2, F_2 and the geometry, i.e. by using and first and the second of equations 3.23. This is likely due to the existence of non negligible local moments at the interface between the "Piezo upper plate" and the three uniaxial load cells (see Figure 3.12). This problem may be solved by a static calibration employing a set of 3 independent load conditions. By looking both at Figure 3.17 and 3.19, one can notice a rapid change in phase and amplitude taking place at roughly 200 Hz and other more prominent dynamics from 450 to 600 Hz. **Since the dynamic response taking place at 200Hz is in the range of interest, a further investigation was necessary to understand if it was possible to associate it to any particular part of the system (wheter it be the LTU, the upper plate, etc.). To this end a hammer test was performed (see Figures 3.20 and 3.21)**. As it is shown in Figure 3.20, three accelerometers measuring along the X, Y and Z axes, respectively, were placed on the motor hub, three accelerometers measuring along Z were placed on the upper plate, and one accelerometer measuring along Z was placed on the lower plate. Referring to Figure 3.21, the system was impacted along the Z direction at points 100, 200, and 300 on the lower plate, along Y at point 101 on the motor hub, and along X and Z, respectively, along points 201 and 301 (which actually are the same geometrical point) on the motor hub. **The result of this test was that the dynamic at 200 Hz is a highly damped (around 20% damping ratio) resonance associated with the motor, which is not part of the measurement system, being instead part of the LTU, i.e. of the subsystem whose dynamic characteristics are the measurement objective. On the other hand, the more prominent dynamics between 450 and 600 Hz are associated with the upper plate or with a combination of upper plate and motor. An example of a motor related mode shape is shown in Figure 3.22 (notice the very high damping ratio associated). The upper plate first mode shape, having a reasonable 2.5% damping ratio, is shown instead in Figure 3.23.**

3.3.4.   Conclusions and setup improvement

From the discussion in the previous two sections it can be concluded that **the proposed piezoelectric measurement has a frequency response which is suitable for the**
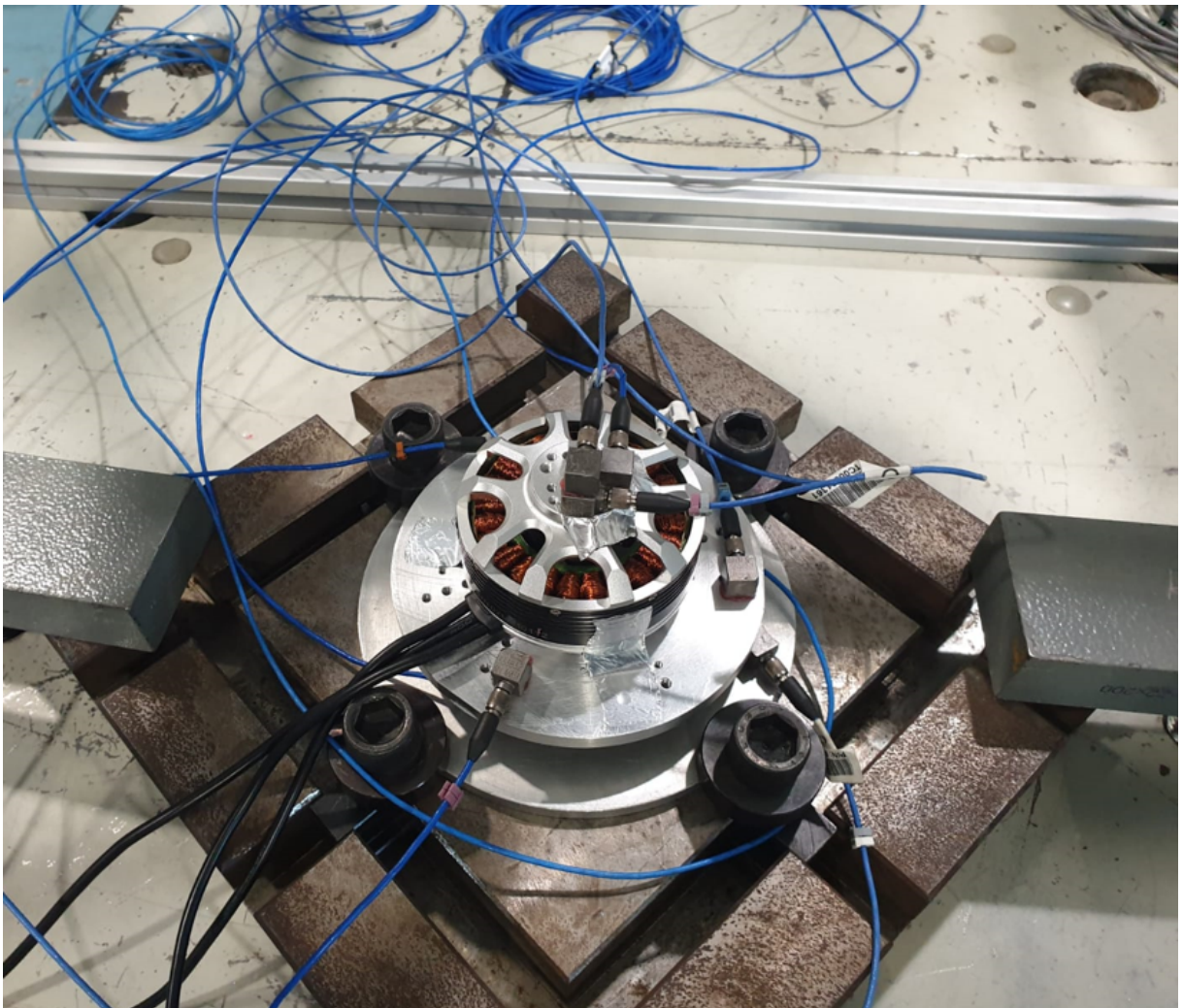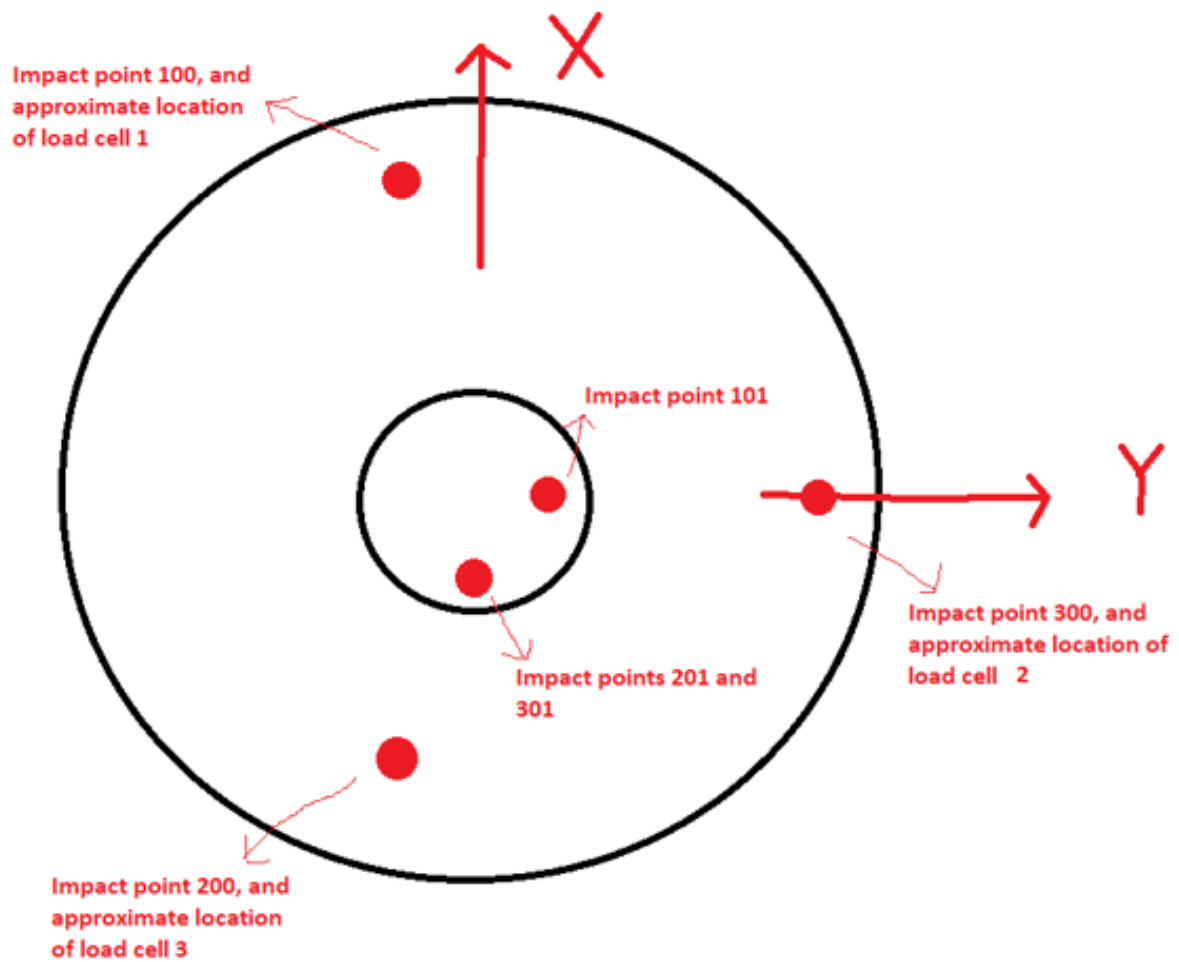
Figure 3.20: Hammer test setup
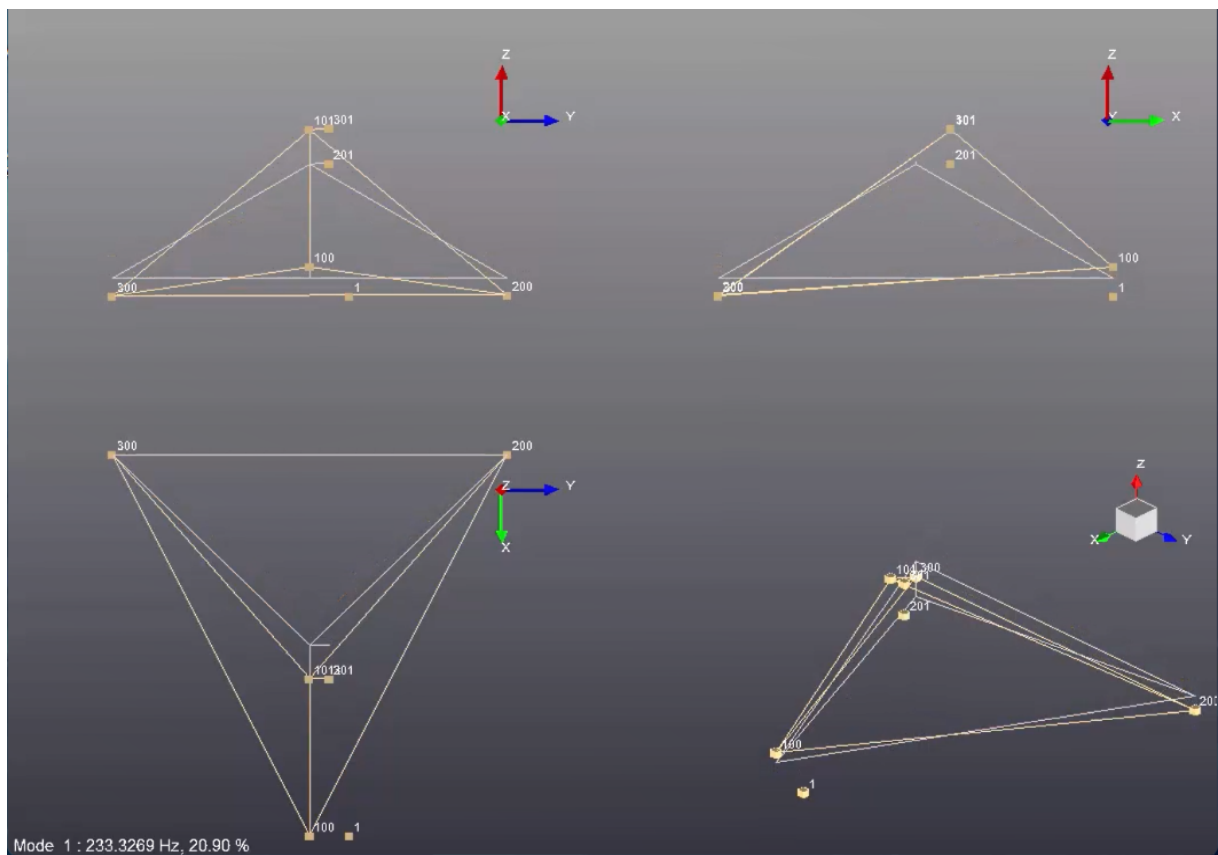
Figure 3.21: Hammer test geometry
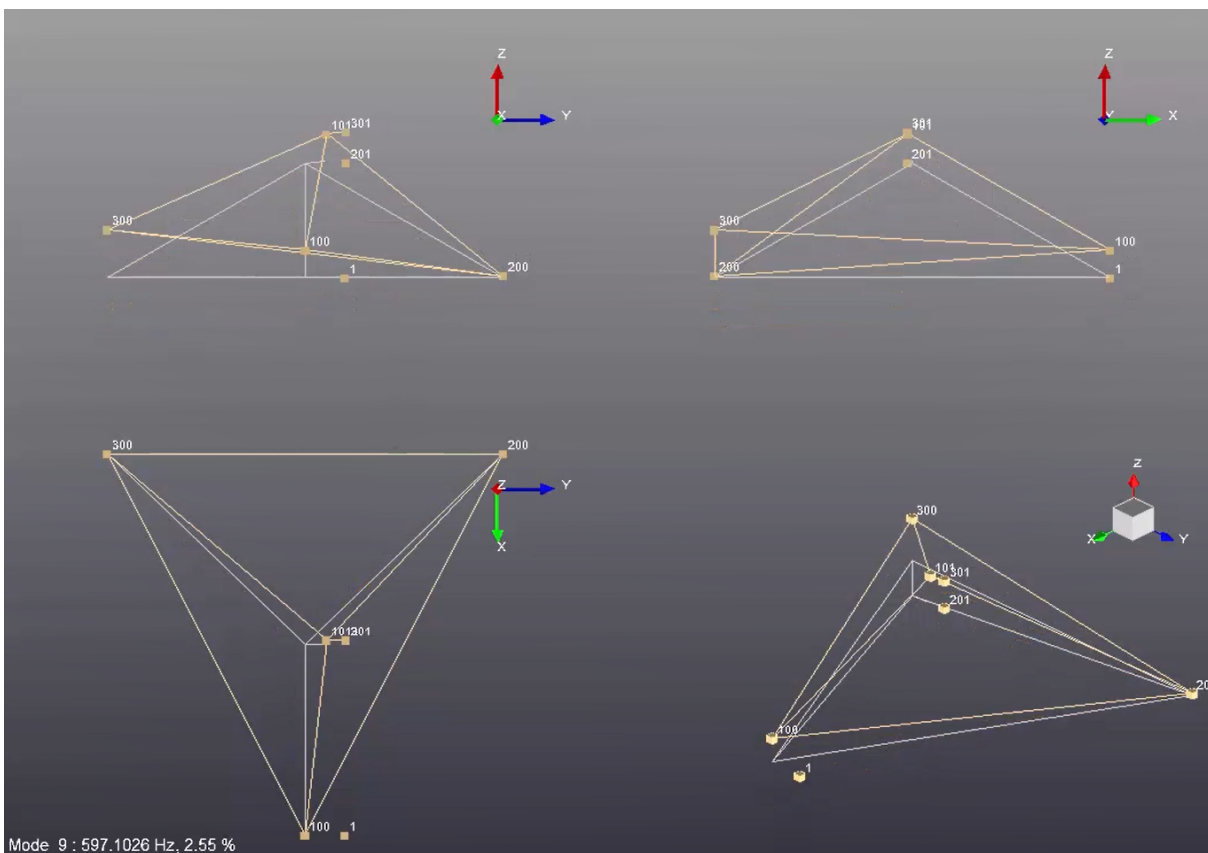
Figure 3.22: Motor related mode shape

Figure 3.23: Upper plate mode shape

application, but it could be improved by supporting the upper plate by means
of four symmetrically placed uniaxial load cells instead of three. In fact this
would have the effect of further increasing the frequency of the upper plate (or a combi-
nation of the upper plate and motor) dynamics. A static calibration is required, as
well as possibly a post-processing correction for the non-ideal behaviour of its
FRFs. Moreover, the intrinsic limitation of this setup of being only capable of
measuring F_Z, M_X and M_Y, could be overcome by substituting the three (or
four) uniaxial piezoelectric load cells with three (or four) triaxial piezoelectric
load cells, each one of them measuring force components along all three orthogonal axes.
The disadvantage of this latter setup is that it would require a complex calibration and
possibly a labor intensive preloading process.

3.4. 6A80C 6-axis strain gauge load cell-based system

At this point, the supplier of the first tested load cell made themselves avail-
able to lend a different 6-axis strain gauge cell, in order to test its dynamic
characteristics. In fact, the frequency response and the dynamic calibration
matrix of the sensor were not provided by the supplier, as it is typically used
in quasi-static tests. The rationale behind this proposal was that an in-house FEM
(Finite element method) model of the load cell with a rigid body element of 1000 g and 75
mm height (modelling the system attached to the top of the load cell), yielded a frequency
for its first structural mode of roughly 800 Hz. Characteristics of interest of the 6A80
type C load cell are :

- Overall diameter of 80mm and a height of 50 mm

- Mass of 1000 g

- Static measurement range of 5 kN for the F_X and F_Y force components, 15 kN for
  the F_Z force component and 250 Nm for all the three moment components

Another important point to be proven was whether it was possible or not to
measure forces and moments of two order of magnitudes less than the sensor
measurement range. The results of sections 3.4.3, 3.4.4 and 4.3, prove that, at
least with a high quality data acquisition system, this is possible, even if the
channels output voltage is of the order of ten micro-volts (see section 3.4.3).
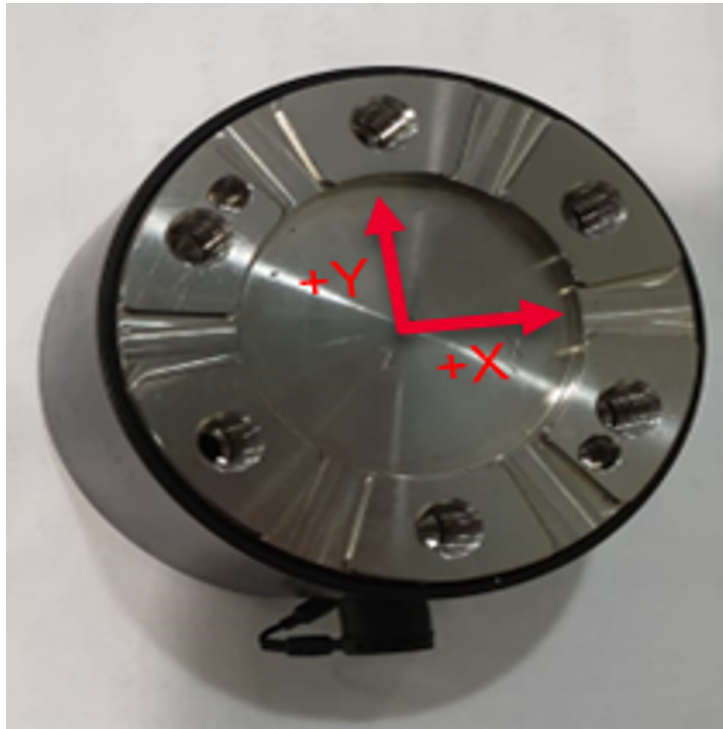
(a)
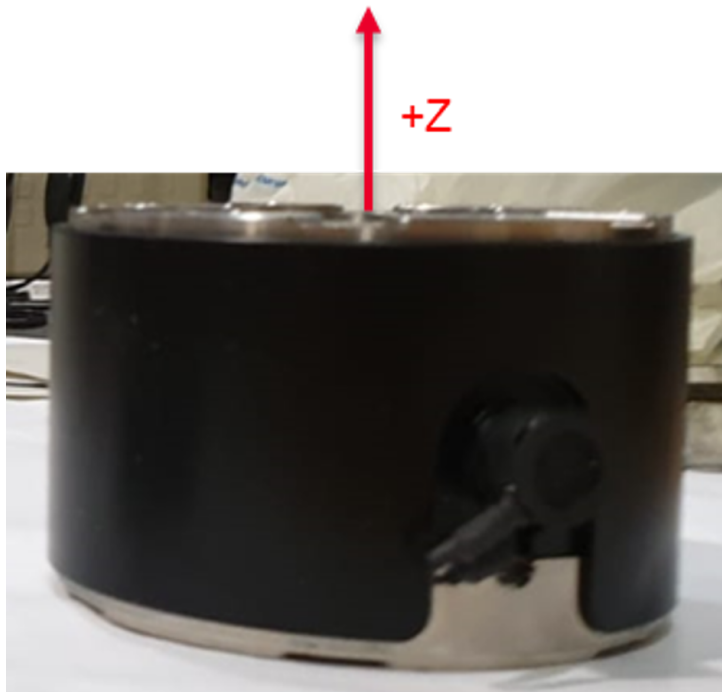
(b)

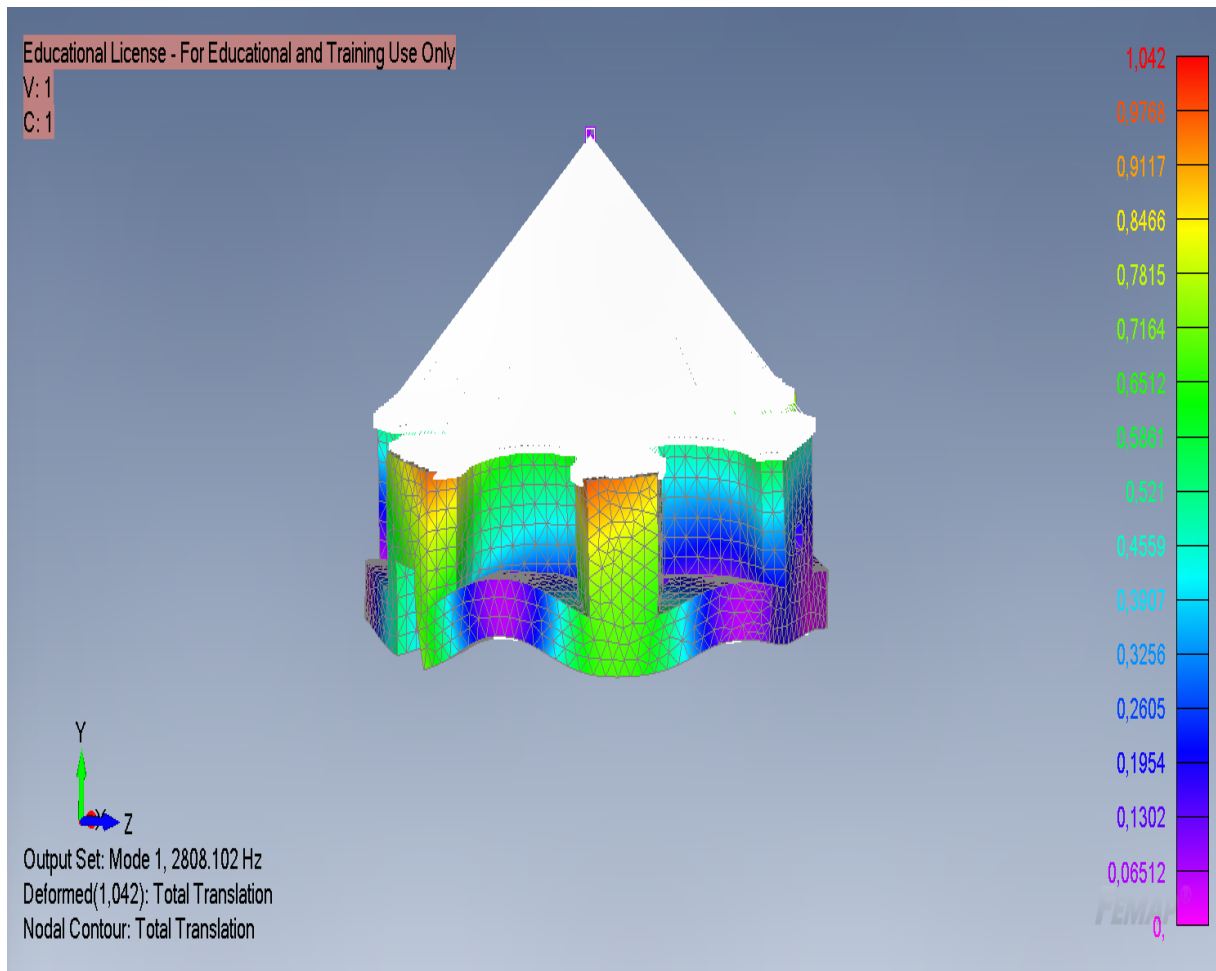Figure 3.24: Load cell axes. **Coordinate origin is at center of contact plane**

Figure 3.25: 6A80C interface first structural mode

3.4.1. Design of the mechanical interface

Clearly it was necessary to design and produce a mechanical interface consisting of two parts, the most critical and complex of which is shown as **6A80C interface** in Figure 3.26. The mechanical drawing of this part can be found in appendix A. A normal modes analysis of the **6A80C interface** alone was carried out with Nastran to check that the frequencies of its structural modes were well above the frequency range of interest, as shown in Figure 3.25. For this analysis a FEM model was used, in which the 6A80C interface was modelled by solid parabolic elements, the LTU was modelled by a rigid body element and a concentrated mass element placed in its estimated CG, and the part was clamped at the six mounting holes to the load cell.

(a)
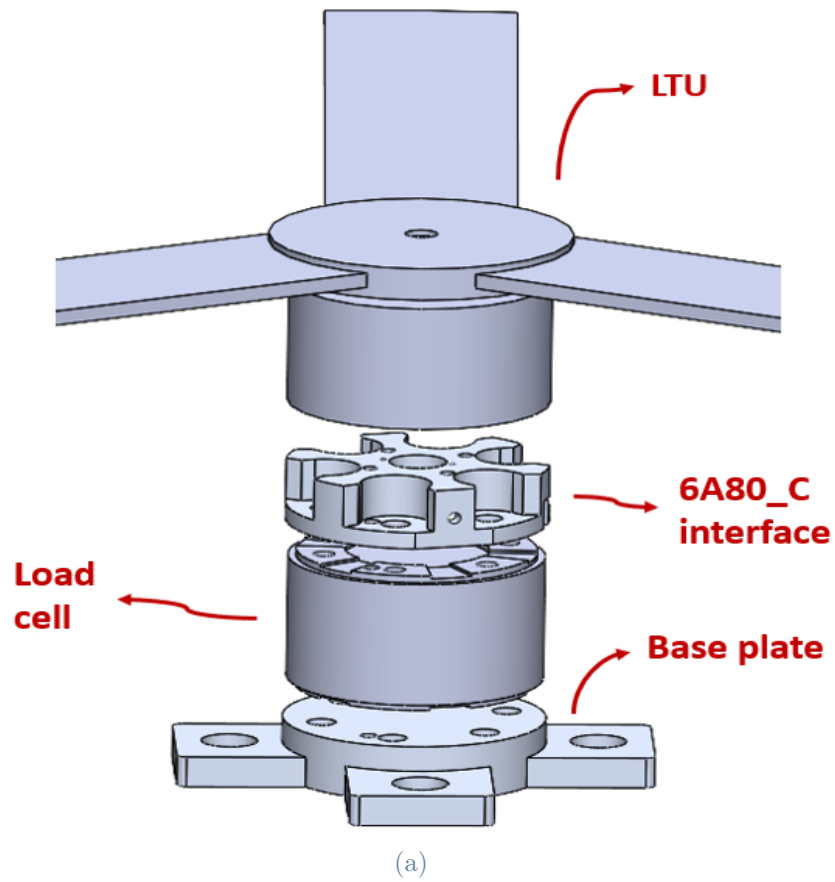
(b)

Figure 3.26: 6A80C-based measurement setup

3.4.2.   Shaker tests

Two shaker tests were performed on the setup without the mounted propeller and with the motor blocked. In the first one, depicted in Figure 3.27 the load cell was excited in the its $X-Y$ plane, at $30°$ angle from its Y-axis. The shaker was mounted on a rigid block, also shown in Figure 3.27. From the geometry of Figure 3.27, it is clear that equation 3.1 yields for this case :

$$
\begin{aligned}
M_x^c &= hF_{ref}\cos(30°) \\
M_y^c &= -hF_{ref}\sin(30°) \\
M_z^c &= 0 \\
F_x^c &= -F_{ref}\sin(30°) \\
F_y^c &= F_{ref}\cos(30°) \\
F_z^c &= 0
\end{aligned}
\tag{3.25}
$$

since :

$$r = 0.039 \ m \tag{3.26}$$
$$h = 0.012 \ m \tag{3.27}$$
$$\theta = 210° \tag{3.28}$$
$$F_x' = -F_{ref}\sin(30°) \tag{3.29}$$
$$F_y' = F_{ref}\cos(30°) \tag{3.30}$$
$$F_z' = 0 \tag{3.31}$$

The values of the relevant parameters were :

- $FS = 3200$ Hz
- $f_{in} = 2$ Hz
- $f_{fin} = 700$ Hz
- $\Delta f = 0.5$ Hz

(a)
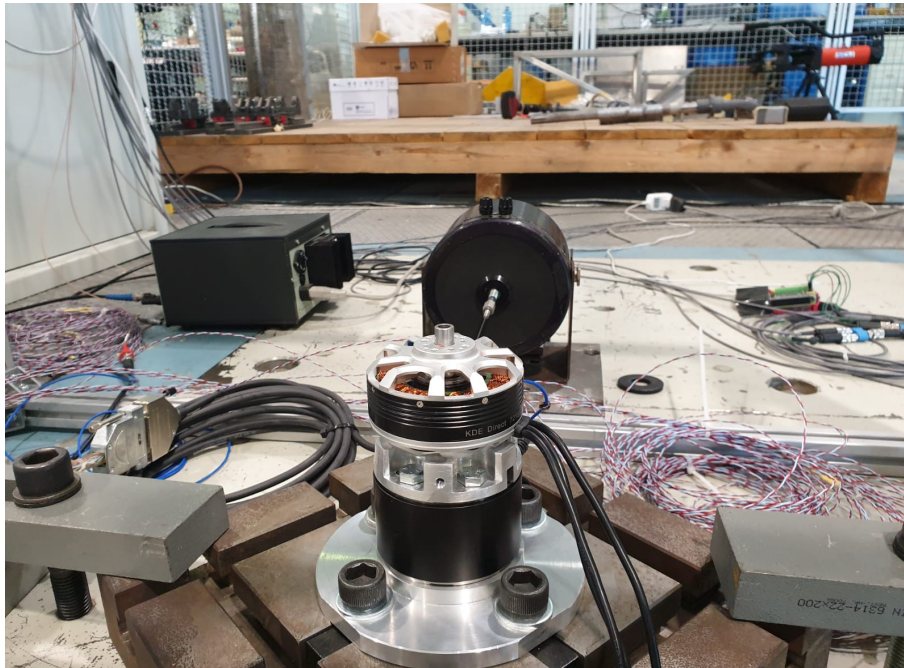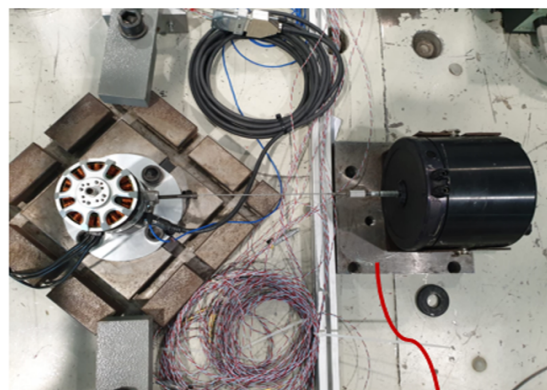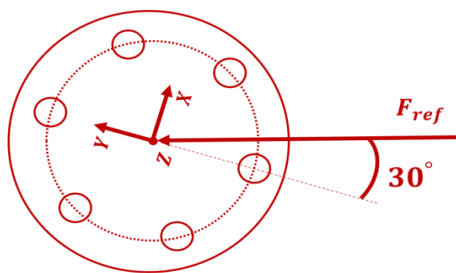
(b)

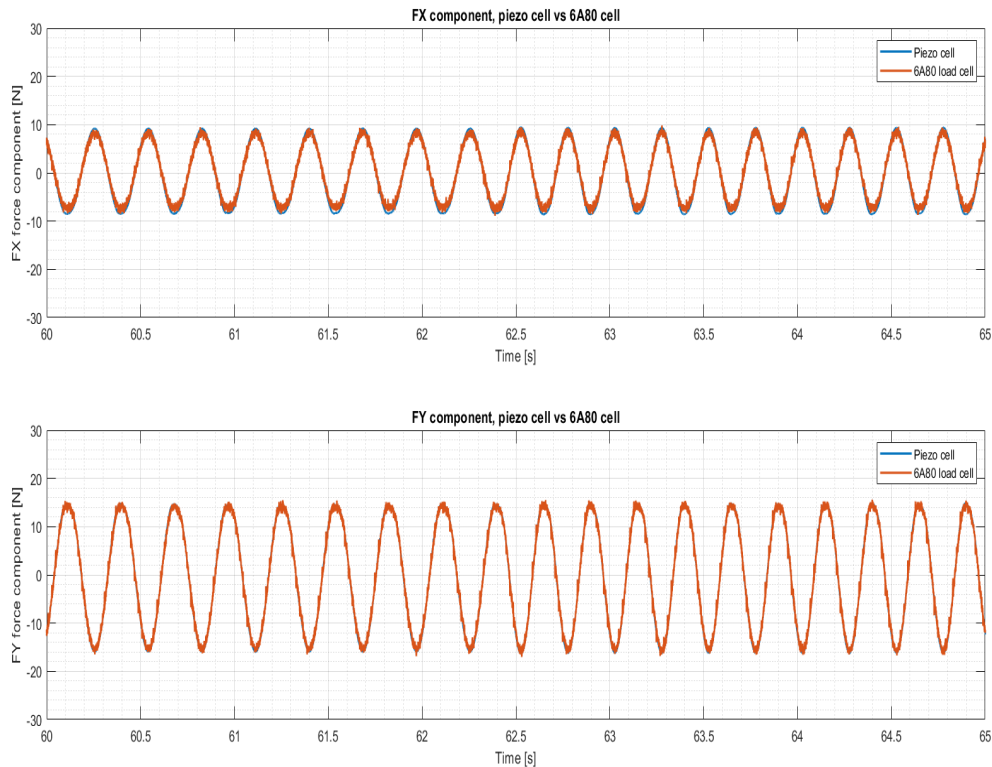Figure 3.27: Shaker test, in-plane excitation force

Figure 3.28: F_X and F_Y time histories

3.4.3. Shaker tests results

For the usual reasons, a representative portion of F_X and F_Y time histories is reported in Figure 3.28 for the in-plane (first) shaker test. **The dynamic components of the non-dimensional voltage output of each channel are reported in Figure 3.29 to give an idea of the voltage range they are in. Since in this test $V_{ref} = 5V$, it can be seen that the (dimensional) voltage outputs are of the order of ten micro-volts**. The FRFs of F_X, F_Y, M_X and M_Y are reported in Figures 3.30, 3.31, 3.32 and 3.33, respectively.

3.4.4. Analysis of shaker test results and conclusion

From the FRFs plots, specially from those of M_X and M_Y, it is clear that a first resonance takes place at roughly 200 Hz, which is the same highly damped motor resonance it was detected when testing the piezoelectric setup (see section 3.3.3). Two other resonances are visible, one at roughly 500 Hz and the other at roughly 700 Hz. Additional tests were subsequently performed (see Figure 3.34) in which the system was also excited in the load
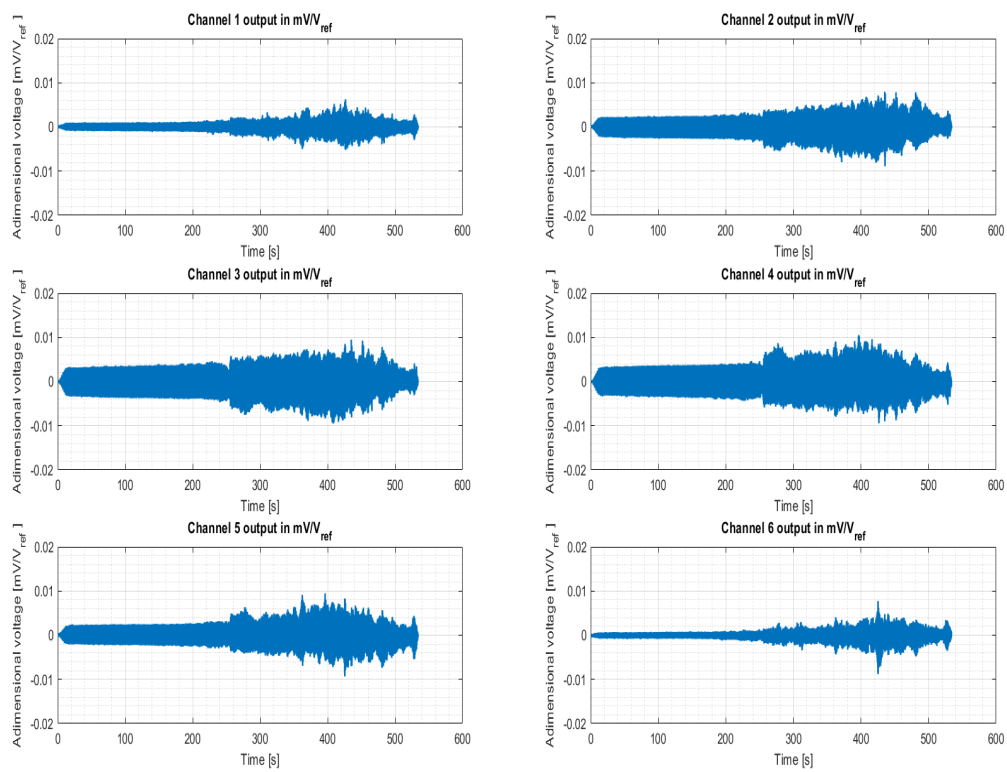
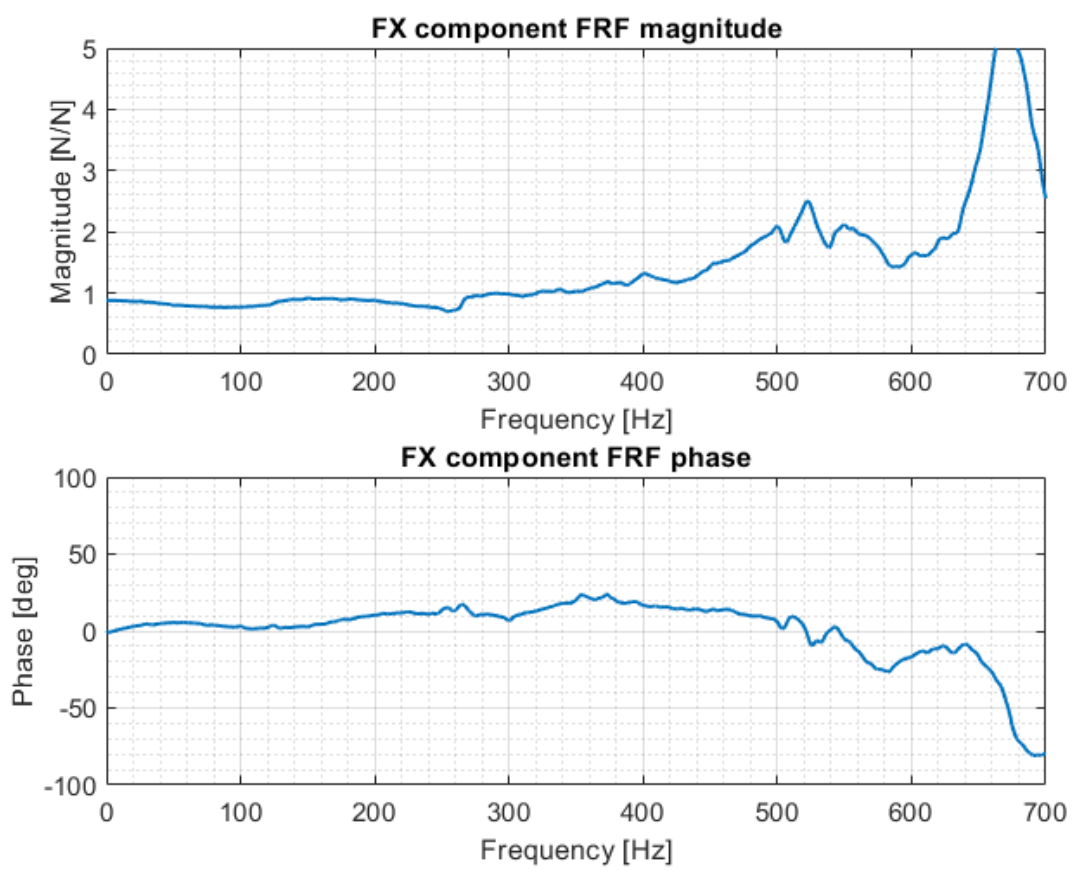Figure 3.29: Dynamic components of channels non-dimensional voltage output
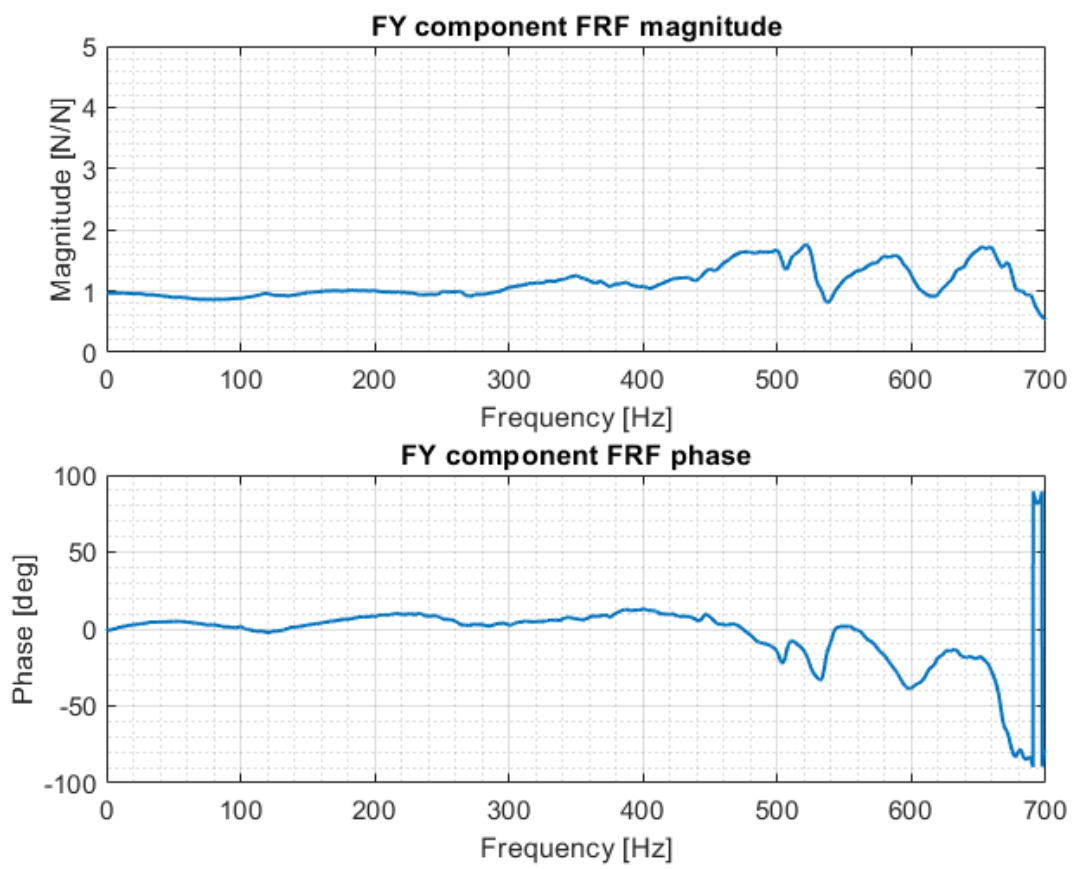
Figure 3.30: FX component FRF
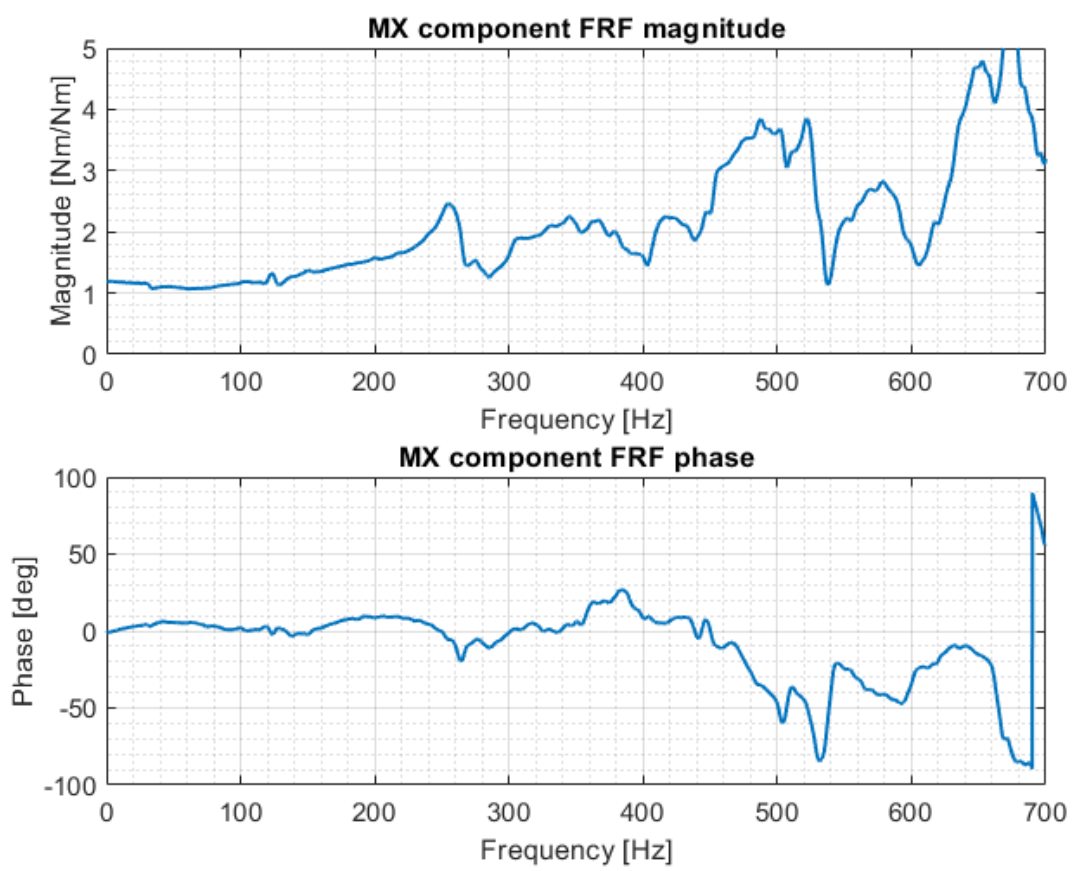
Figure 3.31: FY component FRF
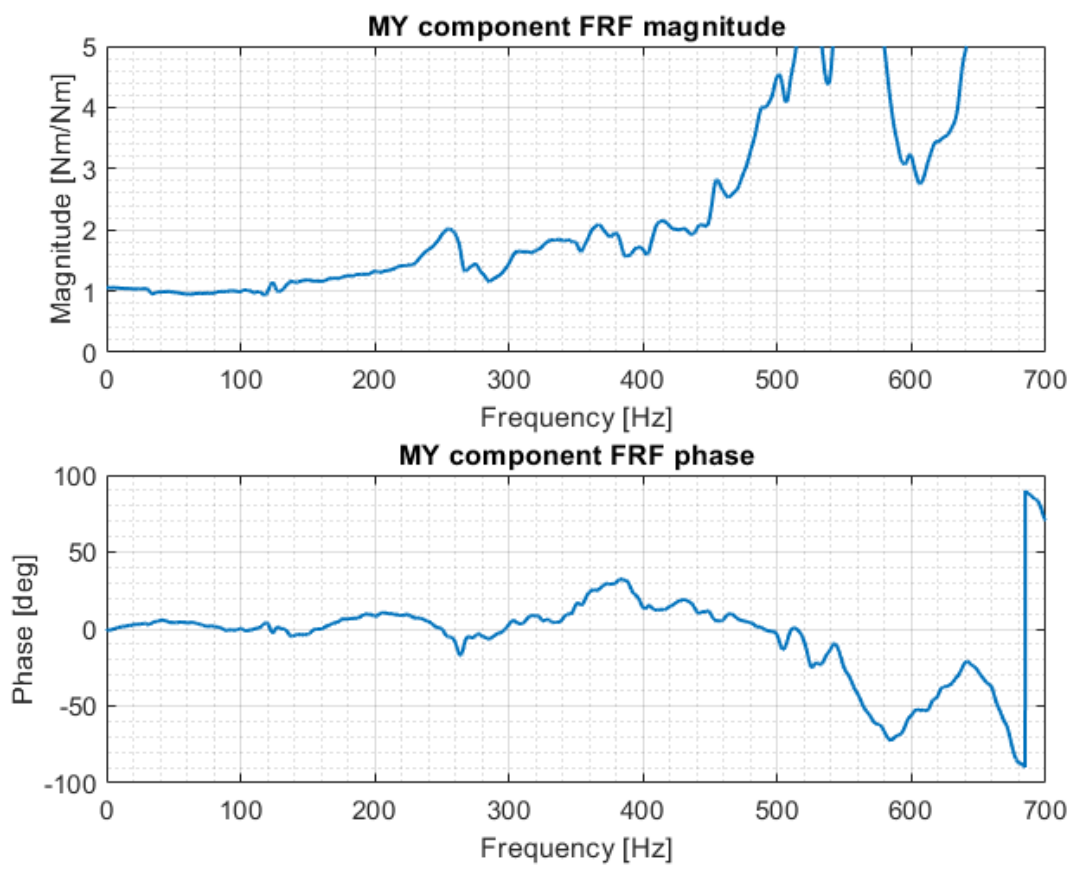
Figure 3.32: MX component FRF

Figure 3.33: MY component FRF

cell "Z" direction and in which accelerometers were used to monitor the dynamic response of the various parts of the test setup (stinger, load cell base plate, load cell interface,etc.). The results of this tests, besides yielding the FRF of the F_Z force component (which could not be derived from the previous test), yielded a value of roughly 700 Hz for the load cell resonance frequency. This means that the 500 Hz resonance peak found in the previous test was associated with the foundation (possibly to the base plate). **Therefore it can be concluded that the measurement system can be employed in the [0 250] Hz frequency range of interest**. [12]

---

[12]with possibly a post-processing correction for the non-ideal behaviour of its FRFs
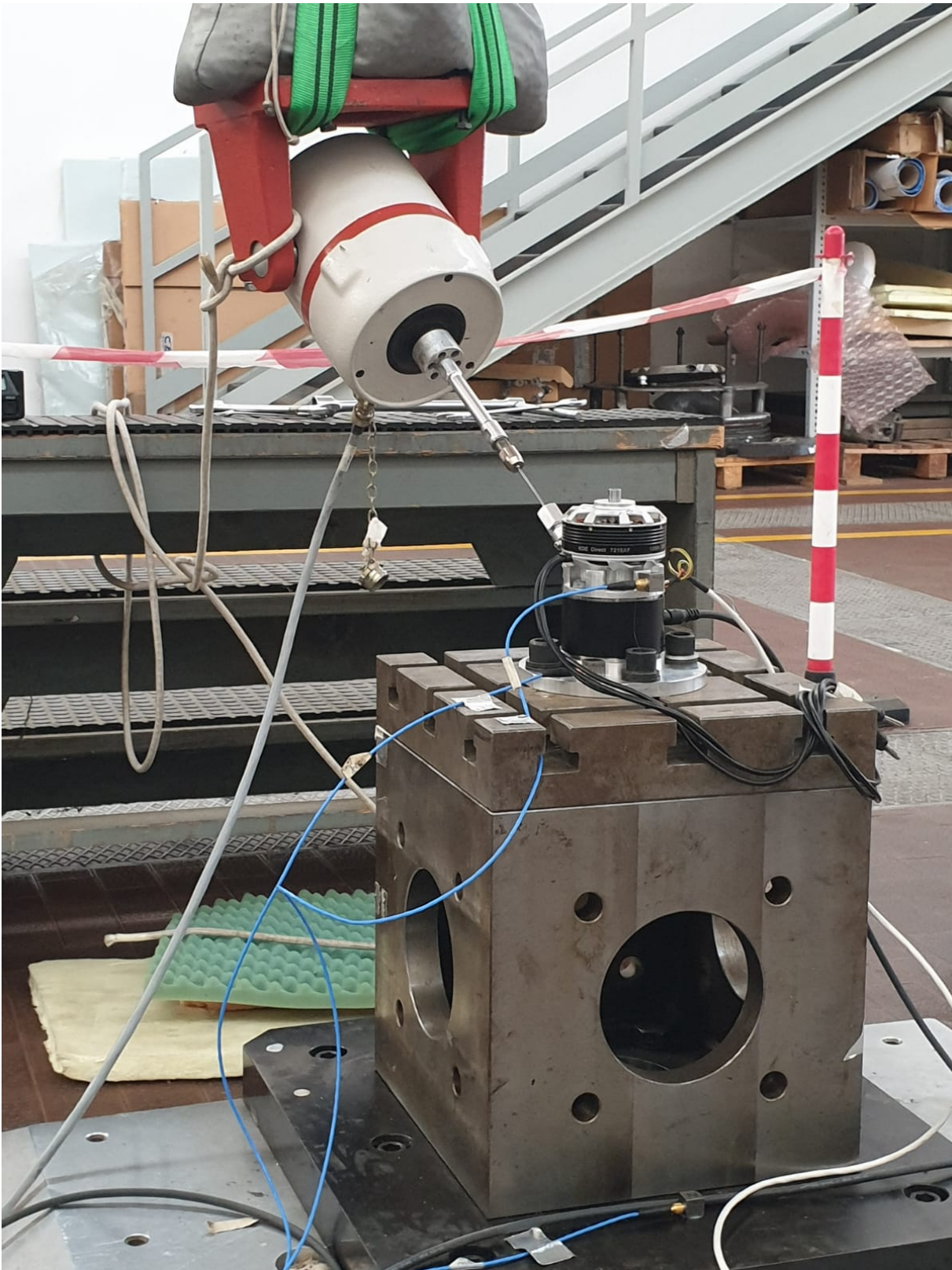
Figure 3.34: Additional shaker test, out-of-plane excitation force

4 | Measuring LTU loads

Several tests were performed to measure the magnitude of both the static and dynamic contributions of the LTU force/moment components. A first set of tests was performed with the 6ADF80-based measurement system (see Figure 4.1) to measure the LTU static loads, i.e. the mean values of the loads, only [1]. A second set of tests was performed to measure the LTU dynamic loads, with particular attention to the Fourier magnitude of the 3/rev harmonic component of the LTU loads [2], with the **piezoelectric measurement system** discussed in section 3.3, and afterwards a third set was performed with the **6A80C-based system** described in section 3.4 to measure both static and dynamic loads. **In each test the LTU loads were measured at a given RPM value**, which was set by setting the value of the PWM duty cycle via the LCD display (see section 2.1.1). In each test the motor was powered with a voltage of 43.5 V from the DC power supply. The RPM value was either measured with the RPM Hall Effect Sensor (see section 2.2) or determined by reading and dividing by 3 the frequency of the peak associated with 3/rev harmonic in the Fourier amplitude spectrum of the thrust (or any other force/moment component)

4.1. LTU dynamic loads with piezoelectric measurement system

The LTU dynamic loads were first measured at varying RPMs with the piezoelectric system (see Figure 4.2), both in "Hover flight condition" and in "Forward flight condition", which was crudely simulated by means of a fan delivering an airflow of 32.5 km/h (measured by a propeller anemometer) at the center of the propeller. The time duration of each test was 20 seconds and the sampling frequency 12800 Hz. The time histories of the forces F_1, F_2 and F_3 on the three piezoelectric load cells were again read via the SCADAS

---

[1]In fact, it was concluded (see section 3.2.5) that this measurement system is not suitable to measure dynamic loads in the frequency range of interest. Actually some load measurement tests were nevertheless performed, and in these tests very pronounced jumps were indeed observed in the amplitude of harmonic components when approaching the load cell resonance frequency

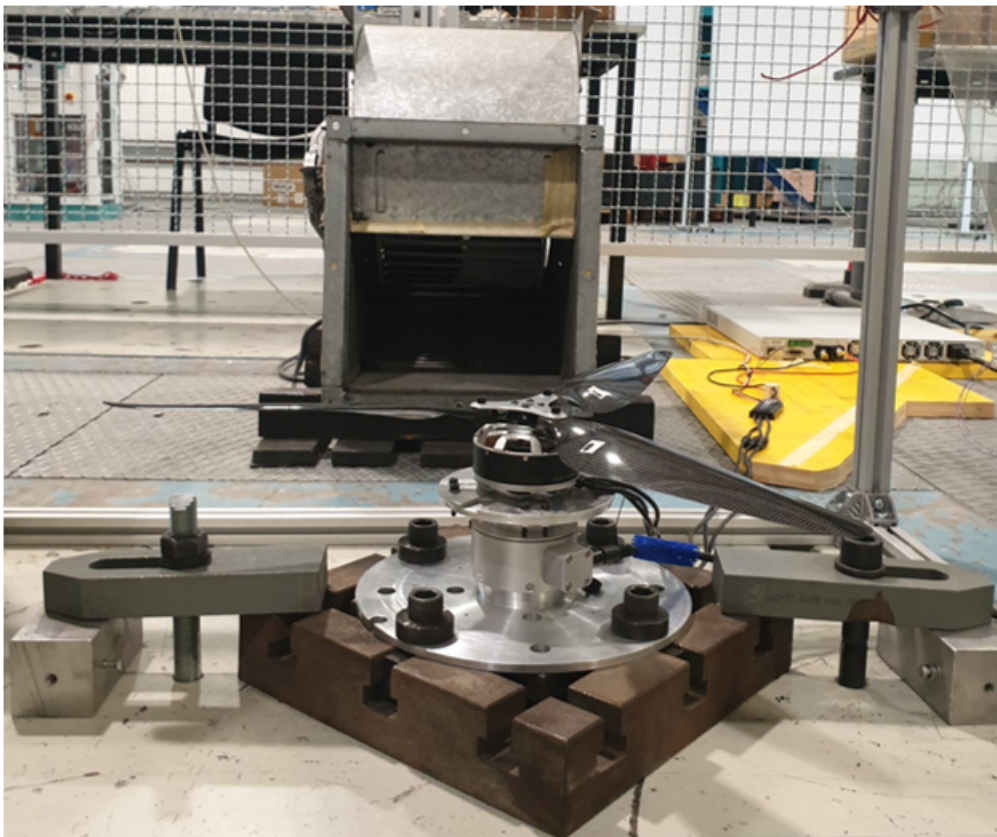[2]Clearly with piezoelectric load cells it is not possible (or at least easy) to measure static loads

Figure 4.1: 6ADF80-based system for measuring LTU static loads

V24-II card (see Figure 3.6) and, from those, the time histories of the F_Z (Thrust) M_X, and M_Y components [3] were computed using equations 4.1 (refer to Figure 4.3 and to section 3.3.1) :

$$F_Z = F_1 + F_2 + F_2$$
$$M_X = d_2 \frac{(2F_2 - F_1 - F_3)}{2\sqrt{3}} \qquad (4.1)$$
$$M_Y = d_2 \frac{(F_3 - F_1)}{2}$$

The Fourier magnitude spectra of the load components were obtained from the corresponding time histories as follows (for more details on the mathematics involved see section 3.2.3) :

- The time histories of the load components are divided into N_{tb} equal time blocks of data (typically from 25 to 30)

- An FFT is performed for each time block separately [4]

- From the FFTs, the corresponding autopower spectrum is computed for each load component and for each time block

- The average of all N_{tb} autopower spectra is computed for each load component

- The Fourier magnitude spectra of each load component is computed by taking the (real) square root of the corresponding average autopower spectra

As an example, in Figure 4.4 the raw magnitude spectrum of F_Z (thrust) is compared, for a particular test in hover, with the one obtained from the averaged autopower.

In Figures 4.5, 4.6, 4.7, the magnitude in hover of the 3/rev harmonic of F_Z, M_X and M_Y, respectively, is compared to the one in forward flight at different RPMs. The results are also reported in tabular form in Tables 4.1 and 4.2

---

[3]It should be recalled that these are the only components which can be measured by the piezoelectric setup (see section 3.3)

[4]No window function was applied

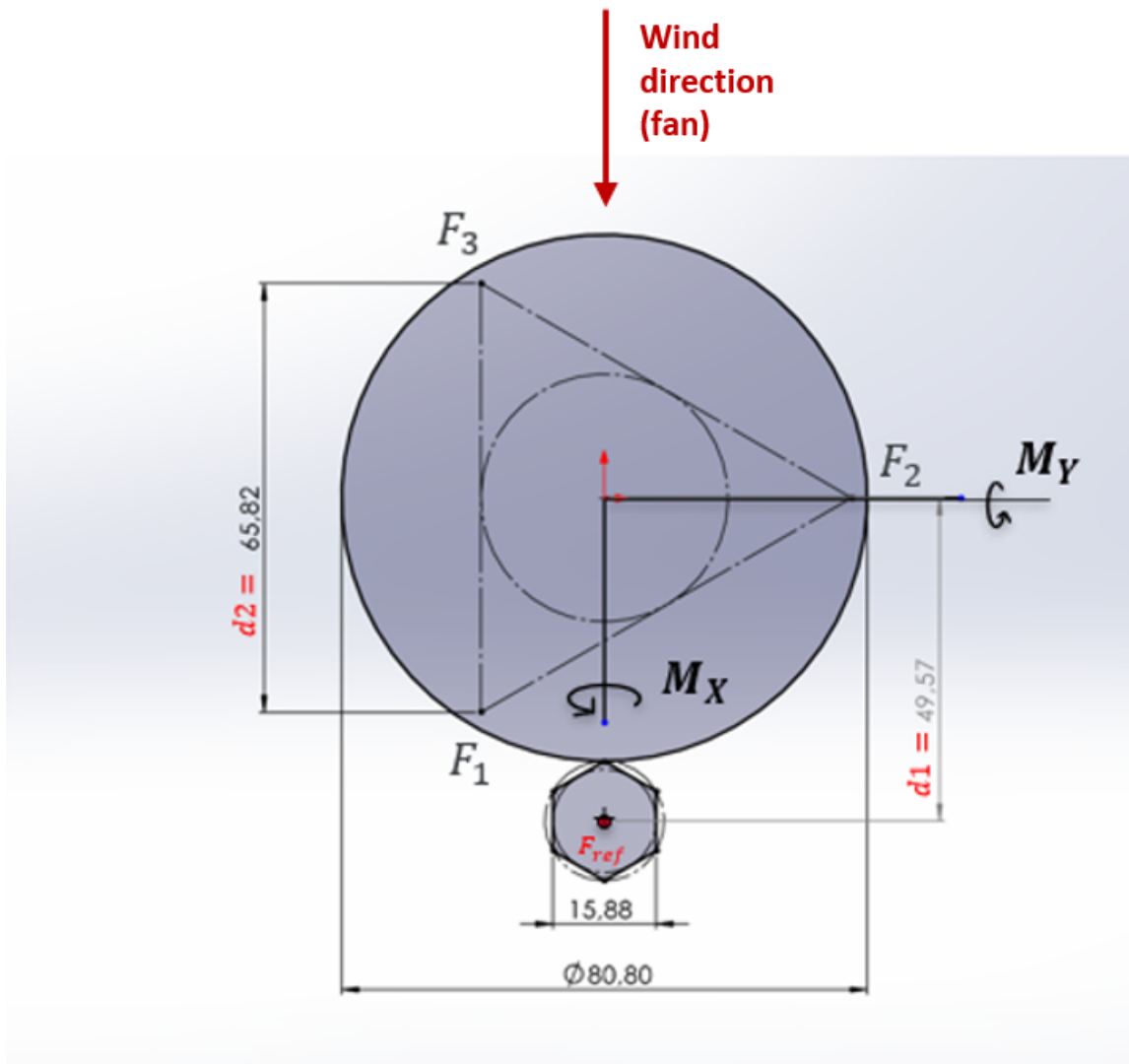Figure 4.2: Piezoelectric system for measuring LTU loads

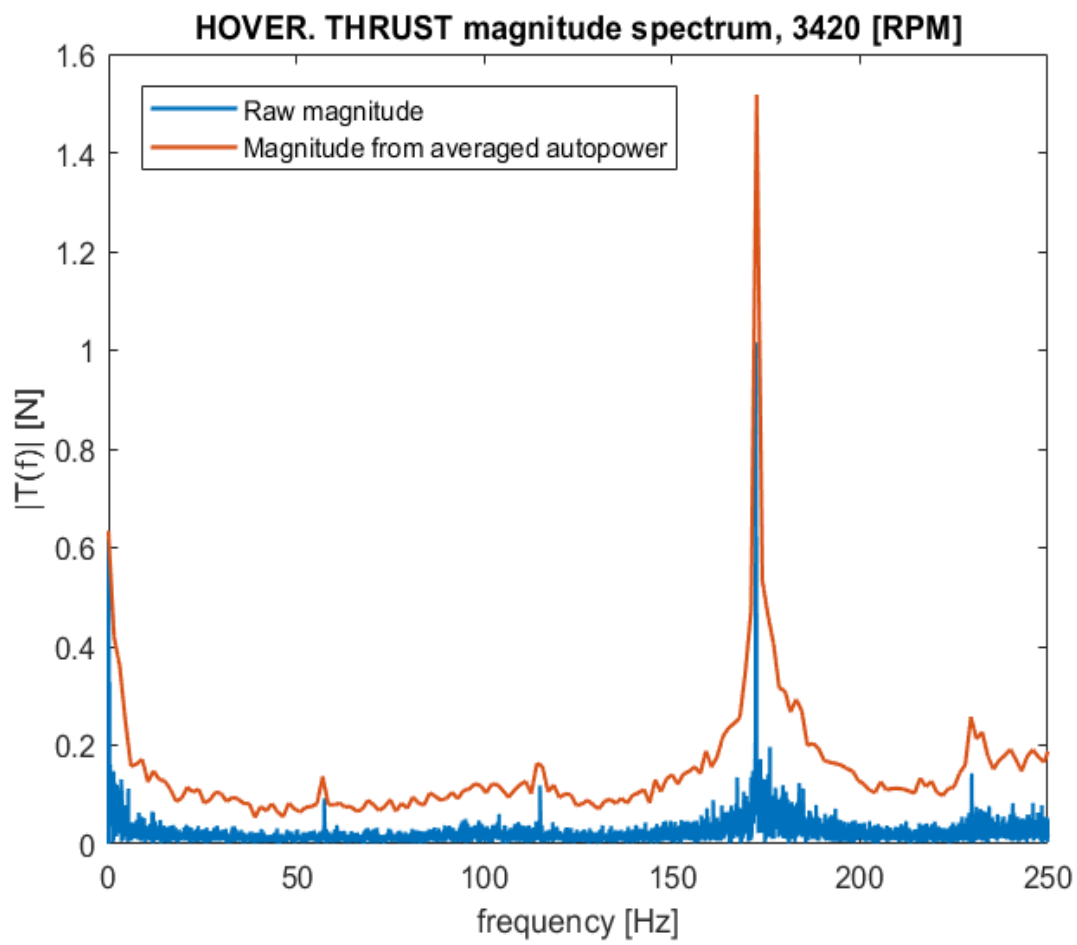Figure 4.3: Piezoelectric measurement system geometry
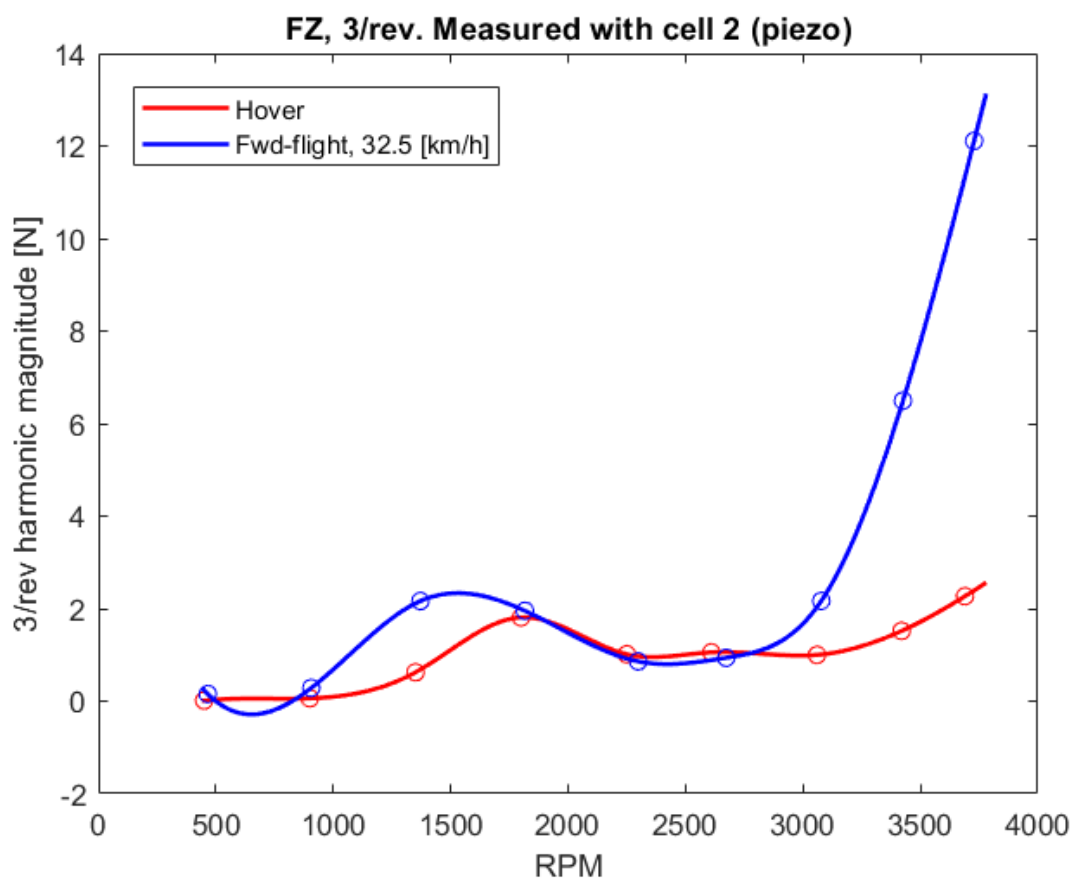
Figure 4.4: Raw vs "averaged" magnitude spectrum
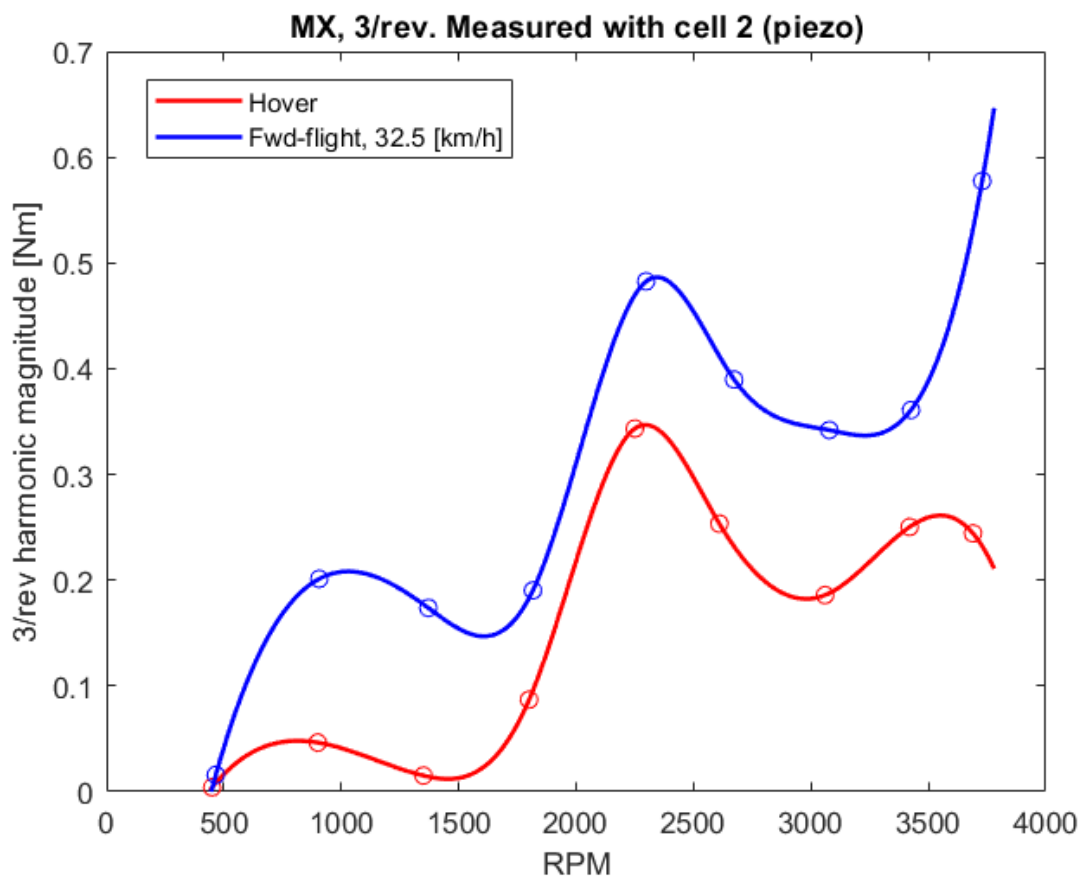
Figure 4.5: F_Z magnitude, hover vs forward flight

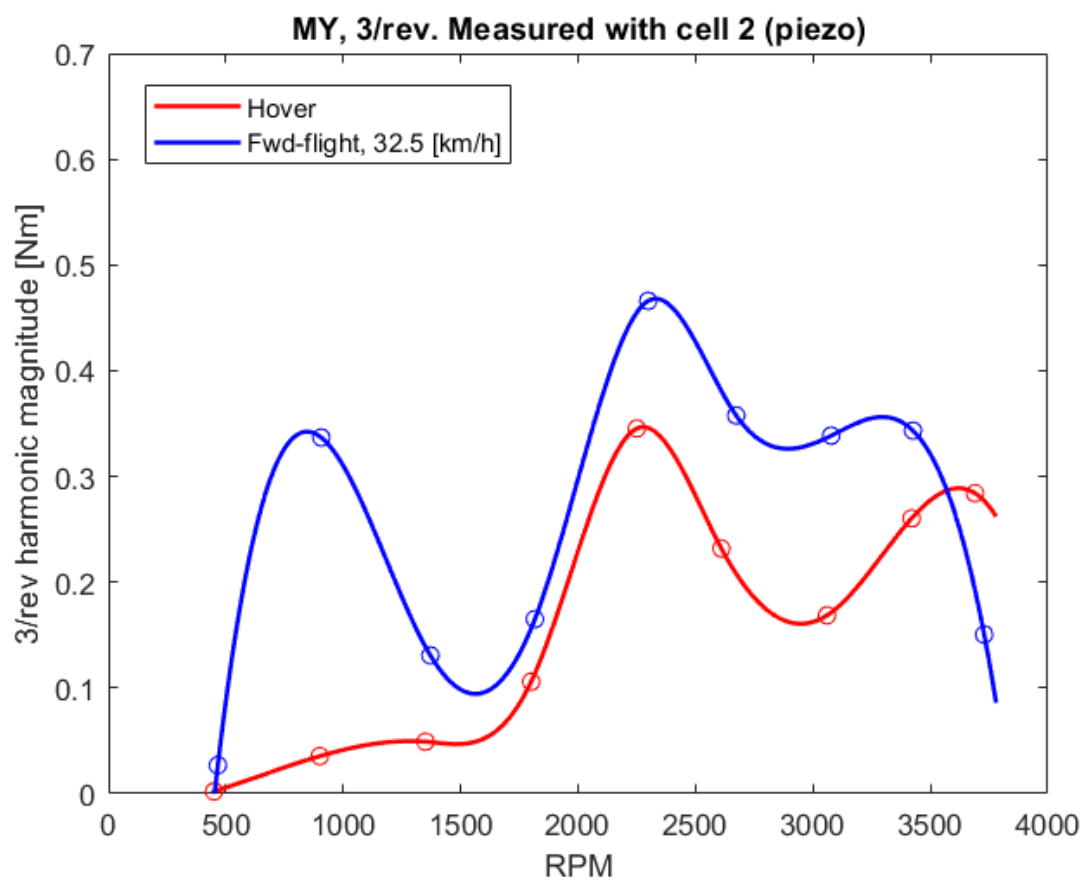Figure 4.6: M_X magnitude, hover vs forward flight

Figure 4.7: M_Y magnitude, hover vs forward flight

RPM	F_Z 3/rev [N]	M_X 3/rev [Nm]	M_Y 3/rev [Nm]
450	0.0114938	0.00412	0.00206449
900	0.0614	0.0464266	0.0354741
1350	0.623374	0.0152132	0.0491471
1800	1.80958	0.0870017	0.105871
2250	1.01401	0.343377	0.345387
2610	1.05544	0.253373	0.231871
3060	1.00023	0.185905	0.168588
3420	1.51793	0.250301	0.260327
3690	2.26826	0.244258	0.284128

Table 4.1: 3/rev harmonic magnitude in Hover

RPM	F_Z 3/rev [N]	M_X 3/rev [Nm]	M_Y 3/rev [Nm]
450	0.153204	0.015865	0.02694
900	0.284873	0.201253	0.336798
1350	2.1642	0.173756	0.13074
1800	1.95261	0.190325	0.165025
2250	0.859184	0.482565	0.466025
2610	0.937626	0.389681	0.357666
3060	2.16626	0.341955	0.338535
3420	6.4938	0.360844	0.343273
3690	12.1102	0.577489	0.150508

Table 4.2: 3/rev harmonic magnitude in Forward Flight

4.2. LTU static and dynamic loads with 6A80C-based system

A set of tests was also performed to measure both LTU static and dynamic loads with the 6A80C-based measurement system (see Figure 4.8. The time duration of each test was again of 20 seconds, the six channels voltages were read via the SCADAS VB8III-RT CARD (see Figure 3.6), and from these, the time histories of all the six force and moment

components were computed using the 6x6 load cell static calibration matrix **MC**. In fact, for each time instant one can write:

$$\mathbf{FM} = \mathbf{MC} \cdot \mathbf{V_{ch}} \tag{4.2}$$

in which V_{ch} is the column vector containing the non-dimensional voltages (in this case in mv/V) of the channels (in the proper order) at a certain instant of time, and $\mathbf{FM} :=$ $[F_X, F_Y, F_Z, M_X, M_Y, M_Z]^T$ [5] is the column vector of loads at the same instant of time. The static loads are by definition the mean values of the loads time histories computed via equation 4.2, while the Fourier magnitude spectra of the load components (dynamic loads) were obtained by the same method described in section 4.1

4.3. Comparison between static and dynamic loads measured with different measurement system

Figures 4.9 and 4.10, show a comparison between the static components of thrust (F_Z) and torque (M_Z), respectively, measured with the 6ADF80 system, the 6A80C system, and those measured by the LTU supplier [6]. The relatively small discrepancy between the 6ADF80 and the 6A80C results is likely due to the different distances of propeller from ground and to different air conditions. In Figure 4.11 some F_Z (thrust) magnitude spectra in hover obtained with the piezoelectric system (indicated by "Cell 2" in the Figure) are compared with some spectra obtained with the 6A80C based system (indicated by "Cell 3") at different but comparable RPM values.

---

[5]see section 3.4 for the definition of these components

[6]The torque according to the supplier was calculated by multiplying by the motor torque constant K_t the value of the battery current I_{dc} measured by the supplier (see Appendix B)
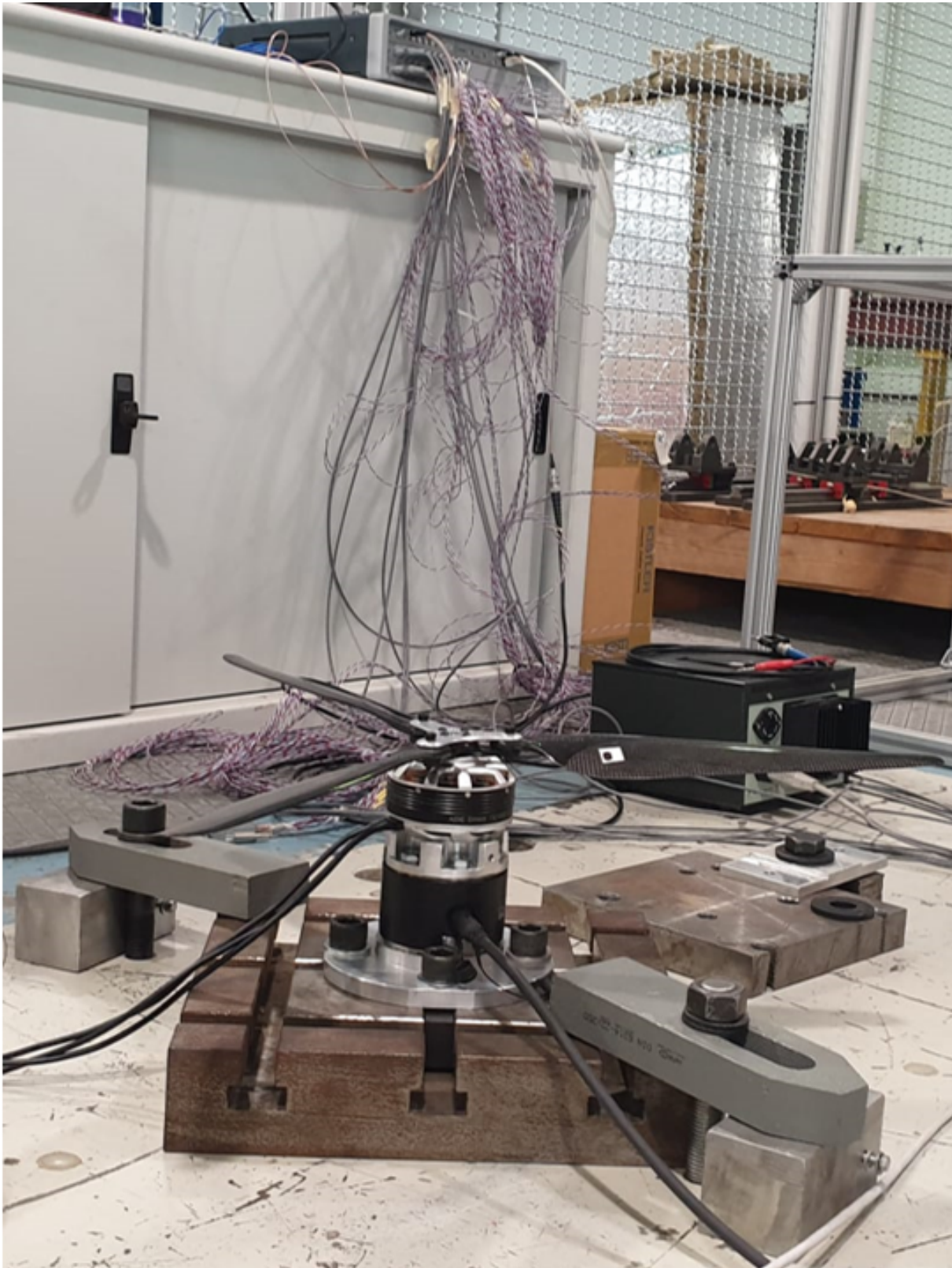
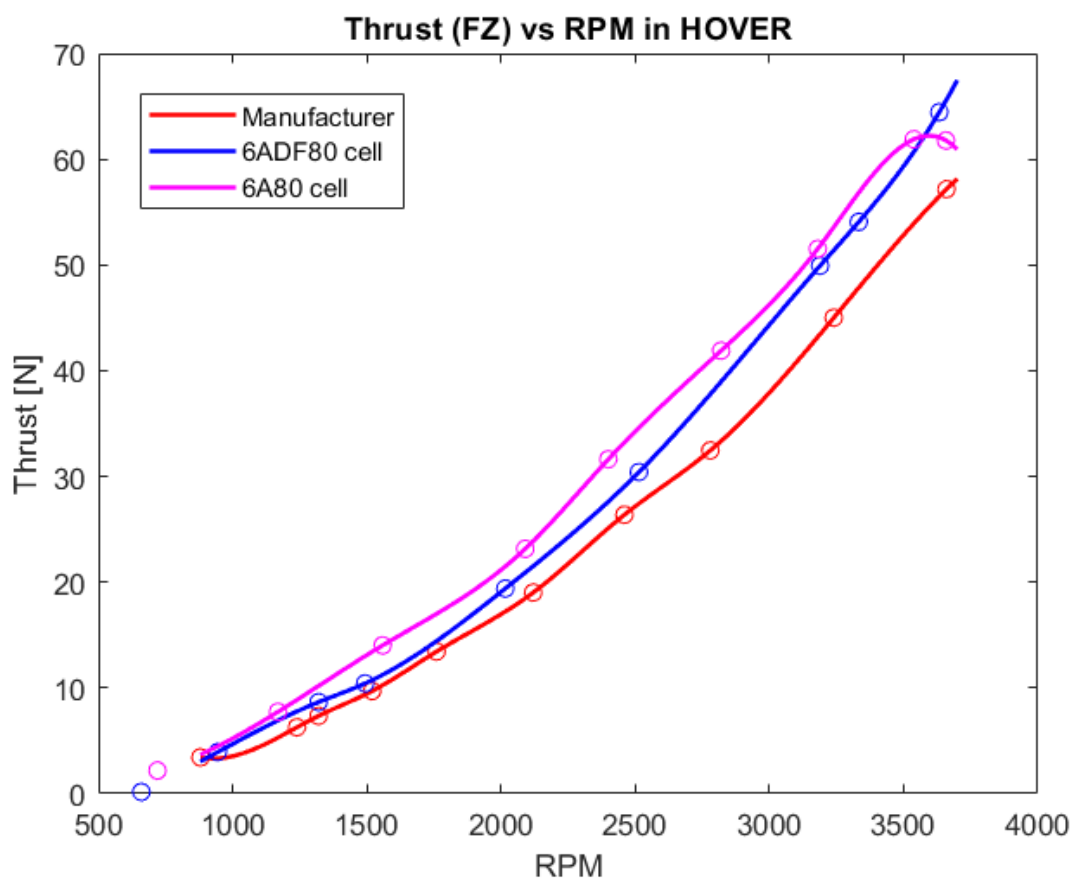Figure 4.8: 6A80C-based system for measuring LTU loads

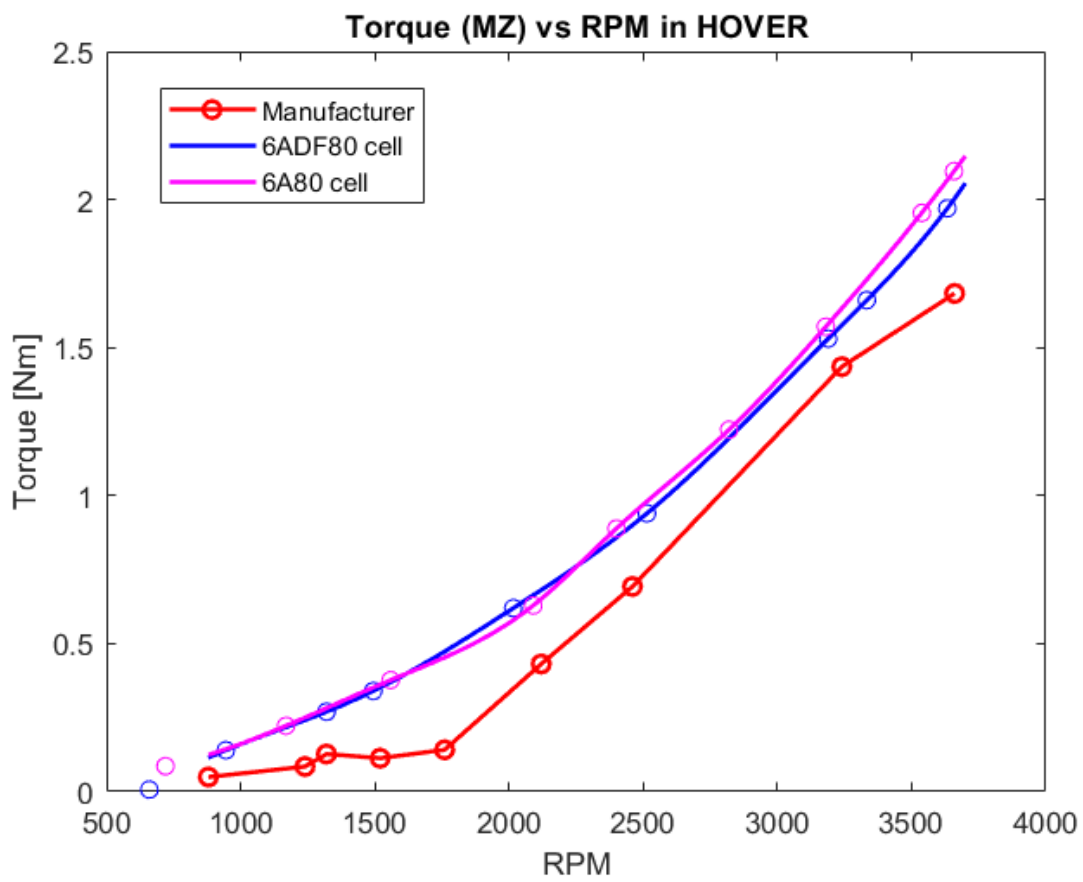Figure 4.9: LTU static thrust comparison
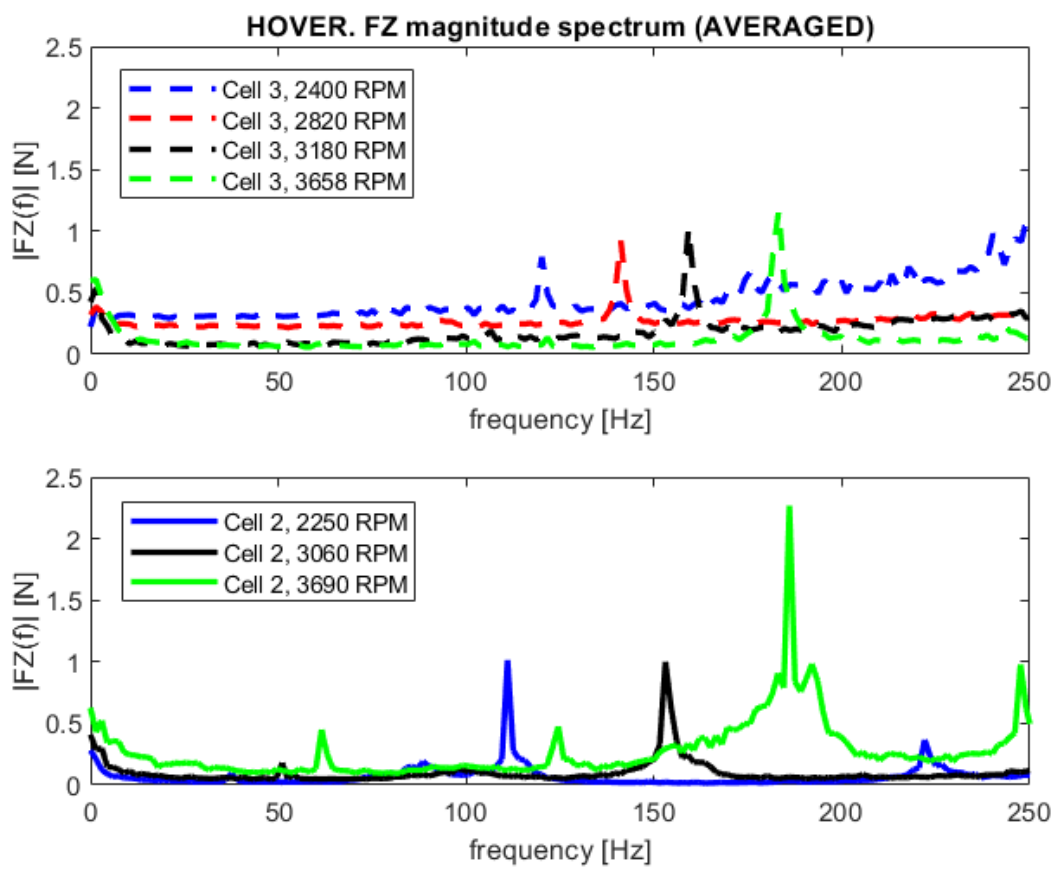
Figure 4.10: LTU static torque comparison

Figure 4.11: Comparison between Piezo (cell 2) vs 6A80C (cell 3) magnitude spectra

5 | Conclusions and future developments

In this thesis, a cost-effective, single LTU test rig capable of driving the LTU at constant RPM and of measuring all the six components of static and dynamic loads in the 250 Hz frequency range was presented. It was shown that, with the given ESC, a satisfactory open-loop control can be achieved by programming a relatively simple MCU, and that a custom, programmable Hall sensor PCB is a relatively simple and cost-effective option to implement a closed-loop RPM control. It is deemed necessary, especially in view of the possible need of programming the MCU for a closed-loop RPM control for wind tunnel measurements, to further assess the precision and bandwidth of the designed RPM sensor. In view of the future use of the test rig for wind tunnel measurements, the electrical drive system presented in this work could be used to either simultaneously or independently control the RPM of multiple LTUs. Furthermore the wind tunnel control system for the tilt angle should be assessed and possibly incorporated in the electrical drive system to finally obtain a basic flight controller. The method for the preliminary choice of motors, ESCs and PS presented in Appendix B may be improved, without compromising too much its simplicity, by introducing temperature dependency of the parameters into the equations, and by bringing into the picture further requirements relating to safety and noise level. The static loads were measured and the thrust and torque components were found to be in very good agreement between the different measurement systems designed and the LTU manufacturer. As far as dynamic loads are concerned, it was concluded that the piezoelectric and the 6A80C-based system are both suitable to measure loads in the specified frequency range provided that the support they are mounted on responds dynamically only at a sufficiently high excitation frequency. This latter assumption is particularly important again in connection to the future use of the test rig for wind tunnel measurements. In fact, the dynamic characteristics of the structure in the wind tunnel supporting the LTUs will have to be at least comparable with those of the supporting structures considered in this work. Moreover, the magnitude spectra of the loads obtained with the piezoelectric system compare successfully (the representative case of thrust was

reported) in the specified frequency range to those obtained with the 6A80C-based system. The number of load components the piezoelectric system is able to measure could be extended from three to all six by replacing, for example, the three uniaxial piezoelectric load cells with three, or better four triaxial piezoelectric load cells.

Bibliography

[1] ams OSRAM Group. As5600, 12-bit programmable contactless potentiometer wiring by botton side, 2018. URL `https://ams.com/documents/20143/36005/AS5600_DS000365_5-00.pdf/649ee61c-8f9a-20df-9e10-43173a3eb323`.

[2] R. E. Coleman. *Experimental structural dynamics*. AuthorHouse, 2004.

[3] K. Direct. Kde7215xf-135 brushless motor for heavy-lift electric multi-rotor (uas), 2022. URL `https://www.kdedirect.com/collections/uas-multi-rotor-brushless-motors`.

[4] K. Direct. Kde-cf245-tp propeller blades, 24.5" x 8.1, triple-edition series, 2022. URL `https://www.kdedirect.com/collections/multi-rotor-propeller-blades`.

[5] electronicsforu.com. How 16×2 lcds work | build a basic 16×2 character lcd, 2016. URL `https://www.electronicsforu.com/technology-trends/learn-electronics/16x2-lcd-pinout-diagram`.

[6] U. Elevate. Fast-forwarding to a future of on-demand urban air transportation. Technical report, UBER Elevate, 2016. URL `https://evtol.news/__media/PDFs/UberElevateWhitePaperOct2016.pdf`.

[7] I. G. et al. Analysis of the effect of the motor temperature to brushless direct current motor performance on karling electric vehicle. *Journal of Physics*, 2019.

[8] fishpepper. Tutorial: How to measure the kv of a brushless motor, 2017. URL `https://fishpepper.de/2017/10/17/tutorial-how-to-measure-the-kv-of-a-brushless-motor/`.

[9] A. forum. Lcd keypad shield for arduino and lcd 1602 wiring by botton side, 2013. URL `https://forum.arduino.cc/t/lcd-keypad-shield-for-arduino-lcd-1602-wiring-by-botton-side/177192`.

[10] A. forum. Liquidcrystal - liquidcrystal(), 2022. URL `https://www.arduino.cc/reference/en/libraries/liquidcrystal/liquidcrystal/`.

[11] L. Gipson. Advanced air mobility mission overview, 2021. URL `https://www.nasa.gov/aam/overview/`.

[12] T. Instruments. Field orientated control of 3-phase ac-motors. Technical report, Texas Instruments, 1998. URL `https://www.ti.com/lit/an/bpra073/bpra073.pdf`.

[13] A. Iqbal. Space vector pwm techniques. Encyclopedia Scholarly Community Encyclopedia, 2018. URL `https://encyclopedia.pub/entry/23`.

[14] W. Johnson. *Rotorcraft Aeromechanics*. Cambridge University Press, 2013.

[15] T.-Y. L. M.-K. S. Y.-J. Kim and S.-Y. Jung. Design and torque ripple analysis of brush-less dc motor according to delta winding connection. *Journal of Magnetics*, 2015.

[16] Z. W. K. Lu and F. Blaabjerg. A simple startup strategy based on current regulation for back-emf-based sensorless control of pmsm. *IEEE TRANSACTIONS ON POWER ELECTRONICS*, 2012.

[17] J. R. Mevey. Sensorless field oriented control of brushless permanent magnet synchronous motors. Master's thesis, KANSAS STATE UNIVERSITY, Manhattan, Kansas, 2009.

[18] E. V. News. Nasa greased lightning (defunct), 2022. URL `https://evtol.news/nasa-greased-lightning`.

[19] Press. Vahana has come to an end. but a new chapter at airbus has just begun, 2019. URL `https://www.suasnews.com/2019/12/vahana-has-come-to-an-end-but-a-new-chapter-at-airbus-has-just-begun/`.

[20] S. C. C. R. K. K. W. K. E. Romander. Comparing rotcfd predictions of the multirotor test bed with experimental results. Technical report, NASA, 2020.

[21] C. Russell and S. Conley. The multirotor test bed – a new nasa test capability for advanced vtol rotorcraft configurations. Technical report, NASA, 2020.

[22] M. K. Sekula and C. R. Russell. Time-frequency analysis of experimental and analytical hub loads of a rotor undergoing a rotor speed change. Technical report, NASA, 2022.

[23] SIEMENS. Multi input multi output mimo testing. SIMCENTER - TEST-ING, 2020. URL `https://community.sw.siemens.com/s/article/multi-input-multi-output-mimo-testing`.

[24] Y. SOLBAKKEN. Space vector pwm intro, 2017. URL `https://www.switchcraft.org/learning/2017/3/15/space-vector-pwm-intro`.

[25] L. SpA. Advanced air mobility: the new paradigm of safe and sustainable air transport services, 2022. URL `https://www.leonardo.com/en/focus-detail/-/detail/advanced-air-mobility`.

[26] A. Stoll and J. Bevirt. Development of evtol aircraft for urban air mobility at joby aviation. Technical report, Joby Aviation, 2022.

[27] A. Tantos. Sign-magnitude drive, 2011. URL `http://www.modularcircuits.com/blog/articles/h-bridge-secrets/sign-magnitude-drive/`.

[28] I. Technologies. Using ccu6e for bldc control with synchronous rectification (active freewheeling). Technical report, Infineon Technologies, 2008. URL `https://www.infineon.com/dgdl/AP0807810_XC866_CCU6E_for_BLDC_control.pdf?fileId=db3a30431be39b97011c1e1e6522783f`.

[29] I. Technologies. Pmsm foc motor control software using xmc™. Technical report, Infineon Technologies, 2017. URL `https://www.infineon.com/dgdl/Infineon-AP32370_PMSM_FOC_for_XMC1000-AN-v01_00-EN.pdf?fileId=5546d4625b3ca4ec015b3e42761006a8`.

[30] P. Vas. *Sensorless Vector and Direct Torque Control.* Oxford University Press, 1998.

[31] P. Yedamale. Brushless dc (bldc) motor fundamentals, an885. Technical report, Microchip Technology Inc., 2003. URL `http://ww1.microchip.com/downloads/en/AppNotes/00885a.pdf`.

[32] P. Yedamale. Using the pic18f2431 for sensorless bldc motor control. Technical report, Microchip Technology Inc., 2005. URL `https://ww1.microchip.com/downloads/en/AppNotes/00970A.pdf`.

[33] A. Zanotti. Experimental study of the aerodynamic interaction between side-by-side propellers in evtol airplane mode through stereoscopic particle image velocimetry. *MDPI*, 2021.
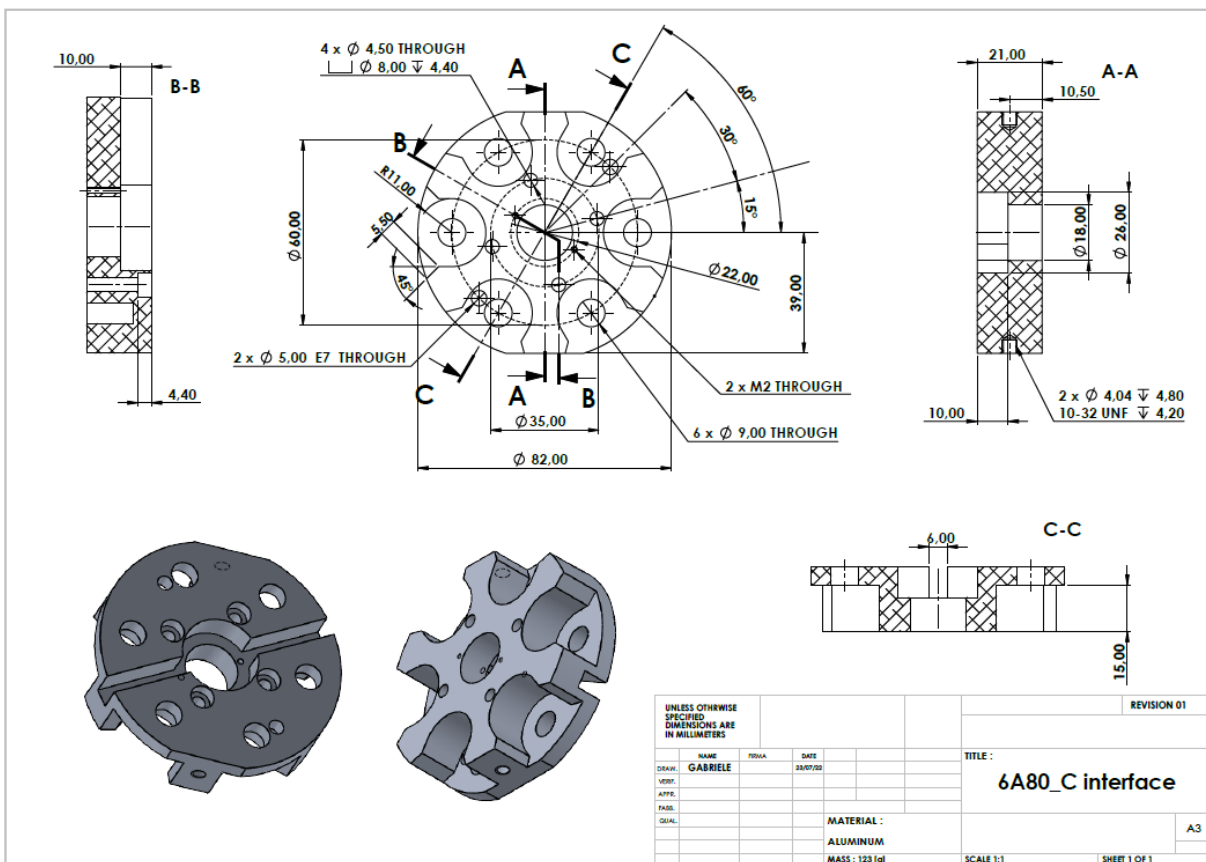
A | Appendix A - Mechanical Drawings

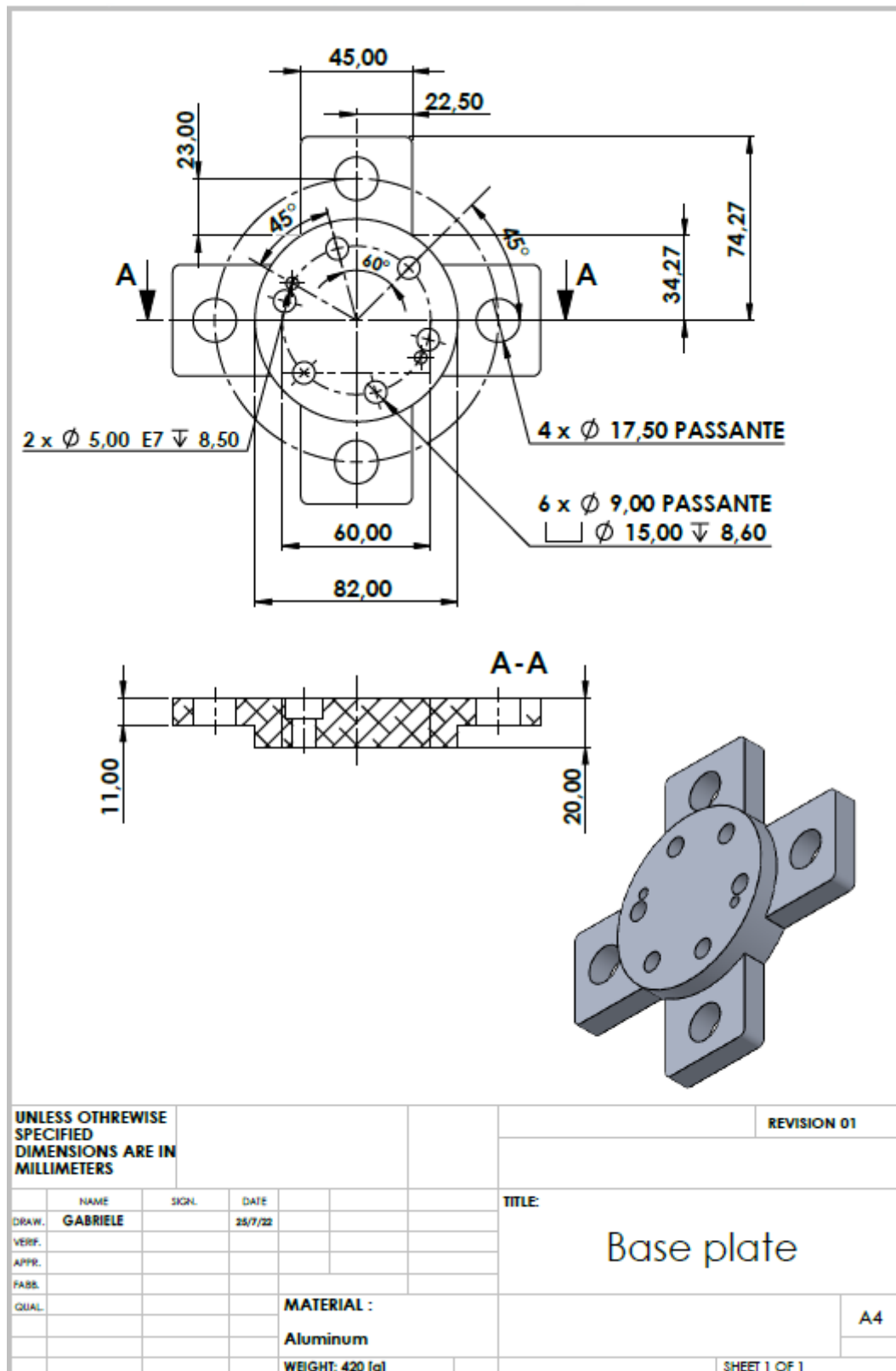Figure A.1: **"6A80_C interface"**, for 6A80_C-based measurement system

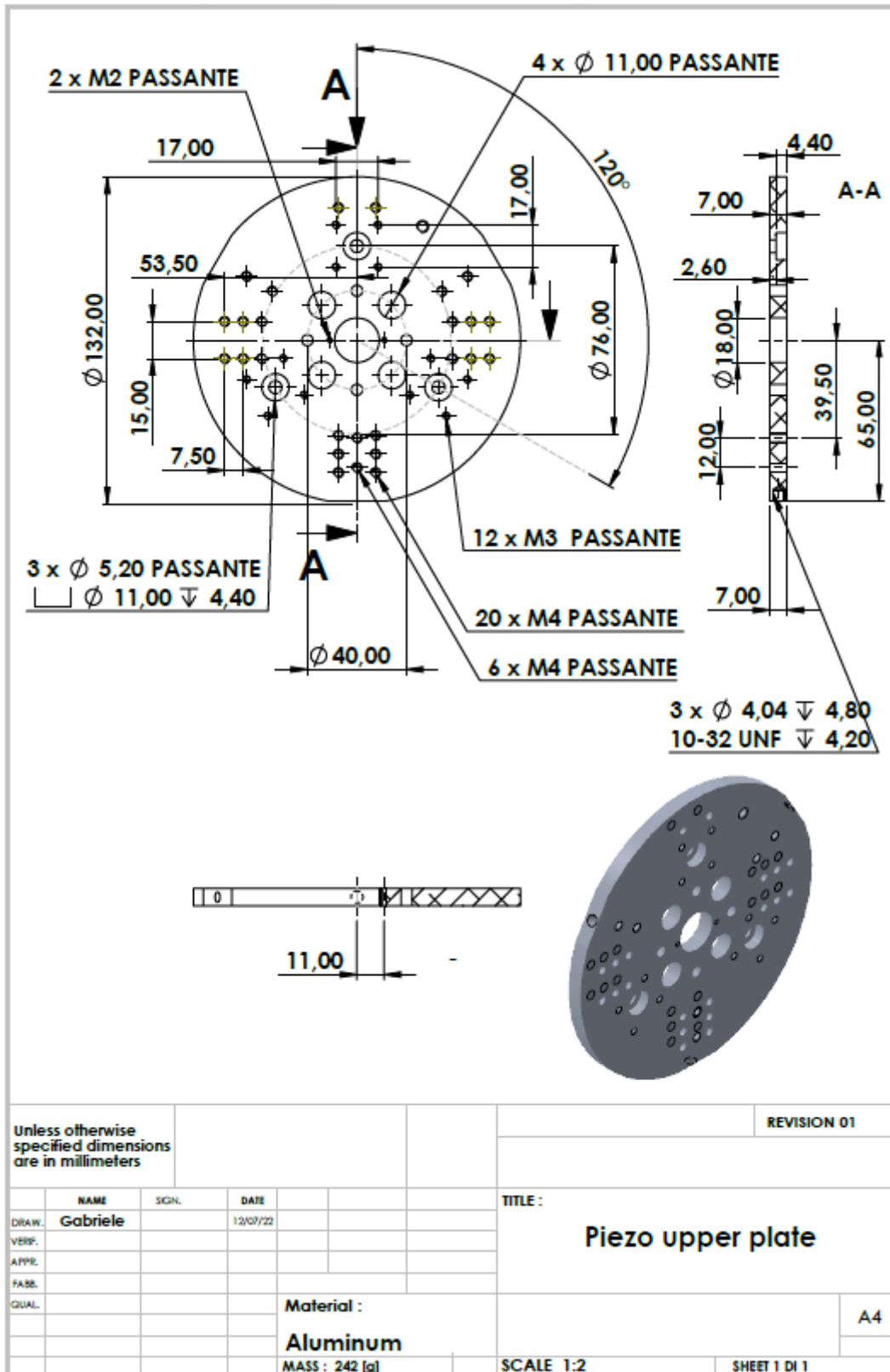Figure A.2: **"Base plate"**, for 6A80_C-based measurement system

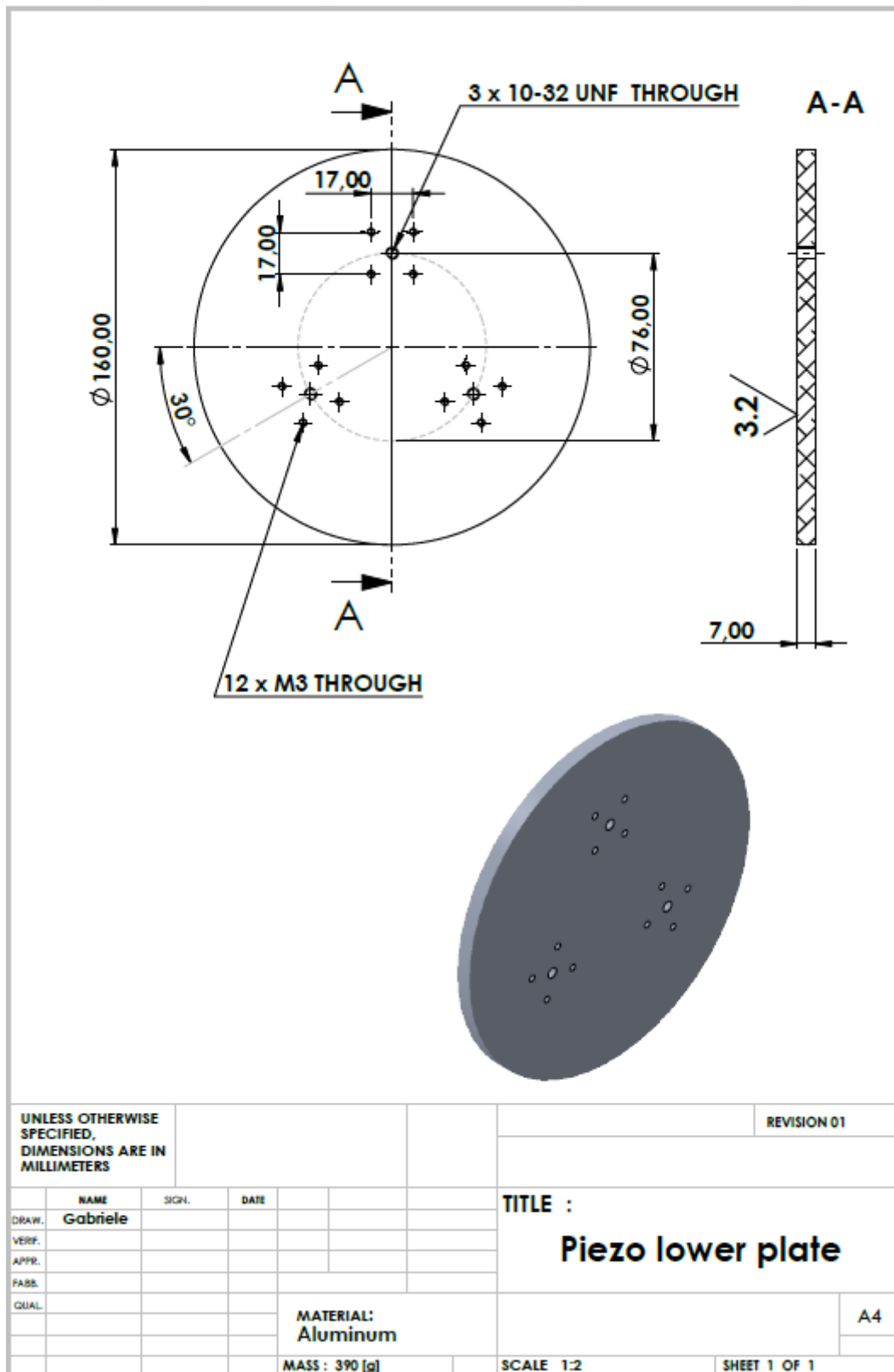Figure A.3: **"Piezo upper plate"**, for piezoelectric measurement system

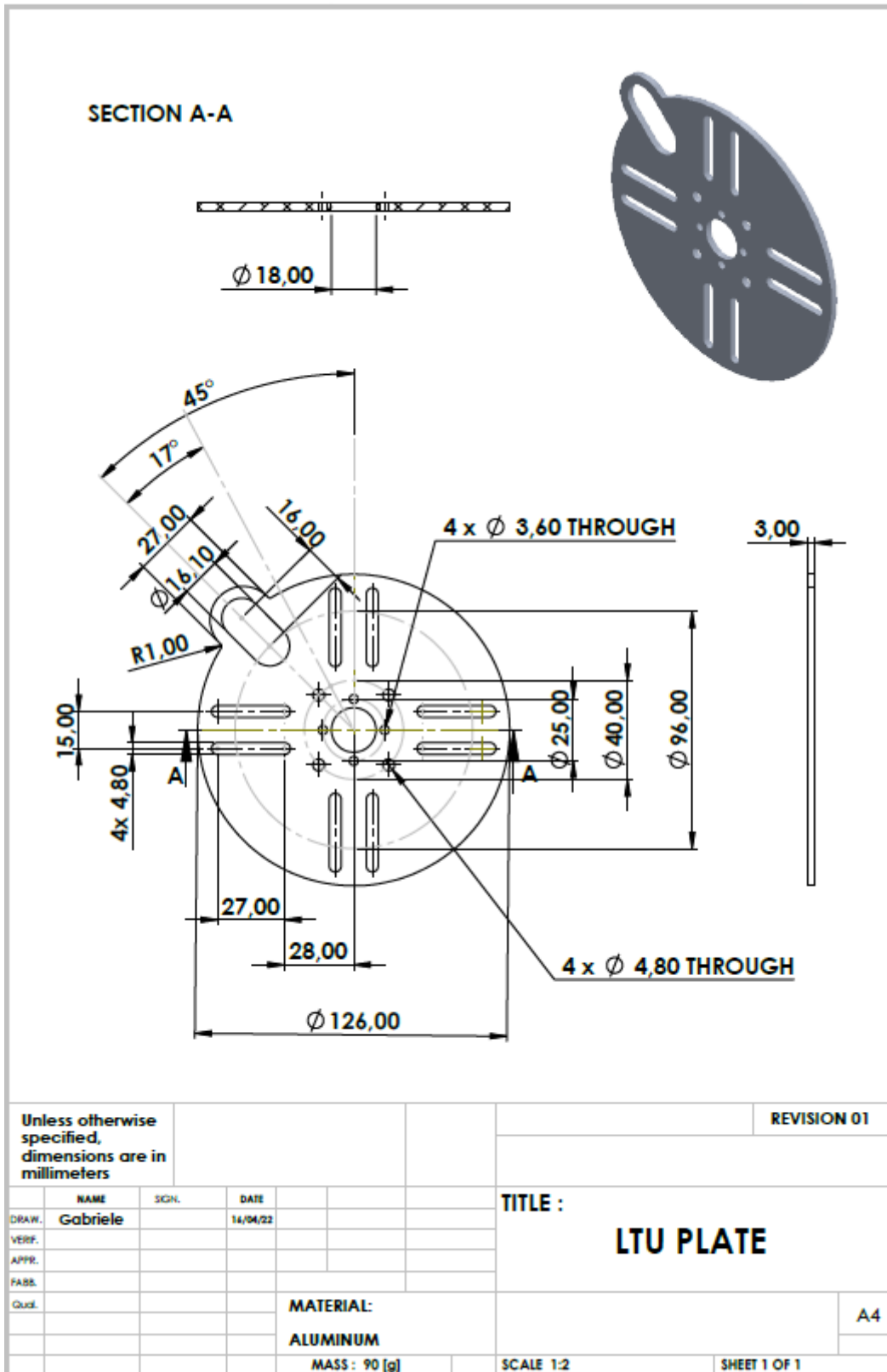Figure A.4: **"Piezo lower plate"**, for piezoelectric measurement system

SECTION A-A

Ø 18,00

45°

17°

27,00

Ø16,10

16,00

4 x Ø 3,60 THROUGH

3,00

R1,00

15,00

4x 4,80

A

A

Ø 25,00

Ø 40,00

Ø 96,00

27,00

28,00

4 x Ø 4,80 THROUGH

Ø 126,00

	NAME	SIGN.	DATE			REVISION 01

Unless otherwise specified, dimensions are in millimeters

DRAW. Gabriele 16/04/22

VERF.

APPR.

FABB.

Qual.

TITLE :

LTU PLATE

MATERIAL: ALUMINUM

MASS : 90 [g]

SCALE 1:2

SHEET 1 OF 1

A4

Figure A.5: **"LTU plate"**, for 6ADF80-based measurement system
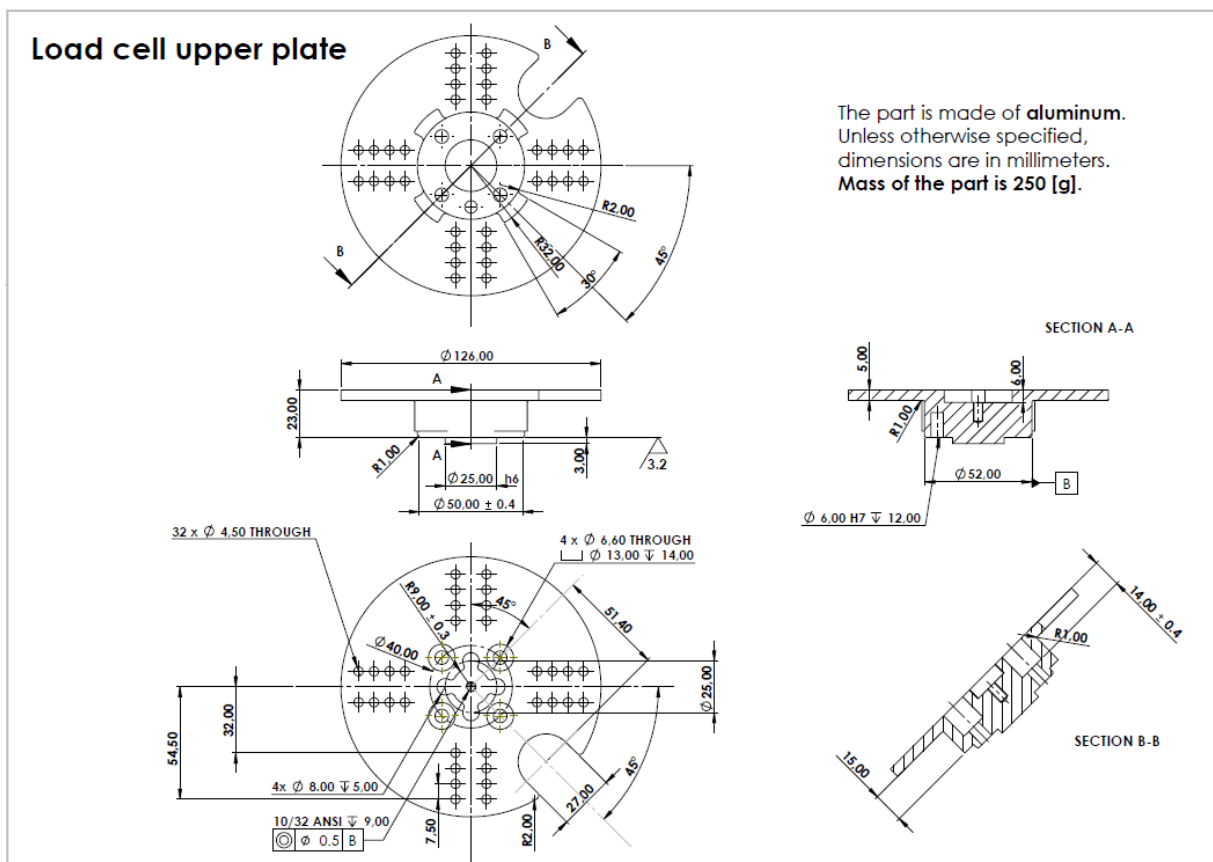
Figure A.6: **"Load cell upper plate"**, for 6ADF80-based measurement system
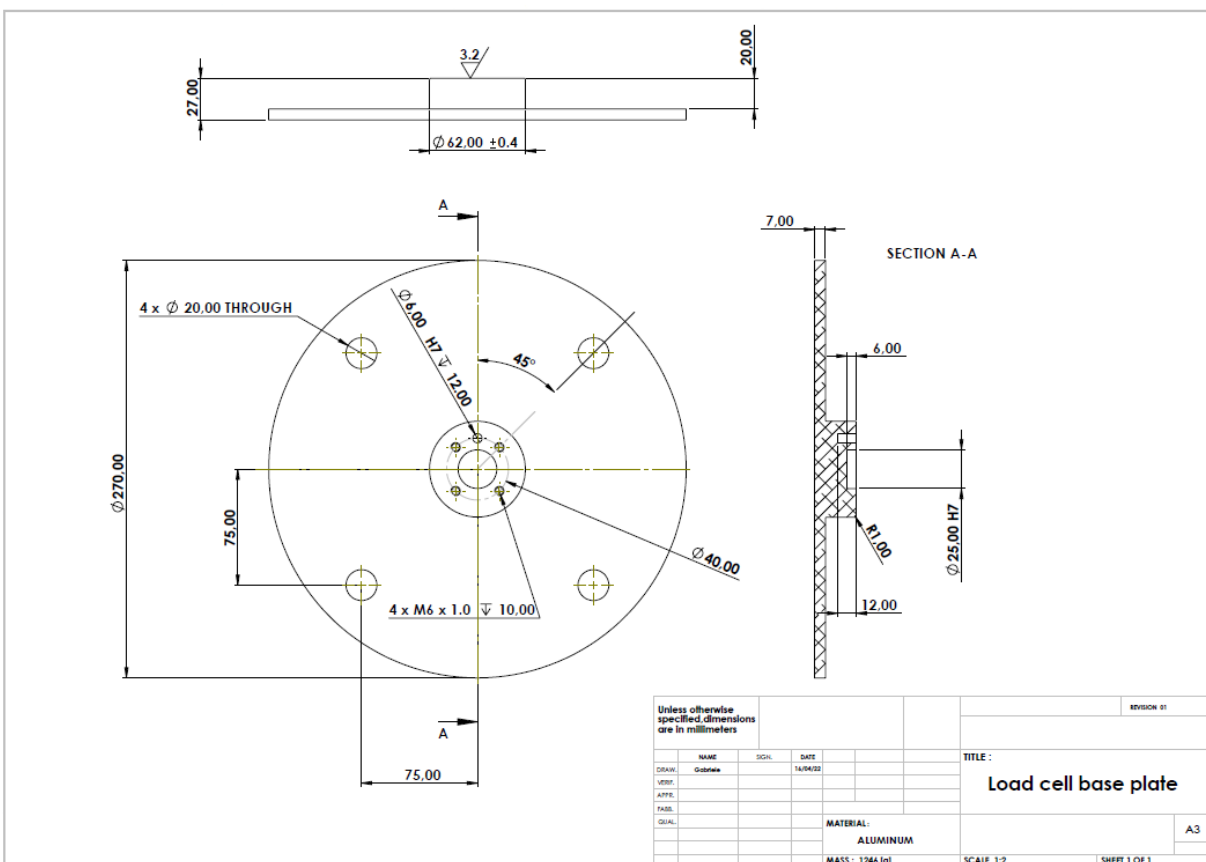
Figure A.7: **"Load cell base plate"**, for 6ADF80-based measurement system

B | Appendix B - Method for selecting an LTU and associated PS

As it was discussed in the main body of this work, an electrical multi-propeller system includes propellers, BPMS motors, ESCs (see section 1.1.1) and of course a power source. **Since multi-propeller test rig could be employed both to test complete designs and to assist the development of new ones, it is deemed appropriate to outline a method for the preliminary choice of the BPMS motors, ESCs and power source. This is done in section B.1, while section B.2 discusses some of the physics behind this method and some experimental techniques to determine the "Motor "constants" " (see section B.2.1).**

B.1. Outline of the method

Once estimates of the required **peak and RMS (Root mean square) torque**, as well as the **operating speed** (which, as it will be clarified later on, is **not** the maximum speed that the motor can sustain) are available for the given rotor/propeller, the designer will be able to select possible candidate BPMS motors. In fact, as it will be further explained in this Appendix, these three parameters constrain both the structural/mechanical and the electrical side of the system. The following equation may be used to calculate the required **peak torque**, let's call it $\mathbf{T_{pk}}$:

$$\mathbf{T_{pk} = N_{sft}(T_P + T_I + T_F)} \tag{B.1}$$

in which $\mathbf{T_P}$ is the **propeller torque** ("load" torque), $\mathbf{T_F}$ is the **torque to overcome friction** and $\mathbf{T_I}$ is the **torque due to inertia**, i.e. the torque required to accelerate the load from rest or from a lower to a higher speed, and it is given by $T_I = \ddot{\alpha}(J_{prop} + J_R)$, in which:

- $J_{prop} + J_R$ is the sum of the inertia of the propeller and that of the rotor of the motor

- $\ddot{\alpha}$ is the desired acceleration

$\mathbf{N_{sft}}$ is a safety factor to obtain a sufficient margin for other factors such as frictional "wind torque", associated with "windage losses", namely the power absorbed by the fluid surrounding the rotor as a result of the relative motion between the BPMS rotor and stator. **A factor of safety greater than 1.2 (see reference [31]) may be needed if one takes into account the negative impact of temperature on motor constants and parameters (see reference [7] and section B.2), being their datasheet values usually related to a "cold motor"**.

The average continuous torque required to run the rotor is approximately equal to the RMS torque, which, **assuming constant acceleration/deceleration curves**, can be determined as (see [31]) :

$$\mathbf{T_{RMS}} = \sqrt{\frac{\mathbf{T_{acl}T_{pk}^2 + T_{run}(T_P + T_F)^2 + T_{dcl}(T_I - T_P - T_F)^2}}{\mathbf{T_{acl} + T_{run} + T_{dcl}}}} \tag{B.2}$$

in which :

- $\mathbf{T_{acl}}$ is the "acceleration time", i.e. the time duration of the constant acceleration curve

- $\mathbf{T_{run}}$ is the "run time", i.e. the time duration of the zero acceleration/deceleration interval

- $\mathbf{T_{dcl}}$ is the "deceleration time", i.e. the time duration of the constant deceleration curve

Assuming that the propeller does not change its angular speed frequently, and that the design maximum angular speed is $\mathbf{\Omega_{max}}$, the required rated operating speed of the motor can be taken equal to (see [31]) :

$$\Omega_{\mathbf{BPMS}} = 1.1\Omega_{\mathbf{max}} \tag{B.3}$$

in which "1.1" is a safety factor. So, the motor rated maximum operating speed, call it $\mathbf{\Omega_{BPMS}^{max}}$, must be greater than $\mathbf{\Omega_{BPMS}}$ calculated from (B.3). In lieu of $\mathbf{\Omega_{BLDC}^{max}}$, a viable option to estimate it is by means of the so called **motor speed constant $\mathbf{K_v^m}$** (discussed in section B.2) of the motor. **From the practical point of view this constant is the proportionality constant between the angular speed and the voltage $\mathbf{V_{avg}^m}$**

(see section 2.1) applied to the motor when the current, and therefore the torque, are equal to zero. Actually, some current will flow even when no load is put on the BPMS motor rotor, because some torque has to be developed to compensate the losses inside it. Neglecting the voltage drop associated with this current, it can be said that $\mathbf{K_v^m}$ is the proportionality constant between speed and $\mathbf{V_{avg}^m}$ when no load is put on the rotor. When the rotor is loaded, its speed is naturally less with respect to the no-load case, for the same value of $\mathbf{V_{avg}^m}$. In particular, at the rated maximum supply voltage $\mathbf{V_{dc}^{max}}$ (more on this in section B.2.), the no-load speed, given by $\mathbf{K_v^m V_{dc}^{max}}$ can be typically up to 150% of $\mathbf{\Omega_{BPMS}^{max}}$ (see [31]). Therefore, given $\mathbf{K_v^m}$, one can estimate $\mathbf{\Omega_{BPMS}^{max}}$ as :

$$\Omega_{\mathbf{BPMS}}^{\mathbf{max}} = \frac{\mathbf{K_v^m V_{dc}^{max}}}{1.5} \tag{B.4}$$

The **continuous (supply) current**, $\mathbf{I_{cc}}$ that the motor (and ESC) has to be able to handle is now determined by the following :

$$\mathbf{I_{cc}} = \frac{\mathbf{T_{RMS}}}{\mathbf{K_t^m}} \tag{B.5}$$

in which $\mathbf{K_t^m}$ is the so called **"motor torque constant"** (discussed further in section B.2), **which is defined as the proportionality constant between the total torque developed by the motor** τ **and the power supply current** $\mathbf{I_{dc}}$ (see section 1.1.1). Typically $\mathbf{K_t^m}$ can be found in the manufacturer datasheet. **Equation** (B.5) **suggests that one can translate a requirement on torque directly into a requirement on current. However, the rotor may of course fail due to excessive torque due to mechanical stresses, even if the the current is below its maximum rated value. Therefore, one can say that current and torque are "equivalent" only if it is sure that the current limit is exceeded well before the mechanical one.**

Now it is time to size the **PS**, which typically consist in a set of "lipo" batteries. To this end it, let's first determine the required supply voltage $\mathbf{V_{dc}}$.

$\mathbf{V_{dc}}$ has to be large enough or, alternatively, the $\mathbf{K_v^m}$ should be large enough for the motor to achieve the required operating speed $\mathbf{\Omega_{BPMS}}$ at its rated continuous (RMS) torque [1], without exceeding the $\mathbf{V_{dc}^{max}}$ of the motor and the $\mathbf{V_{dc}^{max}}$ of the ESC.

The peak current can be instead calculated as (clearly also the ESC has to be able to handle this peak current) :

---

[1] see (B.4), in which now the chosen $\mathbf{V_{dc}}$ takes the place of $\mathbf{V_{dc}^{max}}$

$$\mathbf{I_{pk}} = \frac{\mathbf{T_{pk}}}{\mathbf{K_t^m}} \tag{B.6}$$

Knowing $\mathbf{V_{dc}}$ and $\mathbf{I_{pk}}$, one can finally calculate the required motor peak power as :

$$\mathbf{P_{pk}} = \mathbf{V_{dc}I_{pk}} \tag{B.7}$$

Now, using $\mathbf{I_{pk}}$ and $\mathbf{P_{pk}}$, one can select an appropriate power source. As an example, suppose one wants to choose an appropriate battery pack as the power source. Of course the battery pack must be able to provide the required voltage $\mathbf{V_{dc}}$ and must have a sufficient **capacity** (typically expressed in "mAh" unit), which must be chosen by the designer according to the application. Then, since $\mathbf{I_{pk}}$ represents the minimum required **battery discharge current**, one can calculate the minimum required **battery pack "C rating"** as (here the capacity is expressed in "Ah" unit) :

$$\frac{\text{Maximum discharge current}}{\text{Capacity}}$$

To recap, some of the **important parameters and ratings** to be looked up or to be determined experimentally for the selection of a BPMS motor, are:

- $\mathbf{\Omega_{BPMS}^{max}}$, or, alternatively $\mathbf{K_v^m}$

- $\mathbf{V_{dc}^{max}}$

- $\mathbf{T_{RMS}^{max}}$, or, alternatively, $\mathbf{I_{cc}^{max}}$, if $\mathbf{K_t^m}$ is known (and mechanical stresses are not exceeded)

- $\mathbf{T_{pk}^{max}}$, or, alternatively, $\mathbf{I_{pk}^{max}}$, if $\mathbf{K_t^m}$ is known (and mechanical stresses are not exceeded)

- $\mathbf{I_{cc}^{max}}$

- $\mathbf{I_{pk}^{max}}$

- $\mathbf{K_t^m}$

- $\mathbf{K_v^m}$

B.2. The physics behind the method

In the previous section some BPMS motors ratings such as the maximum continuous current $\mathbf{I_{cc}^{max}}$ and peak current $\mathbf{I_{pk}^{max}}$, and some parameters, such as $\mathbf{K_v^m}$ and $\mathbf{K_t^m}$ were mentioned. But where do these ratings come from? And what do these parameters represent?

B.2.1. Motor "constants"

To begin with, it is important to understand that all the constants which will be discussed in the following characterize the motor in its steady state condition. Therefore, parameters like inductance of the coils $\mathbf{L_m}$, propeller inertia $\mathbf{I_R}$, etc. don't play any role in the following discussion.

In section 1.1.1 the **per-phase** torque and back-EMF functions $\mathbf{k_t}(\boldsymbol{\theta_r})$ and $\mathbf{k_e}(\boldsymbol{\theta_r})$, respectively were introduced, and it was mentioned that they can be proven to be equal to each other when consistent units are used. The peak value of $\mathbf{k_t}(\boldsymbol{\theta_r})$ was denoted with $\mathbf{K_t}$ (see e.g. Figure 1.4). By analogy, the peak value $\mathbf{k_e}(\boldsymbol{\theta_r})$ was denoted with $\mathbf{K_e}$, which is numerically equal to $\mathbf{K_t}$. $\mathbf{K_t}$ and $\mathbf{K_e}$ are known respectively as **per-phase** torque constant and per-phase back-EMF constant, and **The way in which $\mathbf{K_t}$ and $\mathbf{K_e}$ are related to $\mathbf{K_t^m}$ and $\mathbf{K_v^m}$ defined in section B.1 depends on whether the motor is delta-connected or wye-connected and on whether the motor is trapezoidal or sinusoidal. For the sake of simplicity, let's assume for the remaining discussion in this Appendix that six-step commutation is used to control the trapezoidal motor while FOC with either SVPWM or SPWM is used to control the sinusoidal one**.

So, let's first consider the relationship between $\mathbf{K_e}$ and $\mathbf{K_v^m}$ starting with the case of a trapezoidal, delta-connected motor. From equation 1.24 it is clear that when no current flows through the motor, the following holds :

$$\mathbf{V_{avg}^m} = \mathbf{K_e}\boldsymbol{\omega} \tag{B.8}$$

So, from the definition of $\mathbf{K_v^m}$ given in section B.1, and from equation B.8 it follows that :

$$\mathbf{K_v^m} = \frac{1}{\mathbf{K_e}} \tag{B.9}$$

Now let's move on to the case of a **trapezoidal, wye-connected motor**, and let's assume an isolated neutral for the sake of simplicity. By resorting to Figures 1.5 and 1.1, and following a line of reasoning totally analogous to the one that led to equation 1.24, equation B.10 can be obtained :

$$\mathbf{V^m_{avg} = 2R_sI^m_{avg} + 2((L_{mag} + L_l) - M)\frac{dI^m_{avg}}{dt} + 2K_e\omega} \tag{B.10}$$

from which it immediately follows that for this case the following holds instead :

$$\mathbf{K^m_v = \frac{1}{2K_e}} \tag{B.11}$$

Moving on to the case of a (balanced) **sinusoidal wye-connected motor**, it turns out that the line-to-line voltage is $\sqrt{3}$ times larger than the phase (line-to-neutral) voltage. Now, **if the SVPWM technique is used**, it turns out that $\mathbf{V^m_{avg}}$ is $\sqrt{3}$ times larger that the peak value of the phase voltage (see e.g. section 5.3 of reference [12]), and this means that if no current flows through the motor, the following relationship holds :

$$\mathbf{K^m_v = \frac{1}{\sqrt{3}K_e}} \tag{B.12}$$

However, **if the SPWM technique is instead used**, relationship B.12 is only approximately valid, being $\mathbf{V^m_{avg}}$ two times larger that the peak value of the phase voltage (see reference [12]). So, in this case the correct relationship is :

$$\mathbf{K^m_v = \frac{1}{2K_e}} \tag{B.13}$$

Let's now move on to the relationship between $\mathbf{K_t}$ and $\mathbf{K^m_t}$. From the definition of the latter and from equations 1.9 and 1.10, it follows that for sinusoidal and trapezoidal wye-connected motors, the following hold, respectively :

$$\mathbf{K^m_t = \frac{3}{2}K_t} \tag{B.14}$$

and

$$\mathbf{K^m_t = 2K_t} \tag{B.15}$$

Finally, in the case of a trapezoidal delta-connected motor, from equation 1.3 and Figure 1.21, it follows that :

$$\mathbf{K_t^m = K_t} \tag{B.16}$$

At this point it should be **remarked** that the "per-phase" parameters $\mathbf{K_e}$ and $\mathbf{K_t}$, and consequently the parameters $\mathbf{K_v^m}$ and $\mathbf{K_t^m}$, are influenced by temperature (see reference [7]), and this should be taken into account if a more refined selection among candidate BPMS motors is needed/desired [2].

To determine $\mathbf{K_t}$ experimentally, apply an appropriate voltage to the motor (for example a voltage equal but not greater than the maximum rated one, if known). Then, apply a progressively higher constant torque load to the motor [3] and measure the power supply current $\mathbf{I_{dc}}$ corresponding to each applied and measured torque load, including the current when no load is applied [4]. **Since an adjustable torque load is necessary, a particle break or an adjustable hysteresis dynamometer may be used for applying the load, while a current probe may be used to measure the current**. To obtain the important "Torque vs. Speed" curve (or, equivalently, the "Power vs. Torque" curve) it is also necessary to record the corresponding angular speed. Then, plot each data point on a graph with current on the horizontal axis, and applied torque on the vertical axis. The slope of the resulting regression line, is the experimental value of $\mathbf{K_t^m}$. The line so obtained is the " $\mathbf{T_P}$ vs $\mathbf{I_{dc}}$" line. This line does not pass through the origin, but it has a negative offset on the vertical axis (torque axis), whose absolute value is equal to the "friction" torque $\mathbf{T_F}$, i.e. the torque developed at zero **applied** torque. The value of $\mathbf{T_F}$ can be obtained from the measured value of the no (applied) load current, $\mathbf{I_0}$, as follows :

$$\mathbf{T_F = K_t^m I_0} \tag{B.17}$$

In which $\mathbf{K_t^m}$ has been previously calculated as the slope of the regression line. Sometimes the value of $\mathbf{I_0}$ at some given voltage can be found in the motor datasheet.

The same discussion holds for the "Torque vs. angular speed" line, from which the "Power vs. angular speed" is directly derived. **Another method of determining $\mathbf{K_t^m}$**

---

[2]From the physical point of view, the change in $\mathbf{K_e}$ with temperature is governed by the change in the properties of the magnets with temperature

[3]The torque load is increased starting from zero and until the motor stalls

[4]It is clear that before this test, both the closed-loop speed and torque controllers, if present, have to be disabled

is to first determine $\mathbf{K_e}$ using the "Constant RPM method" described below, and then, using the fact that $\mathbf{K_e = K_t}$, the value of $\mathbf{K_t^m}$ can be determined from equation B.14, or B.15 or B.16 according to the type of motor. It is important to mention that, due to the dependency of $\mathbf{K_t^m}$ on temperature, the temperature of the windings and the magnets should be ideally maintained as constant as possible between all successive measurements

To determine $\mathbf{K_v^m}$ experimentally, apply an increasingly high voltage (to be measured) to the motor, up to the maximum rated voltage (if known), and measure the corresponding angular velocity [5]. As for $\mathbf{K_t^m}$, $\mathbf{K_v^m}$ is given by the slope of the regression line. It should be mentioned that the velocity-dependent components of the friction torque $\mathbf{T_F}$ (like for example the "wind torque" mentioned in section B.1) make this method of determining $\mathbf{K_v^m}$ approximate, although a very good approximation is expected. **An even more accurate value for $\mathbf{K_v}$ may be obtained by spinning the motor at constant RPM with its wires disconnected and measuring the value of the peak voltage across any two pair of its wires, i.e. the value of the peak of the line-to-line voltage, let' call it $\mathbf{V_{l-l}^{pk}}$.** In this test, the relationship between $\mathbf{V_{l-l}^{pk}}$ and the peak of the phase voltage, let' call it $\mathbf{V_{ph}^{pk}}$, for the different types of motors is the following :

- $\mathbf{V_{l-l}^{pk} = \sqrt{3} V_{ph}^{pk}}$ for a sinusoidal, wye-connected motor

- $\mathbf{V_{l-l}^{pk} = 2 V_{ph}^{pk}}$ for a trapezoidal, wye-connected motor

- $\mathbf{V_{l-l}^{pk} = V_{ph}^{pk}}$ for a trapezoidal, delta-connected motor

Therefore, if $\boldsymbol{\omega}$ is the constant velocity at which the motor is spinning, $\mathbf{K_e}$ can be obtained as follows for the three types of motor :

- $\mathbf{K_e = \dfrac{V_{l-l}^{pk}}{\sqrt{3}\omega}}$ for a sinusoidal, wye-connected motor

- $\mathbf{K_e = \dfrac{V_{l-l}^{pk}}{2\omega}}$ for a trapezoidal, wye-connected motor

- $\mathbf{K_e = \dfrac{V_{l-l}^{pk}}{\omega}}$ for a trapezoidal, delta-connected motor

Then, $\mathbf{K_v^m}$ can be obtained from equation B.9, or B.11, or B.12 or B.13 according to the type of motor and modulation technique. As an example, this method of determining $\mathbf{K_v^m}$ is applied in article [8] to the particular case of a sinusoidal motor [6].

---

[5]Again, it is clear that before this test, both the closed-loop speed and torque controllers, if present, have to be disabled

[6]In this article the modulation technique is not specified, but a SVPWM technique can be assumed

B.2.2. Motor ratings

Let's start by analyzing the continuous supply current $\mathbf{I_{cc}^{max}}$ rating [7]. $\mathbf{I_{cc}^{max}}$ is easily understood as the maximum continuous current the motor can draw without the temperature of its windings exceeding the maximum rated value (it could be 125°).

Let's now move on to the peak torque or, equivalently the peak current rating. To this end, let's consider as an example the case of a trapezoidal, delta-connected BPMS motor, whose behaviour is governed by equation 1.24. The resistance $\mathbf{R_s}$ is typically of the order of 0.1Ω. So, if one suddenly applies all of $\mathbf{V_{avg}^m}$, which can be as high as 60V or even higher depending on the motor, an enormous amount of current is generated at **startup**[8] (namely when $\boldsymbol{\omega}$ is ≈ 0). However, as soon as the rotor starts spinning, the back EMF voltage $\mathbf{K_e}\boldsymbol{\omega}$ starts to rise, thus reducing the amount of current so to keep the total voltage drop equal to $\mathbf{V_{avg}}^m$. This means that it is typically necessary to implement a circuit or a logic which **modulates** the supply voltage so that it is more or less gradually applied to the motor and the peak current rating of the motor (and of the ESC) is not exceeded. Clearly, high current will also be produced if the rotor stalls ("locked rotor" condition), and this is why generally ESCs feature **stall protection** algorithms.

In view of the discussion so far, the $\mathbf{V_{dc}^{max}}$ can now be understood. The first limitation on $\mathbf{V_{dc}}$ comes from the mechanical world. In fact, $\boldsymbol{\omega}$ is proportional to $\mathbf{V_{dc}}$ (or $\mathbf{V_{avg}^m}$ if $\mathbf{V_{dc}}$ is PWM modulated) through $\mathbf{K_v^m}$, so that by continuously rising $\mathbf{V_{dc}}$ one will eventually end up with damaging the bearings or detaching the magnets from the rotor due to centrifugal forces. This of course sets a maximum speed that the motor can sustain. Setting the structural/mechanical limits apart, the motor wires are insulated to prevent the voltage from jumping from one wire to the other. However, suppose now (and this is typically the case) that $\mathbf{V_{dc}}$ does not exceed the wire rating for voltage jumps, and that the current $\mathbf{I_{dc}}$ is at its maximum continuous rated value $\mathbf{I_{cc}^{max}}$. Increasing the supply voltage means requesting more RPMs from the motor, and consequently more torque [9]. But more load torque means a current greater than $\mathbf{I_{cc}^{max}}$, and so excessive heat, ultimately leading to the destruction of the motor (winding melting and motor demagnetization are both possible). So, in this situation, the only way to increase $\mathbf{V_{dc}}$ above $\mathbf{V_{dc}^{max}}$, would be to reduce in some way the required torque. **In view of the discussion so far, $\mathbf{V_{dc}^{max}}$ can be defined as the supply voltage at which the UNloaded motor can run indefinitely without damaging itself.** [10]

---

[7]Since current and torque are related by $\mathbf{K_t^m}$, the physical origin of the $\mathbf{I_{cc}^{max}}$ rating is the same as that of the $\mathbf{T_{RMS}^{max}}$ rating

[8]A similar situation happens during an acceleration or a deceleration phase

[9]Take for example a propeller. The aerodynamic torque acting on it increases with RPMs

[10]e.g. because of centrifugal forces or overheating

Finally, let's consider the $\Omega_{\textbf{BPMS}}^{\textbf{max}}$ rating. To begin with, it is clear at this point that the constraint on maximum continuous torque $\textbf{T}_{\textbf{RMS}}^{\textbf{max}}$ comes from temperature, and it is associated with current. The angular speed, on the other hand, is determined by the supply voltage $\textbf{V}_{\textbf{dc}}$ (or by $\textbf{V}_{\textbf{avg}}^{\textbf{m}}$). Consider now as an example again the case of trapezoidal, delta-connected motor, and therefore equation 1.24 with $\textbf{I}_{\textbf{avg}}^{\textbf{m}} = \textbf{I}_{\textbf{cc}}^{\textbf{max}}$. With this current the motor delivers its maximum rated torque $\textbf{T}_{\textbf{RMS}}^{\textbf{max}}$. By appropriately choosing the value of $\textbf{V}_{\textbf{dc}}$ (if the full supply voltage is applied $\textbf{V}_{\textbf{avg}}^{\textbf{m}} = \textbf{V}_{\textbf{dc}}$), one can make the motor spin at a given $\boldsymbol{\omega}$, which is higher the higher is $\textbf{V}_{\textbf{dc}}$. However, $\textbf{V}_{\textbf{dc}}$ is limited to $\textbf{V}_{\textbf{dc}}^{\textbf{max}}$, so that it exists a speed above which the motor can no longer deliver the full $\textbf{T}_{\textbf{RMS}}^{\textbf{max}}$ [11]. **This speed is the rated maximum operating speed $\Omega_{\textbf{BPMS}}^{\textbf{max}}$, and its value can be obtained by solving equation 1.24 for $\boldsymbol{\omega}$, which yields equation B.18** [12] :

$$\Omega_{\textbf{BPMS}}^{\textbf{max}} = \frac{\textbf{V}_{\textbf{dc}}^{\textbf{max}} - \frac{2}{3}\textbf{R}_{\textbf{s}}\textbf{I}_{\textbf{cc}}^{\textbf{max}}}{\textbf{K}_{\textbf{e}}} \tag{B.18}$$

---

[11]However, if a torque less than $\textbf{T}_{\textbf{RMS}}^{\textbf{max}}$ is required from the motor, then of course an angular speed higher than $\Omega_{\textbf{BPMS}}^{\textbf{max}}$ can be achieved

[12]It should be noticed that both $\textbf{R}_{\textbf{s}}$ and $\textbf{K}_{\textbf{e}}$ in equation (B.18) are temperature dependent. So, if a reliable estimate of $\Omega_{\textbf{BPMS}}^{\textbf{max}}$ is needed, "hot" values must be used for these parameters

List of Figures

List of Tables

List of Symbols

Variable	Description	SI unit
T	Torque	$[N \cdot m]$
T	Period or time interval	$[s]$
Ψ_R	Rotor-stator flux linkage of a phase	$[\frac{N \cdot m}{A}]$
θ_r	Rotor angular position	$[rad]$
i	Phase current	$[A]$
I_{avg}^m	Average motor current	$[A]$
J	Moment of inertia	$[kg \cdot m^2]$
V	Phase voltage	$[V]$
V_{avg}^m	Average motor voltage	$[V]$
k_e	Per-phase Back-EMF function	$[\frac{V \cdot s}{rad}]$
k_t	Per-phase torque function	$[\frac{N \cdot m}{A}]$
τ	Motor total torque	$[N \cdot m]$
ω, Ω	Rotor angular speed	$[\frac{rad}{s}]$
I_{dc}	Power supply output current	$[A]$
K_t	Per-phase torque constant	$[\frac{N \cdot m}{A}]$
K_t^m	Motor torque constant	$[\frac{N \cdot m}{A}]$
K_e	Per-phase Back-EMF constant	$[\frac{V \cdot s}{rad}]$
K_v^m	Motor speed constant	$[\frac{rad}{s \cdot V}]$
e	Back-EMF	$[V]$
λ	Total stator flux linkage	$[\frac{N \cdot m}{A}]$
B	Flux density	$[\frac{N}{A \cdot m}]$
L, M	Inductance	$[\frac{N \cdot m}{A^2}]$
M	Moment	$[N \cdot m]$
P	Power	$[W]$
P	Number of pole pairs	
D	Duty cycle	

Acknowledgements